Adaptive Optics for Large Aperture Coherent Laser Radars

by

Naomi Esther Zirkind

Submitted to
the Department of Electrical Engineering and Computer Science
in partial fulfillment of the requirements for the degree of

Doctor of Philosophy

at the

Massachusetts Institute of Technology

June 1989

Signature of Author Signature redacted
Department of Electrical Engineering and Computer Science
March 1, 1989

Certified by Signature redacted
Prof. Jeffrey H. Shapiro
Thesis supervisor

Accepted by Signature redacted
Prof. Arthur C. Smith
Chairman, Department Committee on Graduate Students

Adaptive Optics for Large Aperture Coherent Laser Radars

by

Naomi Esther Zirkind

Submitted to the Department of Electrical Engineering
and Computer Science on March 1, 1989
in partial fulfillment of the requirements for the
Degree of Doctor of Philosophy in Electrical Engineering

When a coherent laser radar operates in the presence of atmospheric turbulence, and the radar aperture diameter is much larger than the turbulence coherence length, the radar's performance is significantly degraded by turbulence-induced beam distortions. This thesis addresses the compensation for turbulence effects on such large aperture radars by means of adaptive optics. The radar system model is of a ground-based monostatic radar doing angle-angle imaging of a spatially resolved speckle target located high above the earth's atmosphere. The effect of turbulence on the spatial resolution, carrier-to-noise (CNR), and the resolution and accuracy of range and velocity measurements is quantified, and the improvement that can be obtained with perfect turbulence phase correction is derived. A system for correcting the turbulence-induced phase distortions is then described and its performance derived. The turbulence information for wavefront correction is obtained from the target return. Separation of the speckle and turbulence distortions in the target return is necessary in order to improve the spatial resolution. The system transmits multiple wavelengths to achieve this separation. For system parameter values considered, the spatial resolution is within 1.2 times diffraction limited, and the CNR is within 3 decibels of the no-turbulence value. Consideration of available technology shows that the components necessary for construction of such a system are available or may be available in the near future.

Keywords: 1. Laser radar, 2. Adaptive optics, 3. Speckle reduction.

Thesis supervisor: Prof. Jeffrey H. Shapiro
Title: Professor of Electrical Engineering

Acknowledgements

First, I would like to thank G-d for making available to me all the resources necessary for completion of this thesis. In particular, I thank Him for creating this world, for giving me the intelligence and opportunity to understand some of its interesting features, and for showing His presence even in its most physical aspects.

I would also like to thank the Lubavitcher Rebbe, Rabbi Menachem M. Schneerson, שליט"א, for his blessings and guidance in every area in which they were needed.

I thank my thesis advisor, Professor Jeffrey H. Shapiro, for all his advice and assistance. His interested involvement in all aspects of the thesis preparation has been most helpful. I also thank Dr. William Keicher of Lincoln Laboratory, Group 52, for his support and encouragement of this research. I am grateful to Jim Daley of Group 52 for several conversations on practical aspects of laser radar and for giving me a guided tour of the Firepond laser radar facility. My readers, Professor R. H. Kingston and Professor D. H. Staelin, made several helpful suggestions regarding the presentation of the research results.

This thesis research was supported by the U. S. Department of the Air Force Contract F19628-85-C-0002 and by U. S. Army Research Office Contract DAAL03-87-K-0117. This support is appreciated.

Special thanks to my mother, Mrs. Rachael Silman שתליט"א, for her constant encouragement, support and guidance, and for her wise advice throughout my years at MIT, and special thanks to my husband, Yaakov Mendel Zirkind שי', for his help in every way.

Contents

List of Figures

List of Tables

Chapter 1

Introduction

1.1 Background

A radar is a remote sensing system which measures various characteristics of a distant target by transmitting an appropriate electromagnetic waveform and detecting the nature of the resulting target echo. In basic structure, a radar comprises a transmitter, consisting of an electromagnetic waveform generator and a transmitting antenna, and a receiver, consisting of a receiving antenna, front-end mixers and amplifiers, and a signal processor. Radars have been in use since around 1940, with the preponderance of systems employing wavelengths in the microwave range, 1 mm to 1 meter. These microwave radars have been employed in the detection, location and tracking of aircraft, space targets, ships, land vehicles, and storms, as well as for navigation, altitude and velocity measurements, and surveying [1, Section 1.6]. They operate at wavelengths for which atmospheric propagation effects are nearly inconsequential, although substantially better angular, range, and velocity resolution could be obtained at shorter wavelengths, e.g. millimeter or optical wavelengths.

Since the late 1960's, coherent laser radars have been under development at a number of laboratories [2]-[7]. These systems use a laser, most commonly a 10.6 μm wavelength CO_2 laser, as the "waveform generator". They are termed "coherent" because their receivers employ optical heterodyne detection [8], a technique akin to microwave superheterodyne reception. As a result, coherent laser radars operate on the same basic principles as microwave radars, but, because of their much shorter wavelength, they have different advantages and disadvantages. In particular, the diffraction-limited far-field angular beamwidth at wavelength λ of an antenna of diameter d is approximately λ/d radians [9]. Thus, for a given antenna size, a laser radar is capable of much finer angular resolution than is a microwave radar. Alternatively, a compact laser system can match the angular resolution of a much larger microwave system. In a similar vein, laser radars offer better target range resolution than do microwave systems. The range resolution of a pulsed radar which transmits transform-limited pulses is approximately $c\tau/2$, where c is the speed of light and τ is the pulse duration [1, Section 10.8], [10]. Because infrared frequencies are much higher than microwave frequencies, the pulse durations can be shorter, at the same percentage bandwidth, allowing better range resolution. If the transmitted pulse is chirped, then the range resolution is of the order of c/B, where B is the bandwidth of the chirped pulse. At infrared frequencies, larger chirp bandwidths can be used at the same percentage bandwidth. A third advantage of coherent laser radars arising from their short wavelength is their superior velocity resolution; velocity resolution is approximately $\lambda/4T$, where T is the beam dwell time [1, Section 10.8], [10].

Coherent laser radars derive the preceding resolution advantages over microwave radars from their much shorter wavelength; this wavelength difference also leads to some disadvantages. The earth's atmosphere is far from a benign propagation medium at infrared and visible wavelengths. Attenuation due to molecular absorption, and random spatio-temporal fluctuations due to turbulence-induced refractive index variations can place significant limitations on clear weather atmospheric laser radar performance [11],[12]-[14]. Additional attenuation and multiple scattering effects come into play in bad weather (turbid atmosphere) conditions [14]. Thus, unlike microwave radars, ground based laser radars will not provide all-weather long range sensing capability. A second disadvantage of laser radars is their sensitivity to microscopic target surface irregularities. These irregularities give rise to random spatial and temporal target-return fluctuations, known as speckle [15,11], which can seriously degrade laser radar performance.

Thus, coherent laser radars have advantages where microwave radars have disadvantages, and vice versa. Therefore, laser radars can be considered supplements, rather than replacements, for microwave radars. Some applications which exploit the superior resolution capabilities of infrared coherent laser radars are: tactical imaging systems, missile and aircraft guidance, clear air turbulence sensors, fire control and line-of-sight command systems, remote sensing of atmospheric constituents, and satellite tracking [16].

1.2 Motivation

This thesis is concerned with system theory for coherent laser radars. Previous work in this area has included development of mathematical system models for several coherent laser radar configurations and use of these models for analysis of radar performance in imaging, target detection, range measurement, and velocity measurement applications [11,17,18]. These models incorporate the statistical effects of target speckle and glint, and local oscillator (LO) shot noise. In the absence of atmospheric turbulence, the carrier-to-noise ratio (CNR), spatial resolution, and range and velocity measurement accuracy all improve with increasing aperture size.

The effects of propagation through atmospheric turbulence have also been included in models of compact laser radars for imaging and target detection applications [11]. These analyses show that when the atmospheric scintillation is small (e.g. for a vertical propagation path), the performance of compact laser radars is negligibly affected by turbulence. However, as the aperture size is increased, the performance saturates due to turbulence-induced wavefront distortions. In particular, it has been shown [12,13] that the speckle-target heterodyne mixing efficiency of a monostatic laser radar is significantly reduced by these distortions when the aperture diameter is much larger than the turbulence coherence length. Therefore, the target measurements derived from such a distorted wave will also be impaired by the turbulence. Furthermore, the spatial resolution is degraded due to the beam spreading that results from these wavefront distortions.

If the turbulence-induced wavefront distortions could be corrected by using adaptive optics, then the performance advantage of large aperture laser radars could be restored. The basic concept of adaptive optics is the use of a wavefront correction system to compensate, in real time, for random wavefront fluctuations. Some applications in which adaptive optics techniques have been used or would be useful are: large ground-based telescopes whose angular resolving power is limited by atmospheric turbulence, large telescopes orbiting in space which suffer varying thermal and gravitational stresses, and optical systems for high energy lasers whose wavefronts are deformed due to thermal effects in the components or in the propagation path [19,20]. This thesis presents the structure of a laser radar system which employs adaptive optics to correct the turbulence-induced wavefront distortions, and it derives the improvement in performance that could be obtained with the use of such a system.

1.3 Thesis Outline

In Chapter 2 the basic model of the laser radar system is presented. The radar system model is of a ground-based monostatic radar doing angle-angle imaging of a spatially resolved speckle target located high above the earth's atmosphere. The model of the transmitter and receiver sections of the radar includes assumptions about the transmitting laser and the heterodyne detection scheme. Mathematical models are given for the radar signal, the speckle target reflectivity, and the atmospheric turbulence. The radar signal and target reflectivity models have been previously used in laser radar system analyses [11,21], and the turbulence model been used previously to model turbulence effects on optical propagation through the atmosphere [22,23,24,25].

Chapter 3 describes the effects of atmospheric turbulence on radar performance, given in terms of the spatial resolution, CNR, and the resolution and accuracy of range and velocity measurements. The performance degradation for large aperture radars is derived and evaluated. The performance degradation results are given as formulas that may be analytically evaluated as a function of system parameters and turbulence parameters. These formulas quantitatively show the increasing degradation in radar performance with increasing aperture size. The spatial resolution and some of the CNR results have been derived previously [25,12,13], but are briefly rederived here in order to express them in terms of the notation used here. The effects of turbulence on the resolution and accuracy of range and velocity measurements are new results.

Chapter 4 presents the improvement in radar performance that results from perfect correction of the turbulence phase distortions. The results given here represent the best performance that a turbulence phase correction system could possibly achieve. These results show that perfect turbulence phase correction can very nearly restore the radar performance to the no-turbulence level for vertical-path propagation, if the diffraction-limited spot area on target is smaller than the target-plane atmospheric coherence area.

Although the improvement in beam quality that can be obtained with adaptive wavefront correction has been previously examined [19,26], the effect of such correction on laser radar performance has not, to our knowledge, been analyzed.

Chapter 5 examines the issue of how to measure the turbulence information necessary in order to apply the proper turbulence phase correction. It presents the structure of a new type of radar system which measures the turbulence information for wavefront correction from the target return. The system presented here shows, for the first time, a way to extract the necessary turbulence information from the target return of a spatially resolved speckle target. The system distinguishes between the turbulence and speckle components of the wavefront distortion in the target return by transmitting multiple wavelengths. These wavelengths are selected in such a way that the speckle distortions in the target returns at the different wavelengths are uncorrelated, but the turbulence distortions in the target returns at the different wavelengths are highly correlated. When such a set of wavelengths is transmitted, then averaging the received phase distortions over the different wavelengths suppresses the speckle component without impairing measurement of the turbulence component.

The performance of this system is then analyzed. The condition under which the use of such a wavefront correction system would be necessary, and the condition under which its use would be possible, are evaluated in order to find the ranges of system parameter values in which such a system would operate. The system performance is then evaluated for parameter values in these ranges. The analysis shows that for these parameter values, the system performance is close to the no-turbulence level.

Chapter 6 discusses the results presented and gives suggestions for further investigation in the areas explored in this thesis.

Chapter 2

Basic Radar System Model

This chapter gives the basic radar system model on which the analysis in this thesis is based. This model includes the overall configuration of the radar, the turbulence, and the target, which is described below. Sections 2.1 through 2.4 describe the transmitter model, the turbulence model, the speckle target reflectivity model, and the receiver front end model. Sections 2.1 through 2.4 are intended mainly as a reference. Thus, it is suggested that in the first reading of this work, these sections should be read mainly for a qualitative understanding of the phenomena that are modeled. In reading the later chapters, the mathematical aspects of these models may be referred to as necessary.

The laser radar model is of a ground-based, monostatic coherent laser radar whose basic structure is shown in Figure 2.1. The transmitter and receiver sections are assumed to employ a common telescope equipped with an appropriate optical transmit/receive switch, as is done in the MIT Lincoln Laboratory test bed radars [3]. The transmitted beam exits the radar aperture and travels through a turbulent atmospheric path. It illuminates a spatially resolved speckle target. The reflected beam travels back toward the radar through an atmospheric propagation path. The received beam enters the radar aperture and is optically combined with a local oscillator (LO) beam, whose frequency is offset from that of the transmitted beam by an intermediate frequency ν_{IF}. The two beams impinge on a photodetector, whose output is bandpass filtered in order to extract the beat signal between the received and LO beams. The filter's output—an intermediate-frequency (IF) signal embedded in shot noise—is further processed in order to extract the desired target information.

The type of imaging considered here is angle-angle imaging, in which the illuminator beam is raster scanned across the target surface in order to measure the target information at each pixel. The type of measurements considered here are intensity (i.e. target reflectivity) and range or velocity. For intensity and velocity measurements, cw or long-pulse operation is used; for range measurements, a short duration transform-limited pulse is used, which does not resolve any range spread of the target within a diffraction-limited pixel.

It is assumed that the target is located high above the earth's atmosphere, at an altitude of at least 100 km. The target may be a satellite, for example. This assumption implies that the turbulence which the beam encounters in traveling to and from the target is statistically independent, due to the long exoatmospheric propagation delay. It also implies that if the target is in a circular orbit around the earth, its angular velocity is slow enough that the target speckle and the atmospheric turbulence can be considered frozen during a typical radar pulse duration or pixel dwell time (see Section 3.3). Both of these consequences of the assumption of high target altitude greatly reduce the physical and mathematical complexity of the analysis.

2.1 Transmitter Model

Let the exit pupil of the radar aperture be at the $z = 0$ plane in a Cartesian coordinate system. The transmitter model characterizes $\mathbf{U}_T(\vec{\rho}; k, t)$, the complex envelope of the optical-frequency field of the transmitted wave (in units of $\sqrt{\mathrm{W/m^2}}$)

as a function of transverse coordinate $\vec{\rho} = (x, y)$, wavenumber k, and time t. It is normalized such that $|\mathbf{U}_T(\vec{\rho}; k, t)|^2$ is the short time average power flow per unit area in the transmitted wave at $(\vec{\rho}, t)$ and wavenumber k. $\mathbf{U}_T(\vec{\rho}; k, t)$ is assumed to be a temporally narrowband field centered at the nominal laser wavenumber k_0, and is related to the real-valued optical-frequency field of the transmitted wave $U_T(\vec{\rho}; k, t)$ by

$$U_T(\vec{\rho}; k, t) = \mathrm{Re}[\mathbf{U}_T(\vec{\rho}; k, t) e^{-ick_0 t}]. \tag{2.1}$$

A scalar field representation is used here, i.e. polarization effects are suppressed. Turbulence generally does not induce depolarization [23], but speckle targets do induce depolarization. However, because only the component of the received wave whose polarization matches that of the LO wave is detected in a heterodyne receiver, a scalar theory suffices if we use as our scalar target reflectivity the component of the reflectivity which converts the incident wave's polarization into the LO wave's polarization.

The complex envelope of the field of the transmitted wave can be decomposed into spatial and temporal components as follows

$$\mathbf{U}_T(\vec{\rho}; k, t) = \sqrt{P_T}\, \xi_T(\vec{\rho})\, \mathbf{s}(t)\, e^{-ic(k-k_0)t}. \tag{2.2}$$

Here, P_T is the peak transmitted power, $\xi_T(\vec{\rho})$ is the transmitted beam pattern normalized to obey $\int d\vec{\rho}\, |\xi_T(\vec{\rho})|^2 = 1$; and $\mathbf{s}(t)$ gives the temporal variation of the transmitted wave during a pulse or during a pixel dwell time, normalized such that for a continuous wave $\mathbf{s}(t) = 1$, and for a pulsed wave $\int dt\, |\sqrt{P_T}\, \mathbf{s}(t)|^2$ is the pulse energy. An offset in the center wavenumber of the transmitted wave from the nominal laser wavenumber is given by $k - k_0$. In Chapter 5 we will analyze the performance of a radar which transmits a multi-wavelength beam; in that case some or all of the transmitted wavenumbers will be offset from k_0.

2.2 Model of Propagation Medium

The refractive index of the earth's atmosphere has random spatio-temporal fluctuations which are referred to as atmospheric turbulence. This turbulence results from the fact that the sun heats up the ground, which nonuniformly radiates the heat into the air above it. Thus, the temperature, and therefore the refractive index, of the air is nonuniform. The refractive index fluctuations result from turbulent mixing of air parcels with approximately 1°C temperature differences. This turbulent mixing occurs in the following manner. Instability of convective flow leads to turbulent mixing at large spatial scales. Beginning at an outer scale size L_0, these turbulent eddies transfer their energy in a lossless manner to successively smaller eddies. At an eddy size equal to the inner scale ℓ_0, viscous damping takes over. Typically $L_0 \sim 10 - 100\,\mathrm{m}$ and $\ell_0 \sim 10^{-3}\,\mathrm{m}$ [27,25], although recent measurements using a stellar interferometer [28] suggest that L_0 may be a few kilometers or larger. The statistical properties of the refractive index fluctuations on spatial scales between ℓ_0 and L_0 are described by the Kolmogorov model [29], on which the propagation model given here is based. Thus, we are assuming that only refractive index fluctuations in this spatial range significantly affect the propagation of the laser beam. This assumption is valid when the propagation distance is greater than ℓ_0^2/λ [30], which is the case for IR wavelengths and the propagation distances considered here.

The effect of the turbulent atmosphere on a wave propagating from the radar aperture to the target is given by the extended Huygens-Fresnel principle [22], namely

$$\begin{aligned} \xi_t\left(\vec{\rho}\,'; k, t + \frac{L}{c}\right) &= e^{-\alpha L/2} \int_R d\vec{\rho}\, \xi_T(\vec{\rho}) \exp[\chi_F(\vec{\rho}\,', \vec{\rho}; k, t) + i\phi_F(\vec{\rho}\,', \vec{\rho}; k, t)] \cdot \\ & \quad \frac{e^{ikL}}{i\lambda L} e^{i\frac{k}{2L}\rho'^2} e^{-i\frac{k}{L}\vec{\rho}\,'\cdot\vec{\rho}}, \end{aligned} \tag{2.3}$$

for far-field or focused near-field propagation, where $\xi_t(\vec{\rho}\,'; k, t + L/c)$ is the illuminator beam pattern at transverse coordinate $\vec{\rho}\,'$ in the plane tangent to the target pixel. In Eq. 2.3, α is the path-averaged atmospheric extinction coefficient, L is the target pixel range, and $\lambda = 2\pi/k$ is the transmitted wavelength. $\chi_F(\vec{\rho}\,', \vec{\rho}; k, t)$ and $\phi_F(\vec{\rho}\,', \vec{\rho}; k, t)$ are the turbulence-induced log-amplitude and phase distortions in the field received at $\vec{\rho}\,'$ in the target pixel plane at time $t + L/c$ from a point source of wavenumber k at $\vec{\rho}$ in the radar aperture region R, where the subscript F indicates propagation in the forward path. Propagation in the return path—from target to radar—can be similarly described:

$$\begin{aligned} \xi_R\left(\vec{\rho}; k, t + \frac{L}{c}\right) &= e^{-\alpha L/2} \int d\vec{\rho}\,'\, \xi_r(\vec{\rho}\,'; k, t) \exp[\chi_R(\vec{\rho}, \vec{\rho}\,'; k, t + L/c) + \\ & \qquad i\phi_R(\vec{\rho}, \vec{\rho}\,'; k, t + L/c)] \frac{e^{ikL}}{i\lambda L} e^{i\frac{k}{2L}\rho'^2} e^{-i\frac{k}{L}\vec{\rho}\,'\cdot\vec{\rho}}, \end{aligned} \tag{2.4}$$

where the subscript R denotes return-path turbulence quantities, and the free space phase curvature in the received wave has been suppressed in accord with far-field or focused near-field operation of a monostatic shared-optics radar. In Eq. 2.4, $\xi_r(\vec{\rho}\,'; k, t)$ is the reflected field in the target pixel plane.

The turbulence-induced log-amplitude and phase fluctuations χ and ϕ are jointly Gaussian random variables in the weak turbulence regime considered here [22]. The mean of ϕ can be taken to be zero without loss of generality, and the variance is almost always large enough that $\langle e^{i\phi} \rangle \approx 0$, where the angular brackets denote an ensemble average. The mean of χ is $-\sigma_\chi^2$ because of energy conservation, where σ_χ^2 is the variance of χ. The variance of χ for a wave with wavenumber k is given by [23]

$$\sigma_\chi^2(k) = 0.56 k^{7/6} \int_0^L d\eta\, C_n^2(\eta)\, (\eta/L)^{\frac{5}{6}}\, (L - \eta)^{\frac{5}{6}} \tag{2.5}$$

where L is the propagation distance, and $C_n^2(\eta)$ is the refractive index structure profile as a function of propagation distance from the source (at $\eta = 0$) to the observation point (at $\eta = L$). Equation 2.5 shows that if the turbulence is concentrated mainly near the source or near the observation point, as it is for a vertical propagation path to a target located high above the atmosphere, then $\sigma_\chi^2(k)$ will be small. The $C_n^2(\eta)$ profile for a vertical propagation path varies with location, time of year, and time of day. An idea of the variability of $C_n^2(\eta)$ can be gotten by looking at measurements of $C_n^2(\eta)$ profiles made under various conditions [24,31]. In this thesis, a pair of commonly used $C_n^2(\eta)$ profiles, shown in Figure 2.2, will be used [32] to illustrate the effect of various turbulence conditions—one represents daytime turbulence conditions and the other represents nighttime conditions. Below are presented some second order statistical properties of χ and ϕ which will be used in this thesis.

The structure function of the log-amplitude fluctuations at wavenumber k is defined as

$$\mathcal{D}_{\chi\chi}(\vec{\rho}\,', \vec{\rho}; k) = \langle(\chi_F(\vec{\rho}_1\,' + \vec{\rho}\,', \vec{\rho}_1 + \vec{\rho}; k, t) - \chi_F(\vec{\rho}_1\,', \vec{\rho}_1; k, t))^2\rangle \tag{2.6}$$

and is equal to [22]

$$\begin{aligned} \mathcal{D}_{\chi\chi}(\vec{\rho}\,', \vec{\rho}; k) \;=\; & 8\pi^2(0.033)k^2 \int_0^L d\eta \int_0^\infty d\kappa\, C_n^2(\eta)\, \kappa^{-11/3} \cdot \\ & \left(1 - J_0\left(\left|\frac{\eta}{L}\vec{\rho}\,' + \left(1 - \frac{\eta}{L}\right)\vec{\rho}\right|\kappa\right)\right) \sin^2\left(\frac{\kappa^2\eta(L-\eta)}{2kL}\right), \end{aligned} \tag{2.7}$$

for Kolmogorov turbulence.

The field distortion induced by atmospheric turbulence has the following correlation functions [22]:

$$\langle \exp(\psi_F(\vec{\rho}\,', \vec{\rho}_1; k, t)) \exp(\psi_F^*(\vec{\rho}\,', \vec{\rho}_2; k, t))\rangle = \exp\left(-\frac{1}{2}(|\vec{\rho}_1 - \vec{\rho}_2|/\rho_0)^{\frac{5}{3}}\right), \tag{2.8}$$

where $\psi(\cdot) \equiv \chi(\cdot) + i\phi(\cdot)$, and ρ_0 is the radar-plane turbulence coherence length. If two point sources are located in the radar plane, and the distance between them is large compared to ρ_0, then the contributions of these two point sources to the field at $\vec{\rho}\,'$ in the target plane would be uncorrelated. This decorrelation between the two contributions would reduce the mean irradiance at $\vec{\rho}\,'$ in the target plane. Also,

$$\langle \exp(\psi_F(\vec{\rho}_1\,', \vec{\rho}; k, t)) \exp(\psi_F^*(\vec{\rho}_2\,', \vec{\rho}; k, t))\rangle = \exp\left(-\frac{1}{2}(|\vec{\rho}_1\,' - \vec{\rho}_2\,'|/\rho_0')^{\frac{5}{3}}\right), \tag{2.9}$$

where ρ_0' is the target-plane coherence length. If a point source is located in the radar plane then ρ_0' is the correlation length in the target plane of the field radiated from this point source. The turbulence coherence lengths ρ_0 and ρ_0' are given by

$$\rho_0 = \left[2.91k^2 \int_0^L d\eta\, C_n^2(\eta) \left(1 - \frac{\eta}{L}\right)^{5/3}\right]^{-3/5}, \tag{2.10}$$

$$\rho_0' = \left[2.91k^2 \int_0^L d\eta\, C_n^2(\eta) \left(\frac{\eta}{L}\right)^{5/3}\right]^{-3/5}, \tag{2.11}$$

where L and η are as defined in connection with Eq. 2.5.

The wavenumber-dependent correlation function of the turbulence-induced field distortion $e^{\psi_F(\vec{\rho}\,',\vec{\rho};k,t)}$ can be found from the wavenumber-dependent correlation functions [33] of $\chi_F(\vec{\rho}\,',\vec{\rho};k,t)$ and $\phi_F(\vec{\rho}\,',\vec{\rho};k,t)$, using the fact that the latter two quantities are jointly Gaussian random functions. The resulting correlation function obeys

$$\begin{aligned}
&|\langle\exp(\psi_F(\vec{\rho}\,',\vec{\rho};k_1,t))\exp(\psi_F^*(\vec{\rho}\,',\vec{\rho};k_2,t))\rangle| = \\
&\exp[-\sigma_\chi^2(k_1) - \sigma_\chi^2(k_2) - \frac{1}{2}(\sigma_\chi^2(k_1) + \sigma_\chi^2(k_2))^2]\cdot \\
&\exp\{-2\pi^2 \int_0^L d\eta \int_0^\infty d\kappa\, \kappa[k_1^2 \cos\left(\frac{\eta}{L}(L-\eta)\kappa^2\frac{1}{k_1}\right) + \\
&k_2^2 \cos\left(\frac{\eta}{L}(L-\eta)\kappa^2\frac{1}{k_2}\right) - \\
&2k_1k_2 \cos\left(\frac{\eta}{L}(L-\eta)\kappa^2\frac{1}{2}(\frac{1}{k_1} - \frac{1}{k_2})\right)]\cdot \\
&C_n^2(\eta)\left[0.033\left(\kappa^2 + \frac{1}{L_0^2}\right)^{-11/6}\right]\},
\end{aligned} \tag{2.12}$$

for forward-path propagation, where L_0 is the outer scale of turbulence. In Eq. 2.12, a modified version [25,34] of the Kolmogorov spectrum of turbulence—which has a $\kappa^{-11/3}$ dependence—is used in order to facilitate numerical evaluation. The turbulence-induced field distortion decorrelates with wavelength variation because light waves at different wavelengths undergo different distortions when perturbed by the same refractive-index inhomogeneities.

Atmospheric turbulence has the following reciprocity property [35]:

$$\psi_R(\vec{\rho},\vec{\rho}\,';k,t) = \psi_F(\vec{\rho}\,',\vec{\rho};k,t). \tag{2.13}$$

Therefore, all of the turbulence properties presented above for forward-path (radar-to-target path) propagation can also be interpreted to apply to return-path (target-to-radar path) propagation.

2.3 Speckle Target Reflectivity Model

The target is assumed to be a speckle target, i.e. a target whose surface is rough on a spatial scale the size of a wavelength. Most real targets will exhibit speckle characteristics when illuminated with a laser beam whose wavelength is of the order of microns, although some do have significant specular features [36]. The term speckle describes the spotty intensity pattern produced at a distance from the target when it is illuminated by temporally coherent light. Speckle is caused by constructive and destructive interference of the light reflected, with random space-varying phase, from different parts of the target surface. If the target surface is moving with respect to the radar, then the interference between the light reflected from different parts of the target will change in time, so that the speckle phase received at the radar will vary in time. However, in this thesis we will assume that this time variation in the speckle occurs slowly enough that it negligibly affects the radar measurements. This assumption is discussed in detail in Section 3.3.

Since the target is assumed to be planar over a pixel region, the reflected and illuminator beam patterns are related through the target reflectivity in this target pixel plane $z = L$, namely

$$\xi_r(\vec{\rho}\,';k,t) = \mathbf{T}(\vec{\rho}\,';k,t)\,\xi_t(\vec{\rho}\,';k,t). \tag{2.14}$$

The wavenumber dependence of the target reflectivity $\mathbf{T}(\vec{\rho}\,';k,t)$ of a rough-surface target can be seen by expressing it as $A(\vec{\rho}\,';t)e^{i2kh(\vec{\rho}\,';t)}$, where $A(\vec{\rho}\,';t)$ is the magnitude of the target reflectivity at $(\vec{\rho}\,';t)$, and $e^{i2kh(\vec{\rho}\,';t)}$ is the phase distortion in the reflected wave at $(\vec{\rho}\,';t)$, where $h(\vec{\rho}\,';t)$ is the deviation of the target surface's height relative to a reference plane at $z = L$ [21]. Thus, waves at two different wavelengths incident on the target undergo different phase distortions upon being reflected from it.

The target reflectivity $\mathbf{T}(\vec{\rho}\,';k,t)$ can be conveniently represented as a random process—that way the exact microstructure of the target surface need not be considered. In a commonly used [11,21] statistical characterization of speckle target reflectivity, the first and second moments of the reflectivity are given by

$$\langle \mathbf{T}(\vec{\rho}\,';k,t)\rangle = 0 \tag{2.15}$$

$$\langle \mathbf{T}(\vec{\rho}_1\,';k,t)\mathbf{T}(\vec{\rho}_2\,';k,t)\rangle = 0 \tag{2.16}$$

$$\langle \mathbf{T}(\vec{\rho}_1\,';k_1,t)\mathbf{T}(\vec{\rho}_2\,';k_2,t)^*\rangle = \lambda_{av}^2\delta(\vec{\rho}_1\,' - \vec{\rho}_2\,')\,\mathcal{T}(\vec{\rho}_1\,')\,e^{-4(\rho_1'/d_T)^2}\,e^{-2(k_1-k_2)^2\sigma_h^2}, \tag{2.17}$$

where $\lambda_{av} = 4\pi/(k_1 + k_2), \mathcal{T}(\vec{\rho}\,')$ is the target's mean squared reflectivity at $\vec{\rho}\,'$, d_T is the target diameter, and σ_h^2 is the variance of the target surface's height fluctuations. The term in Eq. 2.17 which depends on the target size is written separately from $\mathcal{T}(\vec{\rho}\,')$ because the latter term will sometimes be assumed to be constant over subregions of the target surface, while the former term will be retained to indicate the finite target size. Equations 2.15 and 2.16 express the phase randomness in the target reflectivity. Equation 2.17 shows that the correlation length of the target reflectivity is of the order of λ_{av}. For intensity imaging applications, $\mathcal{T}(\vec{\rho}\,')$ is the quantity that the radar tries to measure. Equations 2.14 to 2.17 show that the reflected wave is spatially incoherent and therefore its propagation is nondirectional.

The target reflectivity is also commonly assumed to be a complex Gaussian random process, so that Eqs. 2.15 to 2.17 completely characterize its statistics. The conditions under which the Gaussian reflectivity assumption can be used are: (a) σ_h should be much greater than $2\pi/k_1$ and $2\pi/k_2$ to ensure a uniformly distributed random phase on the scattered wave; and (b) a large number of independent scattering centers should contribute to any given point in the image of the target surface [37].

2.4 Receiver Front End Model

Coherent laser radars use heterodyne detection in order to measure both the phase and amplitude of the target return. In a heterodyne receiver the target return wave, after passing through the radar aperture and receiver optics, is mixed by a beam combiner with the local oscillator (LO) wave. The LO wave is cw, and its frequency is offset from that of the transmitted wave by an intermediate frequency ν_{IF}. The complex envelope of the LO field incident on the photodetector for detection at wavenumber k can be written as

$$\mathbf{U}^{D}_{LO}(\vec{\rho}; k, t) = \sqrt{P_{LO}}\,\xi^{D}_{LO}(\vec{\rho})\, e^{i2\pi\nu_{IF}t} e^{-ic(k-k_0)t}, \tag{2.18}$$

where $\xi^{D}_{LO}(\vec{\rho})$ is the LO beam pattern normalized as $\int d\vec{\rho}\, |\xi^{D}_{LO}(\vec{\rho})|^2 = 1$. The received and LO waves impinge on a photodetector whose output is bandpass filtered. This filter passes the beat signal at frequency ν_{IF}, which is proportional to the field of the received wave.

In the limit of a strong LO wave, the normalized intermediate-frequency (IF) component of the photodetector output can be written as [11,8]

$$\begin{aligned} r(k,t) &\equiv \operatorname{Re}[\mathbf{r}(k,t)e^{-i2\pi\nu_{IF}t}] \\ &= \operatorname{Re}[(\mathbf{y}(k,t)+\mathbf{w}(t))e^{-i2\pi\nu_{IF}t}], \end{aligned} \tag{2.19}$$

where $\mathbf{y}(k,t)$ is the target return component and $\mathbf{w}(t)$ is the LO shot noise component. The target return component is proportional to the spatial overlap integral on the photodetector surface of the received and LO waves. According to the antenna theorem for heterodyne detection [38], this overlap integral can also be evaluated at any other place in the path of the transmitted wave. For the calculations in the next two chapters it is convenient to evaluate this overlap integral in the target plane; in that case the target return component at time t is given by

$$\begin{aligned}\mathbf{y}(k,t) &= \sqrt{P_T\epsilon_{opt}}\,\mathbf{s}\left(t-\frac{2L}{c}\right)\,e^{i(4\pi v_{\parallel}/\lambda)t}\,\cdot \\ &\int d\vec{\rho}\,'\left[\mathbf{T}\left(\vec{\rho}\,';k,t-\frac{L}{c}\right)\,\xi_t\left(\vec{\rho}\,';k,t-\frac{L}{c}\right)\right]\,\xi_{lo}^{*}\left(\vec{\rho}\,';k,t-\frac{L}{c}\right).\end{aligned} \quad (2.20)$$

Here, ϵ_{opt} is the signal power loss of the optical system, $2L/c$ is the target range delay for the observed pixel and $4\pi v_{\parallel}/\lambda$ is the target Doppler shift for the observed pixel, where $v_{\parallel}$ is the radial component of the target velocity. The term in brackets is the reflected beam pattern, and $\xi_{lo}^{*}(\vec{\rho}\,';k,t-L/c)$ is defined as

$$\begin{aligned}\xi_{lo}^{*}\left(\vec{\rho}\,';k,t-\frac{L}{c}\right) &= e^{-\alpha L/2}\int_R d\vec{\rho}\,\xi_{LO}^{*}(\vec{\rho})\,\exp(\psi_R(\vec{\rho},\vec{\rho}\,';k,t))\,\cdot \\ &\frac{e^{ikL}}{i\lambda L}\,e^{i\frac{k}{2L}\rho'^2}\,e^{-i\frac{k}{L}\vec{\rho}\,'\cdot\vec{\rho}}\end{aligned} \quad (2.21)$$

where $\xi_{LO}^{*}(\vec{\rho})$ is the LO beam pattern, $\xi_{LO}^{D*}(\vec{\rho})$, back-propagated to the radar aperture. Because of the reciprocity of atmospheric turbulence (Eq. 2.13), Eq. 2.21 can be interpreted as the beam pattern that would result from back-propagation of the LO beam pattern to the target through the prevailing atmospheric turbulence conditions. Thus, it is referred to as the back-propagated LO (BPLO) beam pattern. The LO shot noise $\mathbf{w}(t)$ is a zero-mean circulo-complex Gaussian random process such that

$$\langle \mathbf{w}(t_1)\mathbf{w}^{*}(t_2)\rangle = \frac{h\nu_0}{\eta}\delta(t_1-t_2), \quad (2.22)$$

where $h\nu_0$ is the photon energy at the center frequency of the transmitted field, η is the photodetector's quantum efficiency.

As mentioned above, the IF component of the photodetector output, $r(k,t)$, is passed through a bandpass filter. Equivalently, the baseband complex envelope of $r(k,t)$, i.e. $\mathbf{r}(k,t)$, is lowpass filtered. The particular form of this lowpass filter depends on the transmitted pulse shape $\mathbf{s}(t)$, and on the type of target measurement that is being made. If the transmitted wave is cw, e.g. for intensity or velocity measurements, then the lowpass filter has the following frequency response

$$\mathbf{H}(f) = \begin{cases} 1, & |f| \leq B/2 \\ 0, & \text{otherwise,} \end{cases} \tag{2.23}$$

so that B is the unilateral bandwidth of the IF bandpass filter. It is assumed that B is large enough to pass the target return in an undistorted way. The target-return component of the lowpass filter's output is

$$\ell(k,t) = \sqrt{P_T \epsilon_{opt}} e^{i(4\pi v_{\|}/\lambda)t} \int d\vec{\rho}\,' \, \mathbf{T}\left(\vec{\rho}\,'; k, t - \frac{L}{c}\right) \xi_t\left(\vec{\rho}\,'; k, t - \frac{L}{c}\right) \xi_{lo}^{*}\left(\vec{\rho}\,'; k, t - \frac{L}{c}\right). \tag{2.24}$$

The LO shot noise component of the filter's output is denoted by $\mathbf{n}(t)$, such that $\mathbf{n}(t)$ is a zero-mean circulo-complex Gaussian random process with

$$\langle |\mathbf{n}(t)|^2 \rangle = \frac{h\nu_0 B}{\eta}. \tag{2.25}$$

If the transmitted wave is pulsed and the range is being measured, then the lowpass filter is a matched filter with the following impulse response

$$\mathbf{h}(t) = \sqrt{P_T B / E_T}\, \mathbf{s}^{*}(-t), \tag{2.26}$$

where the factor $\sqrt{P_T B/E_T}$ is included so that the shot noise component of the filter output, $\mathbf{n}(t)$, has the variance of Eq. 2.25. It is assumed that in the case of range measurements the Doppler frequency shift in Eq. 2.20 is zero or that it is tracked and cancelled in the input to the filter. This assumption simplifies the analysis, and the frequency tracking could be carried out by shifting the LO frequency in such a way as to keep the frequency spectrum of the target return centered about the frequency ν_{IF}. This assumption allows an IF filter with a narrower bandwidth to be used, which reduces the LO shot noise contribution to the IF signal. Using this assumption, the target-return component of the filter output is given by

$$\begin{aligned} \ell(k,\tau) &= \sqrt{P_T \epsilon_{opt}} \int d\vec{\rho}\,' \, \mathbf{T}\left(\vec{\rho}\,'; k, \tau - \frac{L}{c}\right) \xi_t\left(\vec{\rho}\,'; k, \tau - \frac{L}{c}\right) \xi_{lo}^{*}\left(\vec{\rho}\,'; k, \tau - \frac{L}{c}\right) \cdot \\ &\quad \sqrt{P_T B / E_T} \int dt\, \mathbf{s}(t - 2L/c)\, \mathbf{s}^{*}(t - \tau), \end{aligned} \tag{2.27}$$

where τ, the time at which the measurement is made, is a time delay in the vicinity of the expected round-trip propagation delay. In writing Eq. 2.27, it is assumed that the time variation in the target reflectivity and in the target-plane beam patterns is negligible during a pulse duration. This assumption is examined in Section 3.3, and is shown to be valid in cases of interest. Passing the photodetector output through the matched filter whose baseband version is Eq. 2.26 allows the range L to be measured from the received pulse's propagation delay, since $\langle|\ell(k,\tau)|^2\rangle$ peaks at time delay $\tau = 2L/c$. Thus, the range estimate is $c/2$ times the peak in τ of the filter output. This range measurement procedure gives the maximum likelihood range estimate in the absence of turbulence [18].

If the transmitted wave is pulsed and the velocity is being measured, then the lowpass filter performs a windowed Fourier transform; it has the following impulse response

$$\mathbf{h}(t) = \sqrt{P_T B/E_T}\,\mathbf{s}^*(-t)\,e^{i2\pi f t}, \tag{2.28}$$

where f is a frequency in the vicinity of the expected Doppler frequency shift. It is assumed that in the case of velocity measurements, the target pixel range L is known. This assumption simplifies the analysis. Furthermore, it allows the received pulse to be measured at the moment at which it arrives, thereby increasing the magnitude of the target return. We again assume that the time variation of the target reflectivity and of the target-plane beam patterns is negligible during a pulse duration or a pixel dwell time. Using these assumptions, the target-return component of the filter output is given by

$$\begin{aligned} \ell(k,f) \;=\; & \sqrt{P_T\epsilon_{opt}}\int d\vec{\rho}\,'\,\mathbf{T}\left(\vec{\rho}\,';k,t-\frac{L}{c}\right)\xi_t\left(\vec{\rho}\,';k,t-\frac{L}{c}\right)\xi_{lo}^*\left(\vec{\rho}\,';k,t-\frac{L}{c}\right)\cdot \\ & \sqrt{P_T B/E_T}\int dt\,|\mathbf{s}(t-2L/c)|^2\,e^{-i2\pi(f-2v_\parallel/\lambda)t} \end{aligned} \tag{2.29}$$

at the observation time $2L/c$, the round trip propagation time. The variance of the LO shot noise component of the filter output, $\mathbf{n}(t)$, is given by Eq. 2.25. Passing the photodetector output through the matched filter whose baseband version is Eq. 2.28 allows the radial component of the velocity, $v_{\parallel}$, to be measured from the received wave's frequency shift, since $\langle|\ell(k,f)|^2\rangle$ peaks at frequency shift $f = 2v_{\parallel}/\lambda$. Thus, the velocity estimate is $\lambda/2$ times the peak in f of the filter output. This velocity measurement procedure gives the maximum likelihood velocity estimate in the absence of turbulence [18].

The effects of turbulence on radar performance can be found by examining the turbulence effects on $\ell(k,\cdot)$, the baseband complex envelope of the IF signal from which the target information is obtained. Eqs. 2.24, 2.27, and 2.29 show that the turbulence affects this IF signal via the illuminator and BPLO beam patterns. These turbulence effects are examined in more detail in the next chapter.

Note that in this chapter the wavenumber dependence of the models is explicitly highlighted, because we will ultimately be concerned with multiwavelength radar operation. The material in the next two chapters, however, is for the usual case of single-wavelength operation.

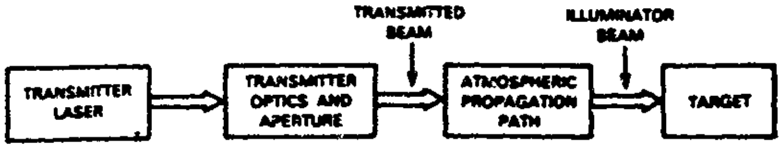

a) TRANSMITTER-TO-TARGET PATH

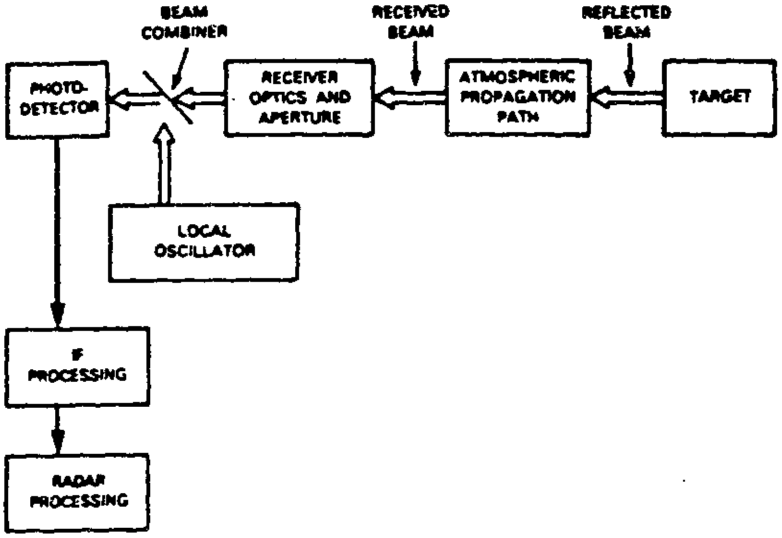

b) TARGET-TO-RECEIVER PATH

Figure 2.1: Coherent laser radar system configuration.

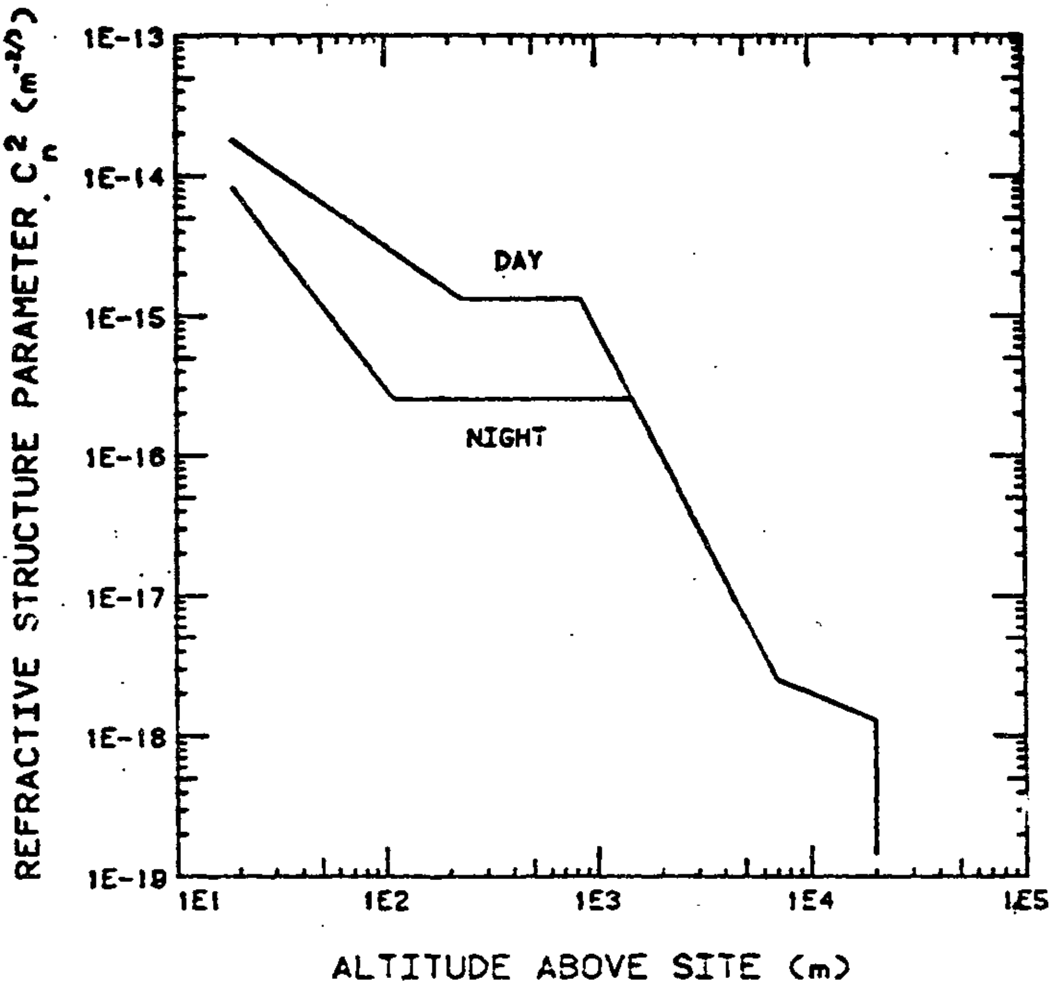

Figure 2.2: Vertical distribution of the refractive index structure constant C_n^2. Above 1 km altitude the value of C_n^2 is independent of whether it is daytime or nighttime. Below 1 km distinct values of C_n^2 are shown for daytime and nighttime. From Reference [32].

Chapter 3

Radar Performance Degradation Due to Turbulence

Now that we have developed models for the IF signal from which radar measurements are made, and for the turbulence and speckle processes which affect this IF signal, we can derive formulas for the effects of turbulence and speckle on the radar's performance. These formulas are functions of parameters of the radar system, the turbulence, and the speckle target. In this chapter the effects of atmospheric turbulence on the speckle target results for spatial resolution, carrier-to-noise ratio (CNR), and the resolution and accuracy of range and velocity measurements are derived. It is found that for large-aperture radars (i.e. those for which $d \gg \rho_0$), the speckle-target spatial resolution, CNR, and range and velocity accuracy are all significantly degraded by turbulence.

The uncorrected transmitted beam pattern is taken to be the Gaussian beam given by

$$\xi_0(\vec{\rho};t) = \sqrt{\frac{16}{\pi d^2}}e^{-8\rho^2/d^2} \tag{3.1}$$

in the radar's exit aperture, where d is the aperture diameter. The uncorrected LO beam pattern propagated to the radar aperture is also taken to be the Gaussian beam of Eq. 3.1. The intensity of these beams at the edge of the aperture is e^{-4} times its value at the center. Thus, the effect of the truncation of these beams by the finite-sized aperture can be expected to be small. A quantitative analysis [39] has shown that for the beam pattern of Eq. 3.1, the effect of truncation is actually small. Therefore, the effect of the truncation is neglected here, so that when the beam pattern of Eq. 3.1 is transmitted, the aperture size will be approximated as being infinite.

3.1 Spatial Resolution

In angle-angle imaging, the target is imaged by measuring a target characteristic at each pixel of the target surface. The spatial resolution of the image is the pixel size, which is given by the size of the target region that contributes to the signal power in a radar measurement. The mean target-return power P_R from a particular pixel at a given time is given by $\langle|\ell|^2\rangle$, where ℓ is given by Eq. 2.24, 2.27, or 2.29, depending on the type of measurement being made. For the cw case, $P_R = \langle|\ell(t)|^2\rangle$, which can be found from Eqs. 2.24 and 2.17 to be

$$P_R = P_T \epsilon_{opt} \lambda^2 \int d\vec{\rho}\,' \, T(\vec{\rho}\,') e^{-4(\rho'/d_T)^2} \langle|\xi_t(\vec{\rho}\,';t)\xi_{lo}^*(\vec{\rho}\,';t)|^2\rangle. \tag{3.2}$$

For the case of range measurements, $P_R = \langle|\ell(2L/c)|^2\rangle$ is the received power at time $2L/c$, the propagation delay of the received pulse, and it can be found from Eq. 2.27 to be Eq. 3.2 with P_T replaced by $E_T B$. For the case of velocity measurements, $P_R = \langle|\ell(2v_{\|}/\lambda)|^2\rangle$ is the received power at frequency $2v_{\|}/\lambda$, the frequency shift in the received wave, and it can be found from Eq. 2.29 to be Eq. 3.2 with P_T replaced by $E_T B$.

When the target is spatially resolved, the mean squared product of the two beam patterns determines how large a region of the target surface contributes to the signal power. Therefore, the spatial resolution, r_{res}, is defined to be the radius to the e^{-2} attenuation point of this mean squared product.

When the turbulence fluctuations incurred in the forward and return paths are independent—as is the case for a target located high above the earth's atmosphere because of the large round trip exoatmospheric propagation delay—the illuminator and BPLO beam patterns are statistically independent. The spatial resolution can then be found in terms of the product of the individual mean squared beam patterns. The mean squared illuminator beam pattern can be found from Eq. 2.3 by using Eq. 2.8 to evaluate the turbulence average, and by using the beam pattern of Eq. 3.1 for $\xi_T(\vec{\rho})$. The result is

$$\langle|\xi_t(\vec{\rho}'; t)|^2\rangle = e^{-\alpha L}\frac{\pi}{4}\left(\frac{d}{\lambda L}\right)^2 \frac{1}{1+\frac{d^2}{8\rho_0^2}} \exp\left[-\frac{\pi^2}{4}\left(\frac{d\rho'}{\lambda L}\right)^2 \Big/ \left(1+\frac{d^2}{8\rho_0^2}\right)\right]. \tag{3.3}$$

Two approximations have been made in deriving Eq. 3.3. First, the integral in Eq. 2.3 has been extended to infinity, i.e. the truncation in the transmitted beam pattern has been neglected. Second, the square-law approximation [40] has been used in Eq. 2.8 to replace the exponent of 5/3 by 2. The mean squared BPLO beam pattern can be found from Eq. 2.21 in the same way, by using the reciprocity property of Eq. 2.13, and the result is the same as the mean squared illuminator beam pattern of Eq. 3.3. Therefore, the spatial resolution is given by

$$r_{res} = \frac{2\lambda L}{\pi d}\sqrt{1+\frac{d^2}{8\rho_0^2}} \tag{3.4}$$

when the transmitted and LO beam patterns are given by Eq. 3.1. The spatial resolution in the presence of turbulence has been found previously in the form of the beam spread in a beam that has propagated through turbulence [25].

The spatial resolution in two limiting cases can be found from Eq. 3.4. At one extreme, the well known result for the diffraction-limited spatial resolution [9] can be found by letting $\rho_0 \to \infty$, and the result is $2\lambda L/(\pi d)$. For other definitions of r_{res} or for other beam patterns, the factor $2/\pi$ may be replaced by a different constant. At the other extreme, when $d \to \infty$ the spatial resolution saturates at its turbulence-limited value, $2\lambda L/(\pi\sqrt{8}\rho_0)$.

The degradation in spatial resolution due to turbulence is the ratio of Eq. 3.4 to the diffraction-limited resolution, $2\lambda L/(\pi d)$. The degradation in spatial resolution is shown in Figure 3.1 as a function of d/ρ_0. When $d \gg \rho_0$ prevails, the transmitted and BPLO beams have significant turbulence-induced distortions, and the resulting beam spreading significantly degrades the spatial resolution. In this case the spatial resolution saturates at its turbulence-limited value, as mentioned above.

3.2 Carrier-to-noise Ratio

The CNR at a given time is defined as the ratio of the mean target return power $\langle|\ell(\cdot)|^2\rangle$ to the mean noise power $\langle|\mathrm{n}(t)|^2\rangle$ in the filtered IF signal. Using Eq. 2.25 shows that CNR $= \eta P_R/(h\nu_0 B)$. To simplify evaluation of Eq. 3.2 for P_R, it will be assumed that the mean squared target reflectivity $\mathcal{T}(\vec{\rho}\,') = \rho/\pi$ over the region illuminated by the two beam patterns, where ρ is the diffuse reflectivity of that region. Then, using Eq. 3.3 for the mean squared beam patterns of Eq. 3.2 gives

$$\mathrm{CNR} = \mathrm{CNR}_0 \cdot \left[1 + \frac{d^2}{8\rho_0^2}\right]^{-1} \left[1 + 8\left(\frac{\lambda L}{\pi d d_T}\right)^2 \left(1 + \frac{d^2}{8\rho_0^2}\right)\right]^{-1}, \tag{3.5}$$

where

$$\mathrm{CNR}_0 \equiv \frac{\eta P_T \epsilon_{opt}}{h\nu_0 B}\, \rho e^{-2\alpha L}\, \frac{d^2}{8L^2} \tag{3.6}$$

is the no-turbulence speckle target CNR for an infinite target for the cw case. For the pulsed wave case, P_T/B would be replaced by E_T. The first term after CNR_0 in Eq. 3.5 is the reduction in CNR due to the reduction in heterodyne mixing efficiency [12,13] caused by turbulence-induced beam distortions. The second term after CNR_0 is the CNR reduction due to power loss when part of the illuminator and BPLO beam patterns spill over the edge of the target and thus do not contribute to the target return, i.e. when the target approaches the unresolved condition. Note that the turbulence-induced enlargement of the illuminator and BPLO beam patterns on target exacerbates this loss term. As with the spatial resolution, when $d \gg \rho_0$ the

CNR saturates at its turbulence-limited value, and is thus significantly degraded relative to its no-turbulence value. This dependence of the CNR on d/ρ_0 agrees with previously obtained results [12,13].

Figure 3.2 shows the CNR reduction due to turbulence as a function of d/ρ_0 for various target diameters. The top curve is for an infinite target. In this case, the CNR is close to the no-turbulence value when $d/\rho_0 \ll 1$, but for d/ρ_0 close to 10, the CNR is significantly reduced because of the reduction in heterodyne mixing efficiency. In the next curve, $(dd_T/(\lambda L))^2 = 10$, so that the target is spatially resolved by the diffraction-limited beam patterns, and also by the turbulence-limited beam patterns for small values of d/ρ_0. In this case the CNR reduction factor is close to the infinite-target result for small d/ρ_0, but for larger values of d/ρ_0 the target becomes spatially unresolved by the turbulence-limited beam patterns, and therefore the CNR reduction is increased because of the loss of part of the energy of the beam patterns. The bottom curve is for $(dd_T/(\lambda L))^2 = 1$, so that the target is spatially unresolved. In this case the CNR is significantly reduced for all values of d/ρ_0, due to the reduction in heterodyne mixing efficiency for large d/ρ_0, and due to the loss of part of the energy of the beam patterns.

3.3 Range and Velocity Resolution

The range resolution is a measure of the smallest separation between two target ranges the radar can measure. Because the range is measured from the value at which $|\ell(\tau)|^2$ peaks, the narrower the peak of $|\ell(\tau)|^2$ is, the better is the range resolution. Thus, the range resolution is defined as $c/2$ times the full width between the e^{-2} attenuation points of $\langle|\ell(\tau)|^2\rangle$, and in the absence of turbulence is given by

$$z_{res} = \frac{\sqrt{2}c}{\sigma_\omega}, \tag{3.7}$$

where σ_ω is the root-mean-square (rms) radian-frequency bandwidth of $\mathbf{s}(t)$ [41]. In the presence of turbulence, the target-return of the filtered IF signal is (see Eq. 2.27)

$$\begin{aligned} \ell(\tau) &= \sqrt{P_T\epsilon_{opt}}\sqrt{P_T B/E_T}\int dt\, \mathbf{s}^*(t-\tau)\mathbf{s}(t-2L/c)\cdot \\ &\quad \left[\int d\vec{\rho}'\, \mathbf{T}\left(\vec{\rho}';t-\frac{L}{c}\right)\xi_t\left(\vec{\rho}';t-\frac{L}{c}\right)\xi_{lo}^*\left(\vec{\rho}';t-\frac{L}{c}\right)\right]. \end{aligned} \tag{3.8}$$

If the spatial overlap integral—the term in brackets in Eq. 3.8—does not vary during the duration of $\mathbf{s}(t)$, then the width of the peak of $|\ell(\tau)|^2$ depends only on the pulse shape $\mathbf{s}(t)$. However, if this bracketed term does vary during the duration of $\mathbf{s}(t)$, then the peak is broadened, and the range resolution is degraded. Physically, if the received pulse has temporal modulation due to time variation of the target reflectivity and/or the turbulence, then it is more difficult to determine the arrival time of the peak of the pulse, i.e. the pulse's propagation delay. Thus, the range resolution is degraded if the target reflectivity $\mathbf{T}(\vec{\rho}';t)$ and/or the turbulence vary on time scales short compared to the pulse duration. For range measurements based on transform-limited pulses, the pulse duration would be of the order of nanoseconds to hundreds of nanoseconds in order to achieve a range resolution of tens of centimeters to tens of meters. (Microsecond durations are used in chirp pulse-compression ranging systems, but the pulse's bandwidth would be of the order of 10^7 to 10^9 Hz to give the same range resolution.)

It is assumed here for simplicity that the reflectivity of the target pixel varies negligibly during microsecond time scales, although such an assumption may not be valid for a spinning or tilting speckle target. For example, consider a target that is tilting about an axis perpendicular to the direction of propagation. If the tilt angle is of the order of d/L or larger, then the received speckle field decorrelates [21]. If d is of the order of a meter, and L is of the order of 100 km, then this tilt angle is of the order of 10 μrad. Thus, if the target undergoes a tilt of such an angle during a pulse duration or pixel dwell time (in the case of velocity measurements), then the range or velocity resolution is degraded. More information on the effects of target tilting and/or rotation on speckle decorrelation can be obtained from Reference [21].

Since we are assuming that the target pixel reflectivity varies negligibly during a pulse duration, it follows that any variations in the spatial overlap integral which would degrade the range resolution would come from temporal variations in $\xi_t(\vec{\rho}\,'; t - L/c)$ and in $\xi_{i_o}^*(\vec{\rho}\,'; t - L/c)$. If the target is a satellite located high above the atmosphere, such variations could come from turbulence-induced pulse spreading, temporal turbulence fluctuations, or turbulence or speckle variation due to beam slewing. Turbulence measurements from fluctuations of starlight have shown that multipath pulse spreading would be less than picoseconds. The temporal turbulence fluctuations are due mainly to the wind blowing the spatial nonuniformities across the aperture region [24]. Therefore, the time scale of IF signal decorrelation due to temporal turbulence fluctuations would be of the order of d/v_w (the time it takes for the spatial nonuniformities to travel across the aperture region), where v_w is the component of the wind velocity perpendicular to the propagation path. For aperture diameters of a few meters, and wind speeds of a few meters per second, this time scale is of the order of seconds. Thus, both multipath spreads and temporal turbulence fluctuations are negligible for nanosecond to microsecond pulses. The decorrelation time of turbulence due to beam slewing is of the order of $\rho_0'/v_\perp$, where $v_\perp$ is the component of the target velocity perpendicular to the propagation path. This time scale is the time it would take for a point on the target to move across a target-plane turbulence coherence area. For a satellite in a circular orbit around the earth at an altitude of 100 km or more, and the $C_n^2(\eta)$ profile used here to represent typical nighttime turbulence conditions, this decorrelation time is approximately 10 milliseconds or longer, which is much longer than the pulse duration. The speckle decorrelation coefficient for beam slewing is $e^{-(4v_\perp t_p/d)^2}$ for the beam pattern of Eq. 3.1, where t_p is the pulse duration [21]. For the satellite altitudes mentioned above and an aperture diameter of 3 meters, this coefficient is e^{-2} when the pulse duration is approximately 0.1 msec or longer, again much longer than the pulse duration.

The velocity resolution is a measure of the smallest separation between two target velocities the radar can measure. Because the velocity is measured from the value of f at which $|\ell(f)|^2$ peaks, the narrower the peak of $|\ell(f)|^2$ is, the better is the velocity resolution. Thus, the velocity resolution is defined as the full width between the e^{-2} attenuation points of $|\ell(f)|^2$, and in the absence of turbulence is given by

$$v_{res} = \frac{\lambda}{\sqrt{2}\pi\sigma_t}, \tag{3.9}$$

where σ_t is the rms time duration of $\mathbf{s}(t)$ [41]. In the presence of turbulence, the target-return component of the filtered IF signal is (see Eq. 2.29)

$$\begin{aligned} \ell(f) \;=\; & \sqrt{P_T \epsilon_{opt}}\sqrt{P_T B/E_T}\int dt\,|\mathbf{s}(t-2L/c)|^2 e^{-i2\pi(f-2v_{\parallel}/c)t}\,\cdot \\ & \left[\int d\vec{\rho}'\,\mathbf{T}\left(\vec{\rho}';t-\frac{L}{c}\right)\xi_t\left(\vec{\rho}';t-\frac{L}{c}\right)\xi_{lo}^{*}\left(\vec{\rho}';t-\frac{L}{c}\right)\right]. \end{aligned} \tag{3.10}$$

If the spatial overlap integral of Eq. 3.10 does not vary during the duration of $\mathbf{s}(t)$ (or during a pixel dwell time in the cw case), then the width of the peak of $|\ell(f)|^2$ depends only on the pulse shape $\mathbf{s}(t)$, or on the pixel dwell time in the cw case. However, if the spatial overlap integral does vary during the duration of $\mathbf{s}(t)$ or during the dwell time, then the peak is broadened, and the velocity resolution is degraded. Physically, temporal modulation in the received wave due to time variation of the target reflectivity and/or the turbulence introduce additional frequency components into the received wave, making it more difficult to determine the frequency shift due to target motion. Thus, the velocity resolution is degraded if the reflectivity of the target pixel and/or the turbulence have significant variation other than that due to the Doppler shift during the pixel dwell time. For velocity measurements, the pixel dwell time would be of the order of tens of microseconds in order to achieve a velocity resolution of a few meters per second at the CO_2 laser wavelength. (For shorter wavelengths, shorter pulses would give the same velocity resolution.) The above discussion of range resolution shows that turbulence-induced multipath spreading is negligible for such dwell times. It also shows that the correlation time of turbulence fluctuations, as well as the turbulence and speckle decorrelation times due to beam slewing, are generally significantly longer than such dwell times.

The above discussion shows that if target spinning or tilting during a pulse duration or a pixel dwell time can be neglected, then the range and velocity resolution are not significantly degraded by turbulence or speckle for pulse durations or pixel dwell times in the range of nanoseconds to tens of microseconds when the target is a satellite in a circular orbit around the earth at an altitude of at least 100 km.

3.4 Range and Velocity Accuracy

The accuracy of a range or velocity measurement is defined as the rms difference between the estimated value and the actual value. Our derivation of range and velocity measurement accuracy in the presence of turbulence is based on a previous analysis [18] of the range and velocity measurement accuracy in the absence of turbulence. We begin with the range measurement analysis—the velocity measurement analysis will follow directly from a duality argument. The range measurement analysis employs a range bin model, in which a range uncertainty interval of length Δz is represented as a set of N_{bin} bins of size z_{res}, the range resolution. If a range measurement is in an incorrect bin, it is said to be anomalous. The mean-squared error can be expressed in terms of the local mean-squared error, i.e. the mean-squared error of a measurement which is not anomalous, and the global mean-squared error, i.e. the mean-squared error of an anomalous measurement [18], as follows:

$$\begin{aligned}\langle (L-\hat{L})^2\rangle &= \langle (L-\hat{L})^2\rangle|_{\text{no anomaly}}\cdot(1-\Pr(A)) + \\ &\quad \langle (L-\hat{L})^2\rangle|_{\text{anomaly}}\cdot \Pr(A). \qquad (3.11)\end{aligned}$$

Here L and $\hat{L}$ are the actual and estimated target pixel ranges, and Pr(A) is the probability that the range measurement is anomalous.

It is assumed that the signal in the correct range bin is due to the target return and shot noise, that the signals in all other bins are due only to shot noise, and that the shot noises in any two bins are statistically independent [18]. Therefore, the probability of no anomaly is the probability that the shot noise power in every incorrect bin is smaller than the total power in the correct bin. The shot noise power in each bin is exponentially distributed with mean $h\nu_0 B/\eta$, according to Eq. 2.25. In the absence of turbulence, the total power in the correct bin is also exponentially distributed with mean $\langle|\ell(2L/c)|^2\rangle + h\nu_0 B/\eta$, where $\ell(\tau)$ is given by Eq. 2.27 using the no-turbulence target-plane beam patterns. Therefore, in the absence of turbulence, the probability of anomaly is [18]

$$\Pr(A) = 1 - \int_0^\infty du\, \frac{1}{1+\text{CNR}}\, e^{-u/[1+\text{CNR}]}\,(1-e^{-u})^{N_{bin}-1}, \qquad (3.12)$$

where $\text{CNR} = \eta\langle|\ell(2L/c)|^2\rangle/(h\nu_0 B)$ evaluated in the no-turbulence case. The anomaly probability in the presence of turbulence can be found from the probability in the no-turbulence case by taking CNR in Eq. 3.12 to be the instantaneous carrier-to-noise ratio for a particular turbulence realization, and then averaging over the turbulence statistics. Because the time scales of the turbulence and speckle fluctuations in the target return are longer than the pulse duration or pixel dwell time, the carrier-to-noise ratio conditioned on turbulence can be expressed as $\text{CNR}_T \cdot x$, where CNR_T is the carrier-to-noise ratio in the presence of turbulence (given in Section 3.2), and x is a unity mean random variable which represents the randomness in the instantaneous carrier-to-noise ratio. The variable x is defined as

$$x \equiv \langle|\ell|^2\rangle|_{\text{speckle}} / \langle|\ell|^2\rangle|_{\text{speckle, turbulence}}. \tag{3.13}$$

The anomaly probability in the presence of turbulence is therefore

$$\begin{aligned}
\Pr(A) &= \int_0^\infty dX\, p_x(X) \Pr(A|x = X) \\
&= 1 - \int_0^\infty dX\, p_x(X) \int_0^\infty dv\, \frac{1}{1 + \text{CNR}_T X}\, e^{-v/(1+\text{CNR}_T X)} \,. \\
&\quad (1 - e^{-v})^{N_{bin}-1}.
\end{aligned} \tag{3.14}$$

The next step in evaluating the range accuracy is to find the local mean-squared range estimation error. Given that there has not been an anomaly, the mean squared error can be approximated by the Cramer-Rao lower bound [18]. The Cramer-Rao bound is expressed in terms of the likelihood ratio, i.e. the ratio of the probability distribution of $\ell(\tau)$ given that there is a signal to the probability distribution of $\ell(\tau)$ due to shot noise alone [42]. The likelihood ratio in the absence of turbulence is

$$\Lambda(\ell) = \frac{1}{\pi\langle|\mathbf{n}|^2\rangle(1 + \text{CNR})} \exp\left(-\frac{|\ell|^2}{\langle|\mathbf{n}|^2\rangle(1 + \text{CNR})}\right) \Big/ \frac{1}{\pi\langle|\mathbf{n}|^2\rangle} \exp\left(-\frac{|\ell|^2}{\langle|\mathbf{n}|^2\rangle}\right). \tag{3.15}$$

The Cramer-Rao bound is given by

$$\text{CR bound} = \frac{c^2}{4}\left[\left\langle -\frac{\partial^2 \ln \Lambda}{\partial \tau^2}\Big|_{\tau=2L/c}\right\rangle\right]^{-1}. \tag{3.16}$$

In the absence of turbulence this bound can be found from Eqs. 3.16, 3.15, and 2.27 to be [41,42]

$$\text{CR bound} = z_{res}^2(\text{CNR} + 1)/(4\text{CNR})^2 \tag{3.17}$$

where z_{res} is given by Eq. 3.7. The Cramer-Rao bound in the presence of turbulence is difficult to find because the likelihood ratio in the presence of turbulence is difficult to evaluate. Therefore, the local range accuracy in the presence of turbulence will be approximated by a weaker lower bound than the Cramer-Rao bound [43], as follows:

$$\langle (L-\hat{L})^2 \rangle |_{\text{no anomaly}} \approx$$
$$\frac{c^2}{4}\left[\left\langle\left\langle -\frac{\partial^2 \ln[\Lambda|\text{turbulence}]}{\partial \tau^2}\Big|_{\tau=2L/c}\right\rangle_{\text{speckle, shot noise}}\right\rangle_{\text{turbulence}}\right]^{-1}. \quad (3.18)$$

That is, the second derivative is found of the log likelihood ratio for a particular turbulence realization, and is then averaged over speckle and shot noise. This result is then averaged over turbulence, and the reciprocal of the expression obtained is the lower bound for the local mean-squared error. Thus, the local mean-squared error in the presence of turbulence can be obtained from Eq. 3.17 as follows:

$$\langle (L-\hat{L})^2 \rangle |_{\text{no anomaly}} \approx z_{res}^2 \left[\int_0^\infty dX\, p_x(X)\, \frac{(4\text{CNR}_T X)^2}{\text{CNR}_T X + 1}\right]^{-1}. \quad (3.19)$$

The remaining term to be evaluated in Eq. 3.11 is the global mean-squared range estimation error. Given that there has been an anomaly, $\hat{L}$ is derived from a range bin in which the power is due only to shot noise. Since the shot noise statistics are the same for all bins, $\hat{L}$ will be a uniformly distributed random variable over the $N_{bin}-1$ anomalous bins in the range uncertainty interval. Assuming that L is equally likely to be anywhere within this uncertainty interval, we have that [18]

$$\langle (L-\hat{L})^2 \rangle |_{\text{anomaly}} \approx (N_{bin} z_{res})^2/6, \quad (3.20)$$

where $N_{bin} z_{res} = \Delta z$ is the size of the range uncertainty interval. The normalized range estimation error can now be evaluated, using Eqs. 3.11, 3.19, and 3.20, with the following result:

$$\frac{\sqrt{\langle (L-\hat{L})^2 \rangle}}{z_{res}} = \left[\left\langle \frac{(4\text{CNR}_T x)^2}{\text{CNR}_T x + 1}\right\rangle^{-1} \cdot (1-\Pr(A)) + \frac{N_{bin}^2}{6}\cdot \Pr(A)\right]^{1/2}, \quad (3.21)$$

where the average is over x, and Pr(A) is given by Eq. 3.14. The final step in evaluating the range accuracy is to find $p_x(X)$. The random variable x, as defined in Eq. 3.13, is equal to

$$x = \frac{\int d\vec{\rho}\,' e^{-4\rho'^2/d_T^2} |\xi_t(\vec{\rho}\,')|^2 |\xi_{l_o}^*(\vec{\rho}\,')|^2}{\int d\vec{\rho}\,' e^{-4\rho'^2/d_T^2} \langle |\xi_t(\vec{\rho}\,')|^2 \rangle \langle |\xi_{l_o}^*(\vec{\rho}\,')|^2 \rangle}, \tag{3.22}$$

where the time dependence of the beam patterns has been suppressed for brevity, and it has been assumed that $\mathcal{T}(\vec{\rho}\,') = \rho/\pi$. On the average, the power in the illuminator and BPLO beam patterns is concentrated near their centers, $\vec{\rho}\,' = \vec{0}$. Therefore, the randomness of each of these beam patterns will be approximated by the randomness at its center, namely,

$$|\xi_t(\vec{\rho}\,')|^2 \approx |\xi_t(\vec{0})|^2 \cdot \frac{\langle |\xi_t(\vec{\rho}\,')|^2 \rangle}{\langle |\xi_t(\vec{0})|^2 \rangle} \tag{3.23}$$

for the illuminator beam pattern. A similar approximation will be made for the BPLO beam pattern, so that x will be taken to satisfy

$$x \approx \frac{|\xi_t(\vec{0})|^2}{\langle |\xi_t(\vec{0})|^2 \rangle} \cdot \frac{|\xi_{l_o}^*(\vec{0})|^2}{\langle |\xi_{l_o}^*(\vec{0})|^2 \rangle}. \tag{3.24}$$

When $d \gg \rho_0$, then $\xi_t(\vec{\rho}\,')$ and $\xi_{l_o}^*(\vec{\rho}\,')$ are each sums of contributions from many coherence areas in the radar plane. These two beam patterns can therefore be regarded as Gaussian random functions, by the central limit theorem [44]. Furthermore, the two beam patterns are zero-mean because of the large variance of the turbulence phase. Thus, the expression for x in Eq. 3.24 is the product of two independent, unity mean, exponential random variables, and $p_x(X)$ can be derived accordingly. In summary, the normalized range accuracy in the presence of turbulence is given by Eq. 3.21, with Pr(A) given by Eq. 3.14, and with the appropriate $p_x(X)$.

Because of the duality between range and velocity measurements [18], the velocity estimation error is derived in the same way as is the range estimation error. The velocity uncertainty interval is composed of N_{bin} bins of size v_{res}. Thus, the normalized velocity accuracy is given by Eq. 3.21, with L and z_{res} replaced by v and v_{res}, with the same Pr(A) and $p_x(X)$ as in the range accuracy derivation.

The normalized range or velocity error is plotted in Figures 3.3a and 3.3b as a function of CNR_0, the no-turbulence infinite-target CNR, for various values of d/ρ_0. It is assumed in these plots that the target diameter is infinite. The bottom curve in Figure 3.3a is for the no-turbulence case. In this case, errors in range or velocity estimation are due to speckle and shot noise. If the strength of $\ell(\cdot)$ is reduced by speckle, then the shape of the peak of $|\ell(\cdot)+\mathbf{n}(\cdot)|^2$, from which the range or velocity estimate is derived, is more strongly affected by the shot noise component, $\mathbf{n}(\cdot)$. This distortion of the shape of the peak can result in an erroneous estimate. If the strength of $\ell(\cdot)$ is sufficiently reduced, then a shot noise peak in an incorrect bin can lead to an anomalous estimate. This behavior is illustrated by the fact that the rms estimation error increases for decreasing CNR_0. In the presence of turbulence, the strength of $\ell(\cdot)$ is reduced by turbulence as well as by speckle. Thus, the rms estimation error has the same qualitative dependence on CNR_0 as it does in the absence of turbulence, but the error is larger for all values of CNR_0 due to this additional source of signal fading. The larger d/ρ_0 is, the stronger is the signal fading due to turbulence, and therefore the larger is the rms estimation error. This behavior is illustrated by the fact that the $d/\rho_0 = 10$ curve lies above the $d/\rho_0 = 5$ curve[1].

All three curves in each plot exhibit the same qualitative behavior. At very high carrier-to-noise ratios, the probability of anomaly is proportional to the reciprocal of the carrier-to-noise ratio [18], so that both terms in the square root on the right hand side of Eq. 3.21 are proportional to the reciprocal of the carrier-to-noise ratio. Thus, in this limiting case the rms estimation error is approximately proportional to the inverse square root of the carrier-to-noise ratio. At very low carrier-to-noise ratios,

---

[1] **If the speckle target is spinning or tilting fast enough that the range or velocity resolution is degraded, then this spinning or tilting would also degrade the range or velocity accuracy. The reason is that $\ell(\cdot)$ is broadened, so that its peak is reduced. This reduction in the peak would degrade the accuracy in a way similar to that in which it is degraded by the turbulence effects described here.**

the anomaly probability approaches a fixed value $(1 - 1/N_{bin})$, and the Eq. 3.19 lower bound for the rms estimation error is now approximately proportional to the reciprocal of the carrier-to-noise ratio. However, the normalized rms estimation error cannot be larger than the number of bins, so all of the curves in Figures 3.3a and 3.3b saturate at 10 and 100, respectively.

The quantitative difference between the curves of Figures 3.3a and 3.3b results from the fact that when the uncertainty interval contains more bins, it is more likely that a shot noise peak in some incorrect bin will lead to an erroneous (anomalous) estimate. Figures 3.3a and 3.3b show that in the presence of turbulence, tens of decibels of additional power may be required in order to achieve a desired range or velocity estimation error.

3.5 Summary

This chapter has shown that the spatial resolution, CNR, and range or velocity estimation accuracy are all significantly degraded by the presence of turbulence when the radar aperture diameter is large compared to ρ_0, although the range and velocity resolution is not significantly affected. The performance degradation may result directly from the turbulence-induced wavefront distortions—as in the case of spatial resolution and CNR—or indirectly through IF signal attenuation and fluctuation—as in the case of range or velocity estimation accuracy. The results obtained here regarding the performance degradation due to turbulence-induced wavefront distortions indicate that it is of interest to find the improvement in performance that could be obtained by wavefront correction. This performance improvement is derived in the next chapter.

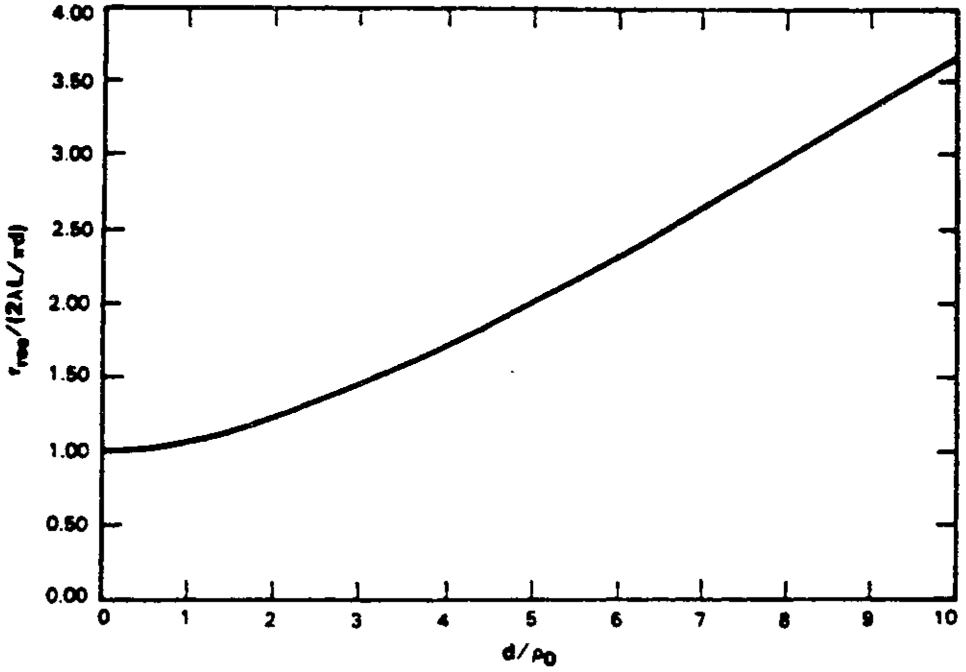

Figure 3.1: Spatial resolution degradation due to turbulence: normalized resolution vs. normalized aperture diameter.

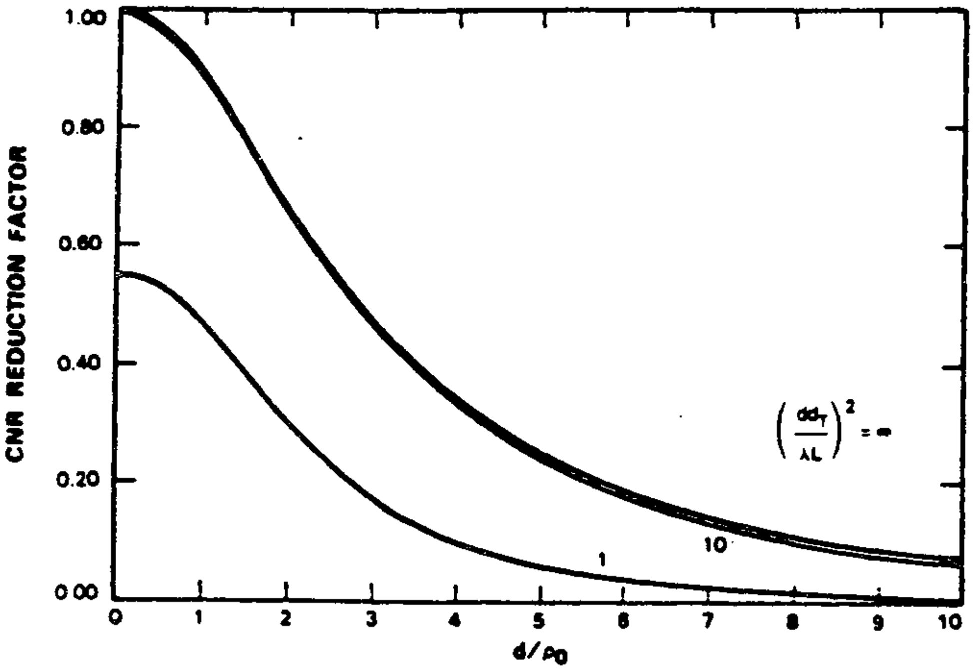

Figure 3.2: CNR reduction due to turbulence: CNR reduction factor vs. normalized aperture diameter for various target sizes.

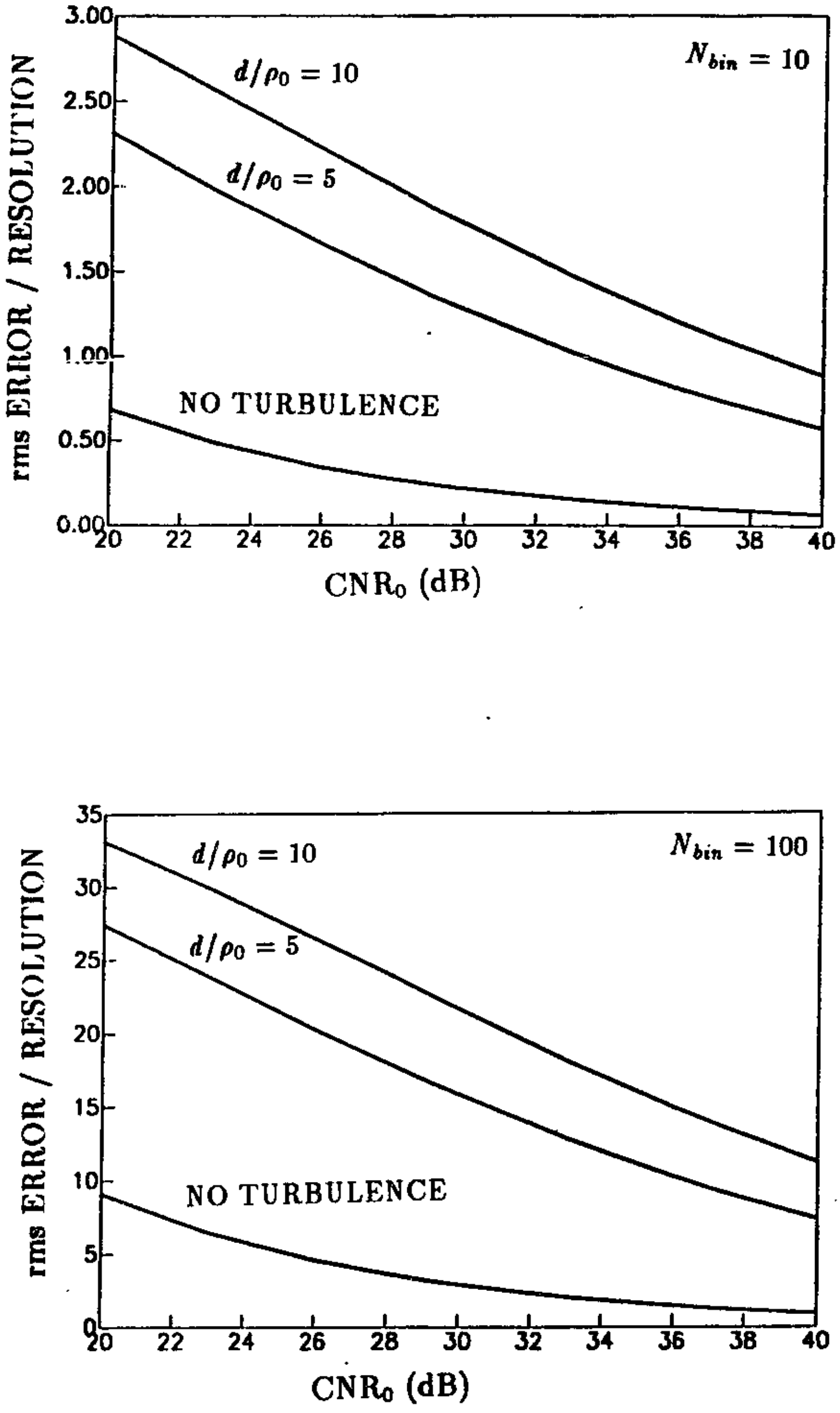

Figure 3.3: Normalized rms range or velocity error vs. carrier-to-noise ratio for various d/ρ_0 values. (a) $N_{bin} = 10$, (b) $N_{bin} = 100$.

Chapter 4

Radar Performance with Perfect Turbulence Phase Correction

The analysis in the previous chapter shows that the spatial resolution, CNR, and range and velocity accuracy are significantly degraded by turbulence-induced wavefront distortions in the illuminator and BPLO beams. If these distortions could somehow be corrected by using adaptive optics, then the radar performance would improve, and the no-turbulence performance advantage of a large aperture radar would be restored. The term adaptive optics refers to a system which compensates in real time for random wavefront fluctuations. Adaptive optics could be used to improve radar performance by continually measuring the appropriate turbulence information and using it to correct the transmitted and/or LO beams. In particular, the illuminator beam would be corrected by predistorting the transmitted beam in such a way as to cancel the turbulence-induced distortions it will incur as it travels to the target. Similarly, the LO beam would be corrected by distorting it in such a way as to cancel the return-path turbulence-induced distortions.

Previous applications of adaptive optics include image compensation and power transfer optimization [45,19]. One context in which image compensation is used is astronomy using a ground-based telescope. The turbulence-induced distortions in the received wavefront reduce the resolving power of the telescope. If the distortions in the received wave are measured and cancelled, then the image formed from the corrected wave will be of better quality than that formed from the uncorrected wave. One context in which power transfer optimization may be used is bidirectional optical communication from a large ($d \gg \rho_0$) transmitter on the ground to a spatially unresolved receiver on a satellite. As the analysis of Section 3.1 shows, the turbulence-induced distortions in the transmitted wave cause the target-plane beam pattern to be broadened, and thus less power is delivered to an unresolved on-axis receiver. Because of atmospheric reciprocity, if the distortions in the wave collected at the ground from the satellite can be measured, then the complex conjugate of these distortions can be applied to the transmitted wave to maximize the mean uplink power transfer [22].

It may not be immediately apparent why this transmitted-wave correction is effective, since the turbulence changes in time. In particular, if the turbulence changes between the time that the received wave has reached the top of the turbulent atmosphere and the time that the corrected transmitted wave reaches the top of the atmosphere, then the received and transmitted waves travel through different turbulence, and the transmitted-wave correction is not completely effective. To see whether this is a significant effect, note that the height of the turbulent part of the atmosphere is about 15 km (the turbulence strength decreases with altitude but it is very small at altitudes higher than this for the $C_n^2(\eta)$ profiles of Figure 2.2), so that the round-trip propagation time through the turbulence is 0.1 msec for vertical propagation. On the other hand, the correlation time of the turbulence distortions at a point in the atmosphere is of the order of ρ_0/v_w, where v_w is the component of the wind velocity perpendicular to the propagation path. For optical to infrared wavelengths, ρ_0 is of the order of 1 cm to 1 meter (at the aperture plane; it would be larger at higher altitudes), and v_w is generally of the order of 1 m/sec, so the turbulence correlation time at a point would be in the range of 10 msec to 1 sec—

much longer than the round-trip propagation time through the turbulence. Thus, the temporal fluctuations of the turbulence should not impair the effectiveness of this type of transmitted-wave correction, since the turbulence can be considered frozen during the round-trip propagation time through it.

There are various technologies for applying the wavefront corrections described above. One way to apply a phase correction to a wavefront is to reflect it off a deformable mirror. A set of actuators controls the shape of the mirror surface, and thereby changes the phase distribution of the reflected wave [19]. Alternately, the complex conjugate of an incident wavefront can be generated by using four-wave mixing techniques [46].

These wavefront correction techniques suffer from one or more of five general types of nonideal behavior [47], namely,

- finite temporal bandwidth,
- finite spatial bandwidth,
- effects of shot noise on the measurement of wavefront distortions,
- anisoplanatic effects in transmitted-wave correction (in which the transmitted wave, and the received wave from which the turbulence-induced distortions are measured, propagate through different turbulence), and
- effects of amplitude fluctuations when only the phase is corrected.

In this chapter, the first four of these effects are neglected, and the radar performance is derived for the case in which the turbulence-induced phase distortions in one or both beams are perfectly cancelled. Therefore, the results derived in this chapter give the ultimate radar performance improvement that can be obtained by using adaptive optics to correct the turbulence-induced phase distortions. The results obtained here indicate that the ideal phase-only correction affords large performance improvements over nonadaptive radar operation in the large aperture ($d \gg \rho_0$) limit, and therefore it is of interest to design a system that will implement such a correction.

Correction of phase only is considered for two reasons. When the turbulence is mainly concentrated near the radar, as it is for a ground-based radar with a vertical propagation path, the turbulence-induced wavefront distortions are mainly phase fluctuations [48]. Furthermore, adaptive optics which correct only the phase may be much easier to build, since amplitude correction may require an additional set of active elements to change the power distribution of the wavefront[1].

In the following analysis, it is assumed that the turbulence-limited spot size in the target pixel plane lies within a single coherence area in that plane. This condition will be called the single coherence area (SCA) approximation. When $d \gg \rho_0$, then the diameter of the uncorrected illuminator or BPLO beam pattern is the turbulence-limited value, of the order of $\lambda L/\rho_0$. Therefore, when

$$\lambda L/\rho_0 < \rho_0' \tag{4.1}$$

the SCA approximation is valid for propagation in both the forward and return paths in the large aperture case ($d \gg \rho_0$). For typical turbulence conditions, (e.g. the $C_n^2(\eta)$ profiles used here), this condition is generally satisfied for vertical paths through the entire atmosphere. It is also satisfied for a sufficiently short horizontal path in the atmosphere.

The transmitted and LO beam patterns with perfect turbulence phase correction are given by

$$\begin{aligned} \xi_T(\vec{\rho};t) &= \xi_0(\vec{\rho})e^{-i\phi_F(\vec{0},\vec{\rho};t)}, & (4.2) \\ \xi_{LO}^*(\vec{\rho};t) &= \xi_0(\vec{\rho})e^{-i\phi_R(\vec{\rho},\vec{0};t)}, & (4.3) \end{aligned}$$

---

[1] This second reason does not apply to the four-wave mixing approach to conjugate-wave generation.

where $\xi_0(\vec{\rho})$ is the uncorrected beam pattern of Eq. 3.1. The turbulence corrections of Eqs. 4.2 and 4.3 compensate for the phase distortion arising from propagation to (for Eq. 4.2) or from (for Eq. 4.3) the point $\vec{\rho}' = \vec{0}$ in the target pixel plane. Because of the SCA approximation, these corrections also compensate for the distortion associated with all points of the illuminator or BPLO spot region for the following reason. Note that $\psi_F(\vec{\rho}', \vec{\rho}; t) \approx \psi_F(\vec{0}, \vec{\rho}; t)$ for $|\vec{\rho}'| < \rho_0'/2$. Therefore, it follows from Eq. 2.3 that when the beam pattern of Eq. 4.2 is transmitted, then turbulence effects in the part of the illuminator beam pattern $\xi_t(\vec{\rho}'; t + \frac{L}{c})$ for which $|\vec{\rho}'| < \rho_0'/2$ are cancelled, neglecting the amplitude fluctuations. If Eq. 4.1 is satisfied, then the *entire* illuminator beam pattern is within a region of diameter ρ_0', and therefore the phase distortions associated with all points of the illuminator spot region are cancelled. A similar argument can be made regarding the BPLO spot region. Actually, Eq. 4.1 is a sufficient but not a necessary condition for cancelling the phase distortions associated with all points of the illuminator or BPLO spot region. The necessary condition is that $\lambda L/d < \rho_0'$ because when the phase correction of Eq. 4.2 or 4.3 is applied, then the diameter of the illuminator or BPLO spot region is actually of the order of $\lambda L/d$ when σ_χ^2 is small, rather than $\lambda L/\rho_0$. However, it will be seen in Chapter 5 that Eq. 4.1 is a necessary condition for *measuring* the turbulence information for wavefront correction. Therefore, Eq. 4.1 will be assumed to be satisfied throughout Chapters 4 and 5, for uniformity.

In the following sections the spatial resolution, CNR, and range and velocity accuracy are derived for cases in which the transmitted and/or LO beams are corrected using the phase corrections of Eqs. 4.2 and 4.3.

4.1 Spatial Resolution with Perfect Phase Correction

In this section the spatial resolution is found for the cases in which one or both beams are corrected. First, the spot sizes on target are found for a corrected beam and for an uncorrected beam. Then an expression is derived for the spatial resolution in terms of the spot sizes of the two target-plane beam patterns, so that the spatial resolution can be found for the cases in which one or both beams are corrected.

When the forward-path turbulence and return-path turbulence are statistically independent, as is assumed here, the spatial resolution is given by the e^{-2} attenuation point of the product $\langle|\xi_t(\vec{\rho}\,';t)|^2\rangle\langle|\xi_{io}^*(\vec{\rho}\,';t)|^2\rangle$. Thus, to find the spatial resolution, we must find the spot sizes of these two beam patterns when the phase of one or both of these beams is corrected.

If the transmitted beam has the correction of Eq. 4.2, then it follows from Eqs. 2.3 and 4.2 and the SCA approximation that

$$\xi_t(\vec{\rho}\,';t) = e^{-\alpha L/2} \int_R d\vec{\rho}\,\xi_0(\vec{\rho})\, e^{\chi_F(\vec{0},\vec{\rho};t)}\, \frac{e^{ikL}}{i\lambda L}\, e^{i\frac{k}{2L}\rho'^2}\, e^{-i\frac{k}{L}\vec{\rho}\,'\cdot\vec{\rho}} \tag{4.4}$$

is the illuminator beam pattern. In order to find $\langle|\xi_t(\vec{\rho}\,';t)|^2\rangle$ when the transmitted phase is corrected, we must use

$$\left\langle e^{\chi_F(\vec{0},\vec{\rho}_1;t)} e^{\chi_F(\vec{0},\vec{\rho}_2;t)} \right\rangle = e^{-\frac{1}{2}\mathcal{D}_{\chi\chi}(\vec{0},\vec{\rho}_1-\vec{\rho}_2)}, \tag{4.5}$$

where $\mathcal{D}_{\chi\chi}(\vec{\rho}\,',\vec{\rho})$ is the structure function of the log-amplitude fluctuations, defined in Eq. 2.6. The mean squared illuminator beam pattern can be found from Eqs. 4.4 and 4.5 to be

$$\langle|\xi_t(\vec{\rho}\,';t)|^2\rangle = e^{-\alpha L}\frac{1}{(\lambda L)^2} \int d\vec{v}\, e^{-4v^2/d^2} e^{-\frac{1}{2}\mathcal{D}_{\chi\chi}(\vec{0},\vec{v})} e^{-i\frac{k}{L}\vec{\rho}\,'\cdot\vec{v}}. \tag{4.6}$$

The expression for $\mathcal{D}_{\chi\chi}(\vec{0},\vec{\rho})$ is complicated (see Eq. 2.7), and integrals involving the exponential of this expression are very difficult to evaluate. However, using the fact that

$$\langle|\mathbf{x}|^2\rangle \geq |\langle\mathbf{x}\rangle|^2 \tag{4.7}$$

for a complex random variable $\mathbf{x}$, we can use Eq. 4.4 to obtain the following lower bound for $\langle|\xi_t(\vec{\rho}\,';t)|^2\rangle$ when the transmitted phase is corrected:

$$\langle|\xi_t(\vec{\rho}\,';t)|^2\rangle \geq e^{-\sigma_\chi^2}\, e^{-\alpha L}\, \frac{\pi}{4}\left(\frac{d}{\lambda L}\right)^2 e^{-(\frac{kd}{4L})^2 \rho'^2}, \tag{4.8}$$

where we have used the fact that χ is Gaussian to find $\langle e^\chi\rangle$. Furthermore, $\langle|\xi_t(\vec{\rho}\,';t)|^2\rangle$ cannot be appreciably larger than the lower bound of Eq. 4.8 over a large region because the total area under $\langle|\xi_t(\vec{\rho}\,';t)|^2\rangle$ is $e^{\sigma_\chi^2}$ times times the total area under this lower bound formula. Since $e^{\sigma_\chi^2}$ is close to 1 for moderate turbulence conditions, the area under $\langle|\xi_t(\vec{\rho}\,';t)|^2\rangle$ and the area under its lower bound cannot be very different, so that $\langle|\xi_t(\vec{\rho}\,';t)|^2\rangle$ cannot deviate greatly from its lower bound, except in the form of narrow spikes. It can be argued—see below—that such spikes do not exist, so we shall say that $\langle|\xi_t(\vec{\rho}\,';t)|^2\rangle$ is close to its lower bound.

The argument that such spikes do not exist is based on consideration of horizontal-path propagation. The structure function $\mathcal{D}_{\chi\chi}(\vec{0},\vec{v})$ of the log-amplitude fluctuations has been calculated for horizontal-path propagation [30]. It is monotonically increasing with $|\vec{v}|$ for $|\vec{v}|$ less than $\sqrt{\lambda L}$, beyond which it is nearly constant. Therefore, consideration of Eq. 4.6 shows that $\langle|\xi_t(\vec{\rho}\,';t)|^2\rangle$ will be a smooth function with few oscillations. For vertical propagation through the entire atmosphere, the $C_n^2(\eta)$ profile varies with altitude, and thus $\mathcal{D}_{\chi\chi}(\vec{0},\vec{v})$ is more difficult to evaluate. However, the $C_n^2(\eta)$ profiles used here vary monotonically with altitude, so it appears from Eq. 2.7 that even for vertical propagation $\mathcal{D}_{\chi\chi}(\vec{0},\vec{v})$ will be a smooth function with few oscillations. Furthermore, it can be argued that $\mathcal{D}_{\chi\chi}(\vec{0},\vec{v})$ will have the same qualitative dependence on $|\vec{v}|$ as it does for a horizontal path, but with L replaced by H, an effective scale height of the turbulent propagation path. Thus, consideration of Eq. 4.6 shows that $\langle|\xi_t(\vec{\rho}\,';t)|^2\rangle$ would also be a smooth function, without spikes.

The width of this beam pattern, on which the spatial resolution depends, is estimated to be the e^{-1} attenuation point of the widest Gaussian curve which satisfies the lower bound of Eq. 4.8 and whose total area is $e^{-\alpha L}$. This width is found to be

$$w_t = e^{\sigma_\chi^2/2} \cdot \frac{2\lambda L}{\pi d}, \tag{4.9}$$

which is close to the diffraction limited value, $2\lambda L/(\pi d)$.

The width of the BPLO beam pattern in the case of LO correction can be found by using a similar procedure. If the LO beam has the correction of Eq. 4.3, the it follows from Eqs. 2.21 and 4.3 and the SCA approximation that

$$\xi_{lo}^*(\vec{\rho}\,';t) = e^{-\alpha L/2} \int_R d\vec{\rho}\, \xi_0(\vec{\rho})\, e^{\chi_R(\vec{\rho},\vec{0};t)} \frac{e^{ikL}}{i\lambda L}\, e^{i\frac{k}{2L}\rho'^2}\, e^{-i\frac{k}{L}\vec{\rho}\,'\cdot\vec{\rho}} \tag{4.10}$$

is the BPLO beam pattern. The mean BPLO intensity $\langle|\xi_{lo}^*(\vec{\rho}\,';t)|^2\rangle$ has the same lower bound as that of Eq. 4.8, and therefore the width of the BPLO beam pattern, as defined above, is given by

$$w_l = e^{\sigma_\chi^2/2} \cdot \frac{2\lambda L}{\pi d}, \tag{4.11}$$

the same as the width of the illuminator beam pattern.

The spatial resolution can now be found by noting that

$$\langle|\xi_t(\vec{\rho}\,';t)|^2\rangle\langle|\xi_{lo}^*(\vec{\rho}\,';t)|^2\rangle \;\propto\; e^{-\rho'^2/w_t^2} e^{-\rho'^2/w_l^2}, \tag{4.12}$$

and the e^{-2} attenuation point of this expression is

$$r_{res} = \sqrt{2} w_t w_l / \sqrt{w_t^2 + w_l^2}. \tag{4.13}$$

When the phases of both the transmitted and LO beams are corrected, then w_t and w_l are given by Eqs. 4.9 and 4.11, so that the spatial resolution is

$$r_{res} = e^{\sigma_\chi^2/2} \cdot \frac{2\lambda L}{\pi d}, \tag{4.14}$$

with both beams corrected. If the phase of either the transmitted or the LO beam is not corrected, then the e^{-1} attenuation points can be found from Eq. 3.3 to be

$$w_t,\ w_l = \sqrt{1 + \frac{d^2}{8\rho_0^2}} \cdot \frac{2\lambda L}{\pi d}. \tag{4.15}$$

Therefore, if one beam is corrected and one is not, the spatial resolution is

$$r_{res} = \frac{\sqrt{2} e^{\sigma_\chi^2/2} \sqrt{1 + \frac{d^2}{8\rho_0^2}}}{\sqrt{e^{\sigma_\chi^2} + 1 + \frac{d^2}{8\rho_0^2}}} \cdot \frac{2\lambda L}{\pi d} \tag{4.16}$$

with one beam corrected, regardless of which beam is corrected (since both beam have the same uncorrected beam pattern $\xi_0(\vec{\rho})$). In the limiting case of a large aperture, i.e. $d^2/(8\rho_0^2)$ large compared to 1 and to $e^{\sigma_\chi^2}$, the spatial resolution approaches

$$r_{res} \overset{\text{large d}}{\approx} \sqrt{2} e^{\sigma_\chi^2/2} \cdot \frac{2\lambda L}{\pi d} \tag{4.17}$$

with one beam corrected, close to the value for both beams corrected. Finally, when neither beam is corrected, the spatial resolution in given by Eq. 3.4. The spatial resolution formulas given here are summarized in Table 4.1.

The physical significance of these spatial resolution results is illustrated in Figures 4.1a-c. Recall that we are assuming that the radar is monostatic, so that a single aperture is used for both transmitting and receiving. However, in these figures, the apertures used for transmitting and for receiving are drawn separately to better illustrate the effects of wavefront correction. This illustration format suggests that the forward-path turbulence and return-path turbulence are different; in fact they are different due to the long round-trip exoatmospheric propagation delay. Figure 4.1a illustrates the case in which both beams are phase-corrected. Each beam pattern is predistorted in such a way as to cancel the turbulence-induced distortions incurred in propagation to the target. Therefore, the target-plane beam patterns are close to diffraction-limited, so that the spatial resolution is close to its no-turbulence value. The dashed contour on the target shows the spot size that

	r_{res}
neither beam corrected	$\frac{2\lambda L}{\pi d}\sqrt{1+\frac{d^2}{8\rho_0^2}}$
one beam corrected	$e^{\sigma_\chi^2/2}\cdot\frac{2\lambda L}{\pi d}\frac{\sqrt{2}\sqrt{1+\frac{d^2}{8\rho_0^2}}}{\sqrt{e^{\sigma_\chi^2/2}+1+\frac{d^2}{8\rho_0^2}}}$
both beams corrected	$e^{\sigma_\chi^2/2}\cdot\frac{2\lambda L}{\pi d}$
no-turbulence value	$\frac{2\lambda L}{\pi d}$

	r_{res}: large aperture limit
neither beam corrected	$\frac{1}{\sqrt{8}}\frac{2\lambda L}{\pi\rho_0}$
one beam corrected	$e^{\sigma_\chi^2/2}\cdot\sqrt{2}\,\frac{2\lambda L}{\pi d}$
both beams corrected	$e^{\sigma_\chi^2/2}\cdot\frac{2\lambda L}{\pi d}$
no-turbulence value	$\frac{2\lambda L}{\pi d}$

Table 4.1: Spatial Resolution with Perfect Turbulence Phase Correction

would result from an uncorrected transmitted or LO beam, for comparison with Figures 4.1b and 4.1c. Figure 4.1b illustrates the case in which only one beam is phase-corrected. Then the target-plane beam pattern resulting from that correction is close to diffraction-limited, while the other target-plane beam pattern is turbulence-limited (for $d \gg \rho_0$). The spatial resolution depends on the size of the target region illuminated by the product of *both* beams, which in this case is the region illuminated by the corrected beam. Therefore, when only one beam is corrected, the spatial resolution is still close to diffraction limited, though not quite as good as it is when both beams are corrected. Figure 4.1c illustrates the case in which neither beam is phase-corrected. In this case both target-plane beam patterns are turbulence-limited (for $d \gg \rho_0$), and therefore the spatial resolution is turbulence-limited.

4.2 CNR with Perfect Phase Correction

As mentioned in Section 3.2, the CNR is given by

$$\mathrm{CNR} = \frac{\eta P_T \epsilon_{opt}}{h\nu_0 B}\frac{\lambda^2 \rho}{\pi}\int d\vec{\rho}\,'\langle|\xi_t(\vec{\rho}\,';t)|^2\rangle\langle|\xi_{lo}^*(\vec{\rho}\,';t)|^2\rangle e^{-4\rho'^2/d_T^2}, \tag{4.18}$$

when the two target-plane beam patterns are statistically independent. The mean squared beam patterns derived in Sections 4.1 and 3.1 can be used to evaluate the CNR for the cases in which one or both beams are corrected.

4.2.1 CNR with one beam corrected

First the CNR will be found for the case in which only one beam is corrected. The result is the same whether the transmitted or LO beam is corrected, because the uncorrected beam pattern is the same for both beams and because the turbulence in the forward path and the turbulence in the return path have the same statistics. Therefore the case of transmitted beam correction is considered.

A lower bound can be obtained for the CNR expression of Eq. 4.18 by using the lower bound formula of Eq. 4.8 for the mean squared illuminator beam pattern with transmitted beam correction, and by using Eq. 3.3 for the mean squared BPLO beam pattern with no LO correction. The result is

$$\mathrm{CNR} \geq \mathrm{CNR}_0\, e^{-\sigma_\chi^2} \cdot \frac{1}{1+\frac{d^2}{16\rho_0^2}+8\left(\frac{\lambda L}{\pi d d_T}\right)^2\left(1+\frac{d^2}{8\rho_0^2}\right)}. \tag{4.19}$$

An upper bound can be obtained for the CNR with only the transmitted beam corrected by first substituting the exact expressions for the mean squared target-plane beam patterns into Eq. 4.18. Substituting Eq. 4.6, and Eq. 3.3 for the mean squared BPLO beam pattern, into Eq. 4.18 gives

$$\mathrm{CNR} = \mathrm{CNR}_0 \cdot \frac{8}{\pi(1+16A^2B)}\frac{1}{d^2}\int d\vec{v}\, e^{-4v^2/d^2} e^{-\frac{1}{2}\mathcal{D}_{\chi\chi}(\vec{0},\vec{v})} e^{-\frac{4B}{1+16A^2B}v^2/d^2} \tag{4.20}$$

where $A \equiv \lambda L/(\pi d d_T)$ and $B \equiv 1 + d^2/(8\rho_0^2)$ have been used for brevity. It follows from Eq. 2.7 that $e^{-\frac{1}{2}\mathcal{D}_{\chi\chi}(\vec{0},\vec{v})} \leq 1$, and therefore, because the other terms of the integrand of Eq. 4.20 are greater than or equal to 0, an upper bound can be obtained for Eq. 4.20 by setting this former term *equal* to 1. The result is

$$\mathrm{CNR} \leq \mathrm{CNR}_0 \cdot \frac{1}{1+\frac{d^2}{16\rho_0^2}+8\left(\frac{\lambda L}{\pi d d_T}\right)^2\left(1+\frac{d^2}{8\rho_0^2}\right)}. \tag{4.21}$$

This upper bound is less than the no-turbulence finite-target result (obtained by letting $\rho_0 \to \infty$ in Eq. 3.5), so that the CNR with perfect phase correction in one beam is less than the no-turbulence value.

The effect on the CNR of correction of only one beam can easily be seen by comparing the turbulence-limited CNR's (obtained by letting $d \to \infty$) for the cases of single beam correction and no correction. The turbulence-limited CNR for the case of no correction is, using Eq. 3.5,

$$\mathrm{CNR} \overset{d\to\infty}{=} \mathrm{CNR}_0 \cdot \frac{8\rho_0^2}{d^2} \cdot \frac{1}{1+\left(\frac{\lambda L}{\pi\rho_0 d_T}\right)^2}. \tag{4.22}$$

An approximation for the CNR in the case of single beam correction can be obtained by comparing the lower and upper bound formulas, Eqs. 4.19 and 4.21. Since σ_χ^2 is very small for vertical propagation paths, these two bounds are nearly equal, so the CNR will be taken here to be approximately equal to the upper bound formula. The turbulence-limited result for this formula is

$$\mathrm{CNR} \overset{d\to\infty}{\approx} \mathrm{CNR}_0 \cdot \frac{16\rho_0^2}{d^2}. \tag{4.23}$$

Eq. 4.23 shows that if the aperture is sufficiently large, the CNR does not depend on the target size. This effect is illustrated in Figure 4.1b. The part of the target which contributes to the CNR is the shaded region—the region of overlap between the two target-plane beam patterns. If the aperture is sufficiently large, then the illuminator beam pattern will be smaller than the target, so that the overlap region will be smaller than the target, and therefore the target size will not affect the CNR. The second effect of correcting a single beam is that if the target is much larger than the turbulence-limited spot size (on the order of $\lambda L/\rho_0$), then the turbulence-limited CNR is increased by a factor of 2 due to the increased spatial matching between the two beams. However, the CNR still saturates for large aperture sizes, because only the energy in the BPLO beam pattern which falls within of the overlap region contributes to the target return. Because the spot size of the BPLO beam pattern saturates for large aperture sizes, the amount of its energy which falls within the overlap region (i.e. within a diffraction-limited spot region) also saturates for large aperture sizes, and therefore the CNR saturates for large aperture sizes when only one beam is corrected.

4.2.2 CNR with both beams corrected

Now the CNR will be found for the case in which both beams are corrected. In this case, both target-plane mean squared beam patterns have the lower bound of

Eq. 4.8. Substituting Eq. 4.8 into Eq. 4.18 for both mean squared beam patterns gives the following lower bound for the CNR:

$$\mathrm{CNR} \geq \mathrm{CNR}_0 \cdot e^{-2\sigma_\chi^2} \cdot \frac{1}{1+8\left(\frac{\lambda L}{\pi d d_T}\right)^2}. \tag{4.24}$$

An upper bound for the CNR can be found by first substituting Eq. 4.6 into Eq. 4.18 for both mean squared beam patterns. After carrying out the $\vec{\rho}\,'$ integral, the result is

$$\begin{aligned}\mathrm{CNR} \;=\; & \mathrm{CNR}_0 \cdot 2\left(\frac{d_T}{\lambda L d}\right)^2 \int d\vec{v}_1 \int d\vec{v}_2\, e^{-4(v_1^2+v_2^2)/d^2} \cdot \\ & \exp\left(-\frac{1}{2}[\mathcal{D}_{\chi\chi}(\vec{0},\vec{v}_1)+\mathcal{D}_{\chi\chi}(\vec{0},\vec{v}_2)]\right) \cdot \\ & \exp\left(-\left(\frac{kd_T}{4L}\right)^2 |\vec{v}_1+\vec{v}_2|^2\right).\end{aligned} \tag{4.25}$$

The upper bound can be found from Eq. 4.25 by setting $e^{-\frac{1}{2}\mathcal{D}_{\chi\chi}(\vec{0},\vec{v})} = 1$, as was done for the case of single beam correction, because $e^{-\frac{1}{2}\mathcal{D}_{\chi\chi}(\vec{0},\vec{v})} \leq 1$ and because the other terms of the integrand of Eq. 4.25 are greater than or equal to 0. The result is

$$\mathrm{CNR} \leq \mathrm{CNR}_0 \cdot \frac{1}{1+8\left(\frac{\lambda L}{\pi d d_T}\right)^2}. \tag{4.26}$$

Comparing the lower and upper bound formulas, Eqs. 4.24 and 4.26, shows that when σ_χ^2 is small, the CNR is approximately equal to the no-turbulence formula of Eq. 4.26. In this case the two beams have good spatial matching, as they would in the absence of turbulence.

The analysis in this section shows that correction of one of the beams can remove the target size dependence of the CNR for sufficiently large aperture sizes, but the CNR still saturates at a turbulence-limited value which is only slightly larger than the turbulence-limited value for the case of no correction. The reason is that the spot size of the uncorrected beam saturates for large aperture sizes, so that the energy in the region of overlap between the two target-plane beam patterns also saturates

	CNR/CNR$_0$
neither beam corrected	$\left[1+\frac{d^2}{8\rho_0^2}\right]^{-1}\left[1+8\left(\frac{\lambda L}{\pi d d_T}\right)^2\left(1+\frac{d^2}{8\rho_0^2}\right)\right]^{-1}$
one beam corrected: lower bound	$e^{-\sigma_\chi^2}\left[1+\frac{d^2}{16\rho_0^2}+8\left(\frac{\lambda L}{\pi d d_T}\right)^2\left(1+\frac{d^2}{8\rho_0^2}\right)\right]^{-1}$
upper bound	$\left[1+\frac{d^2}{16\rho_0^2}+8\left(\frac{\lambda L}{\pi d d_T}\right)^2\left(1+\frac{d^2}{8\rho_0^2}\right)\right]^{-1}$
both beams corrected: lower bound	$e^{-2\sigma_\chi^2}\left[1+8\left(\frac{\lambda L}{\pi d d_T}\right)^2\right]^{-1}$
upper bound	$\left[1+8\left(\frac{\lambda L}{\pi d d_T}\right)^2\right]^{-1}$
no-turbulence value	$\left[1+8\left(\frac{\lambda L}{\pi d d_T}\right)^2\right]^{-1}$

	CNR/CNR$_0$: large aperture limit
neither beam corrected	$\frac{8\rho_0^2}{d^2}\left[1+\left(\frac{\lambda L}{\pi \rho_0 d_T}\right)^2\right]^{-1}$
one beam corrected	$\approx \frac{16\rho_0^2}{d^2}$
both beams corrected	≈ 1
no-turbulence value	1

Table 4.2: CNR with Perfect Turbulence Phase Correction

for large aperture sizes. Both beams must be corrected in order to approach the no-turbulence CNR. The CNR formulas given here are summarized in Table 4.2.

4.3 Range and Velocity Accuracy with Perfect Phase Correction

In Section 3.4, the range and velocity accuracy for the case of no correction was obtained from the corresponding no-turbulence results by using the substitution CNR → $\text{CNR}_T \cdot x$, where the random variable x represents the turbulence-induced fluctuations. The range and velocity accuracy for the cases in which the phase of one or both beams is corrected can be obtained from the no-turbulence results in a similar way. The only difference is that now x has a different probability distribution, because the phase correction causes the resulting target-plane beam patterns to have different statistics. Thus, the normalized range or velocity accuracy is still given by the right hand side of Eq. 3.21, but now the local accuracy is averaged over a different $p_x(X)$ distribution, and Pr(A) is found from the no-turbulence formula by averaging over a different $p_x(X)$ distribution. Therefore, it is sufficient to find $p_x(X)$ for the cases in which either one or both beams is corrected. In the following analysis it is again assumed that x is approximately given by Eq. 3.24.

4.3.1 Accuracy with one beam corrected

First $p_x(X)$ will be found for the case in which only one beam (e.g. the transmitted beam) is corrected. The two factors in Eq. 3.24 are statistically independent because the turbulence fluctuations in the forward and return paths are statistically independent; therefore $p_x(X)$ can be found from the probability distributions of each factor. Since the LO beam is uncorrected, $|\xi_{lo}^*(\vec{0})|^2/\langle|\xi_{lo}^*(\vec{0})|^2\rangle$ is an exponential random variable, as explained in Section 3.4.

Equation 4.4 implies that

$$|\xi_t(\vec{0})|^2 = e^{-\alpha L}\frac{1}{(\lambda L)^2}\left|\int_R d\vec{\rho}\,\xi_0(\vec{\rho})\,e^{\chi_F(\vec{0},\vec{\rho})}\right|^2, \tag{4.27}$$

where the time dependence of ξ_t and of χ_F is omitted for brevity. Assuming that the aperture is large compared to the coherence length of $e^{\chi_F(\vec{0},\vec{\rho})}$, the integral in Eq. 4.27 is a sum of statistically independent real lognormal random variables because $\xi_0(\vec{\rho})$ is real and $\chi_F(\vec{0},\vec{\rho})$ is Gaussian. The sum of a large number of statistically independent real lognormal random variables is approximately lognormal [49], and the square of a lognormal random variable is also lognormal, so therefore $|\xi_t(\vec{0})|^2/\langle|\xi_t(\vec{0})|^2\rangle$ is approximately lognormal. Let

$$\frac{|\xi_t(\vec{0})|^2}{\langle|\xi_t(\vec{0})|^2\rangle} \equiv w \equiv e^{2u}, \tag{4.28}$$

where u is a Gaussian random variable. The probability distribution of w is given by

$$p_w(W) = \frac{1}{\sqrt{8\pi\sigma_u^2 W}} e^{-(\ln W - 2\langle u\rangle)^2/(8\sigma_u^2)} \mathsf{u}(W), \tag{4.29}$$

where $\langle u\rangle$ and σ_u^2 are the mean and variance of u, and $\mathsf{u}(\cdot)$ is the unit step function. Since w has mean 1 by construction, it follows that

$$\langle u\rangle = -\sigma_u^2. \tag{4.30}$$

The variance of u can be found by taking the variance of Eq. 4.28, namely

$$\operatorname{var}\left(\frac{|\xi_t(\vec{0})|^2}{\langle|\xi_t(\vec{0})|^2\rangle}\right) = e^{4\sigma_u^2} - 1. \tag{4.31}$$

The first and second moments of $|\xi_t(\vec{0})|^2$ can be found from Eq. 4.27 by using the fact that the mean of $\chi_F(\vec{0}, \vec{\rho})$ is $-\sigma_\chi^2$, as mentioned in Section 2.2. Using these moments in Eq. 4.31 gives

$$\begin{aligned}
e^{4\sigma_u^2} = \ & [\int d\vec{\rho}_1 \int d\vec{\rho}_2 \int d\vec{\rho}_3 \int d\vec{\rho}_4\, \xi_0(\vec{\rho}_1)\, \xi_0(\vec{\rho}_2)\, \xi_0(\vec{\rho}_3)\, \xi_0(\vec{\rho}_4) \\
& \exp(C_{\chi\chi}(\vec{0}, \vec{\rho}_1 - \vec{\rho}_2) + C_{\chi\chi}(\vec{0}, \vec{\rho}_1 - \vec{\rho}_3) + C_{\chi\chi}(\vec{0}, \vec{\rho}_1 - \vec{\rho}_4) \\
& + C_{\chi\chi}(\vec{0}, \vec{\rho}_2 - \vec{\rho}_3) + C_{\chi\chi}(\vec{0}, \vec{\rho}_2 - \vec{\rho}_4) + C_{\chi\chi}(\vec{0}, \vec{\rho}_3 - \vec{\rho}_4))]/ \\
& [\int d\vec{\rho}_1 \int d\vec{\rho}_2 \int d\vec{\rho}_3 \int d\vec{\rho}_4\, \xi_0(\vec{\rho}_1)\, \xi_0(\vec{\rho}_2)\, \xi_0(\vec{\rho}_3)\, \xi_0(\vec{\rho}_4) \\
& \exp(C_{\chi\chi}(\vec{0}, \vec{\rho}_1 - \vec{\rho}_2) + C_{\chi\chi}(\vec{0}, \vec{\rho}_3 - \vec{\rho}_4))],
\end{aligned} \tag{4.32}$$

where $C_{\chi\chi}(\vec{\rho}\,', \vec{\rho})$ is the covariance of the log-amplitude fluctuations. Eq. 4.32 is difficult to evaluate, but because $C_{\chi\chi}(\vec{\rho}\,', \vec{\rho}) \leq \sigma_\chi^2$, and $\xi_0(\vec{\rho}) \geq 0$, the right hand side of Eq. 4.32 is less than or equal to $e^{4\sigma_\chi^2}$, and therefore

$$\sigma_u^2 \leq \sigma_\chi^2. \tag{4.33}$$

Because of aperture averaging of the amplitude fluctuations in Eq. 4.27, we can expect that the inequality 4.33 will be strict [23].

It follows from Eqs. 4.29 and 4.30 that the probability distribution of w is given by

$$p_w(W) = \frac{1}{\sqrt{8\pi\sigma_u^2 W}} e^{-(\ln W + 2\sigma_u^2)^2/(8\sigma_u^2)} \mathrm{u}(W), \tag{4.34}$$

where σ_u^2 is given by Eq. 4.32 and is bounded by Eq. 4.33. Thus, $x = wy$ where $p_w(W)$ is given by Eq. 4.34 and $p_y(Y) = e^{-Y}\mathrm{u}(Y)$. Therefore, the normalized range or velocity accuracy is given by Eq. 3.21 with

$$\begin{aligned} \left\langle \frac{(4\mathrm{CNR}_T x)^2}{\mathrm{CNR}_T x + 1} \right\rangle &= \int_0^\infty dW \int_0^\infty dY \frac{(4\mathrm{CNR}_T WY)^2}{\mathrm{CNR}_T WY + 1} \cdot \\ &\quad \frac{1}{\sqrt{8\pi\sigma_u^2 W}} e^{-(\ln W + 2\sigma_u^2)^2/(8\sigma_u^2)}\, e^{-Y}, \end{aligned} \tag{4.35}$$

and, from Eq. 3.14[2],

$$\begin{aligned} \Pr(A) &= 1 - \int_0^\infty dW \int_0^\infty dY \int_0^\infty dv \frac{1}{1 + \mathrm{CNR}_T WY} e^{-v/(1+\mathrm{CNR}_T WY)} \cdot \\ &\quad (1 - e^{-v})^{N_{bin}-1} \frac{1}{\sqrt{8\pi\sigma_u^2 W}} e^{-(\ln W + 2\sigma_u^2)^2/(8\sigma_u^2)}\, e^{-Y}. \end{aligned} \tag{4.36}$$

4.3.2 Accuracy with both beams corrected

The probability distribution of x for the case in which both beams are corrected follows directly from the results given above. In particular, since both beams are corrected, it follows that $|\xi_t(\vec{0})|^2/\langle|\xi_t(\vec{0})|^2\rangle$ and $|\xi_{i_o}^*(\vec{0})|^2/\langle|\xi_{i_o}^*(\vec{0})|^2\rangle$ are statistically independent, identically distributed lognormal random variables with the probability distribution of Eq. 4.34. Therefore x is also lognormal, with

$$p_x(X) = \frac{1}{\sqrt{16\pi\sigma_u^2 X}} e^{-(\ln X + 4\sigma_u^2)^2/(16\sigma_u^2)} \mathrm{u}(X). \tag{4.37}$$

Thus, the normalized range and velocity accuracy is given by Eq. 3.21 with

$$\left\langle \frac{(4\mathrm{CNR}_T x)^2}{\mathrm{CNR}_T x + 1} \right\rangle =$$

---

[2] The v integral in the following equation can be simplified by noting that $\int_0^\infty dv \frac{1}{A} e^{-v/A}(1 - e^{-v})^M = \prod_{j=1}^M \frac{jA}{jA+1}$.

$$\int_0^\infty dX\,\frac{(4\mathrm{CNR}_T X)^2}{\mathrm{CNR}_T X+1}\cdot\frac{1}{\sqrt{16\pi\sigma_u^2 X}}\,e^{-(\ln X+4\sigma_u^2)^2/(16\sigma_u^2)}, \tag{4.38}$$

and, from Eq. 3.14[2],

$$\begin{aligned}\Pr(A) \;=\; & 1-\int_0^\infty dX\int_0^\infty dv\,\frac{1}{1+\mathrm{CNR}_T X}\,e^{-v/(1+\mathrm{CNR}_T X)}\,. \\ & (1-e^{-v})^{N_{bin}-1}\frac{1}{\sqrt{16\pi\sigma_u^2 X}}\,e^{-(\ln X+4\sigma_u^2)^2/(16\sigma_u^2)}.\end{aligned} \tag{4.39}$$

The normalized range or velocity accuracy is plotted in Figures 4.2a-d and 4.3a-d for various values of N_{bin} and σ_u^2, for the cases in which one or both beams are corrected. In plotting these curves it has been assumed that the target size is infinite. Figures 4.2a-d show the results for the case in which one beam is corrected. Comparison of Figures 4.2a and 4.2b, as well as comparison of Figures 4.2c and 4.2d, shows that the accuracy for $N_{bin} = 100$ is slightly more than a factor of ten worse than the accuracy for $N_{bin} = 10$. As explained in Section 3.4, this difference is due to the fact that when the uncertainty interval contains more bins, it is more likely that a shot noise peak in some incorrect bin will lead to an erroneous estimate.

Comparison of Figures 4.2a and 4.2c, as well as comparison of Figures 4.2b and 4.2d, shows that the accuracy changes negligibly when σ_u^2 is decreased from 10^{-3} to 10^{-4}. The reason is that for such low values of σ_u^2, the effect of the log-amplitude fluctuations on the range and velocity accuracy is negligible. The reason these values of σ_u^2 are used for illustration is that for wavelengths of interest, σ_χ^2 is in or near the range of 10^{-3} to 10^{-4} for vertical propagation paths through the atmosphere. For example, it follows from Eq. 2.5 that for a wavelength of 10.6 μm, the values of σ_χ^2 for daytime and nighttime turbulence conditions are 3.6×10^{-4} and 1.9×10^{-4} respectively, and for a wavelength of 5 μm, the corresponding values are 8.8×10^{-4} and 4.5×10^{-4}. For shorter wavelengths σ_χ^2 would be larger, but Eq. 4.33 shows that $\sigma_u^2 \le \sigma_\chi^2$, so σ_u^2 may still fall into this range.

The effect of correcting one beam on the range or velocity accuracy can be seen by comparing Figures 4.2a and 4.2c with Figure 3.3a, for $N_{bin} = 10$, or by comparing Figures 4.2b and 4.2d with Figure 3.3b, for $N_{bin} = 100$. These comparisons show that correction of a single beam gives a moderate improvement in the accuracy. For example, when $N_{bin} = 10$, for a normalized accuracy of 1.0 when $d/\rho_0 = 5$, correcting one beam gives about a 7 decibel CNR_0 improvement. However, a 16 decibel improvement would be needed to obtain the no-turbulence performance. For a normalized accuracy of 2.0 when $d/\rho_0 = 10$, correcting one beam gives about a 6 decibel CNR_0 improvement. However, an 18 decibel improvement would be needed to obtain the no-turbulence performance.

Correction of a single beam improves the accuracy by increasing the CNR, as shown by Eqs. 4.19 and 4.21, and by reducing the fluctuations in the target return intensity. The increase in CNR obtained by correcting a single beam is slight—comparison of Eq. 4.22 for $d_T \to \infty$ and Eq. 4.33 shows that this improvement is 3 decibels. Furthermore, when only one beam is corrected, the fluctuations in the uncorrected beam still cause significant fluctuations in the target return intensity. Thus, it is not surprising that the improvement in accuracy is relatively small when only one beam is corrected. Note that the range and velocity accuracy saturate for large aperture sizes when only one beam is corrected, because the d-dependence of the accuracy is in CNR_T (see Eqs. 4.39 and 4.36), which saturates at a turbulence-limited value when only one beam is corrected.

The effect of correcting both beams on the range or velocity accuracy is shown in Figures 4.3a-d, for the same values of N_{bin} and σ_u^2 as those of Figures 4.2a-d. All of these curves show that correcting both beams very nearly restores the accuracy to its no-turbulence level for these values of σ_u^2. When both beams are corrected, the CNR is very close to its no-turbulence value, as shown by Eqs. 4.24 and 4.26. Furthermore, since the wavefront correction is good enough to attain the no-turbulence CNR, it is also good enough to almost entirely eliminate the beam pattern fluctuations which lead to fluctuations in the target return intensity. For these reasons, correction of both beams restores the accuracy to very close to its no-turbulence level.

4.4 Summary

This chapter presents the spatial resolution, CNR, and range and velocity accuracy for the cases in which the phase of one or both beams is perfectly corrected for the turbulence-induced distortions. When only one beam is corrected, the region of overlap between the two target-plane beam patterns is the region illuminated by the corrected beam pattern, whose spot size is close to the no-turbulence value. The energy in the target return is the energy illuminating this overlap region (see Eq. 3.2). The size of this region is close to the no-turbulence value, and therefore the spatial resolution is close to the no-turbulence value when only one beam is corrected. However, none of the energy in the uncorrected target-plane beam pattern which falls outside of this overlap region contributes to the target return, and therefore the CNR saturates at a turbulence-limited value when only one beam is corrected. Because of this CNR saturation, and because of the fluctuations in the uncorrected beam, the range and velocity accuracy also saturate at a turbulence-limited value when only one beam is corrected.

When the phases of both beam are corrected, the spatial resolution, CNR, and range and velocity accuracy are all very close to their no-turbulence levels. In this case, all of the turbulence-induced phase distortions are corrected, and the amplitude distortions have a very small variance for vertical propagation paths through the atmosphere. Since turbulence phase correction of both beam very nearly restores the no-turbulence performance, and even correction of only one beam nearly restores the no-turbulence spatial resolution, it is of interest to find a way to implement this phase correction. The next chapter presents a system for correction of the turbulence phase and analyzes its performance.

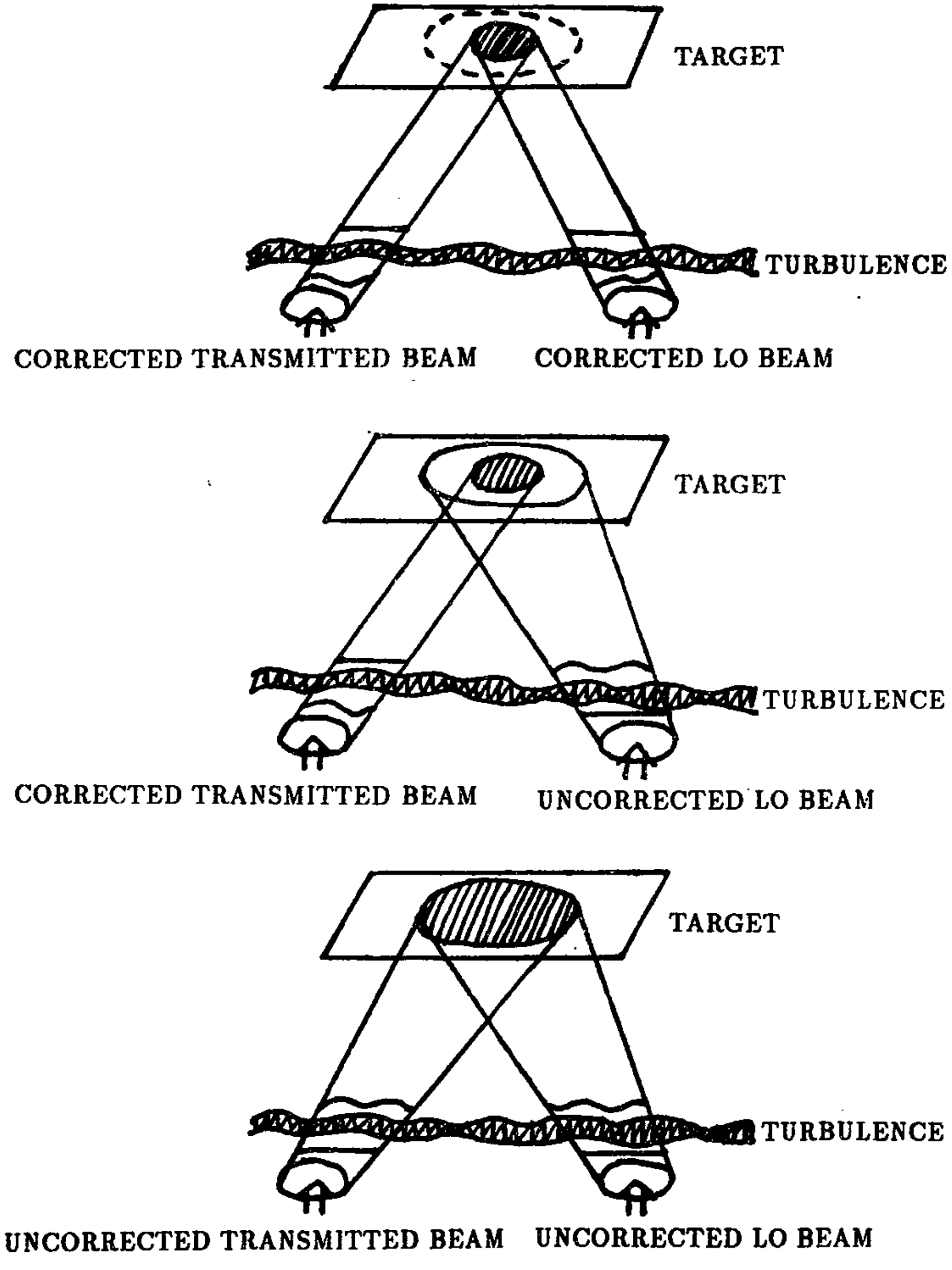

Figure 4.1: Target-plane beam patterns. (a) both beams phase-corrected, (b) only one beam phase-corrected (e.g. transmitted beam), (c) neither beam phase-corrected.

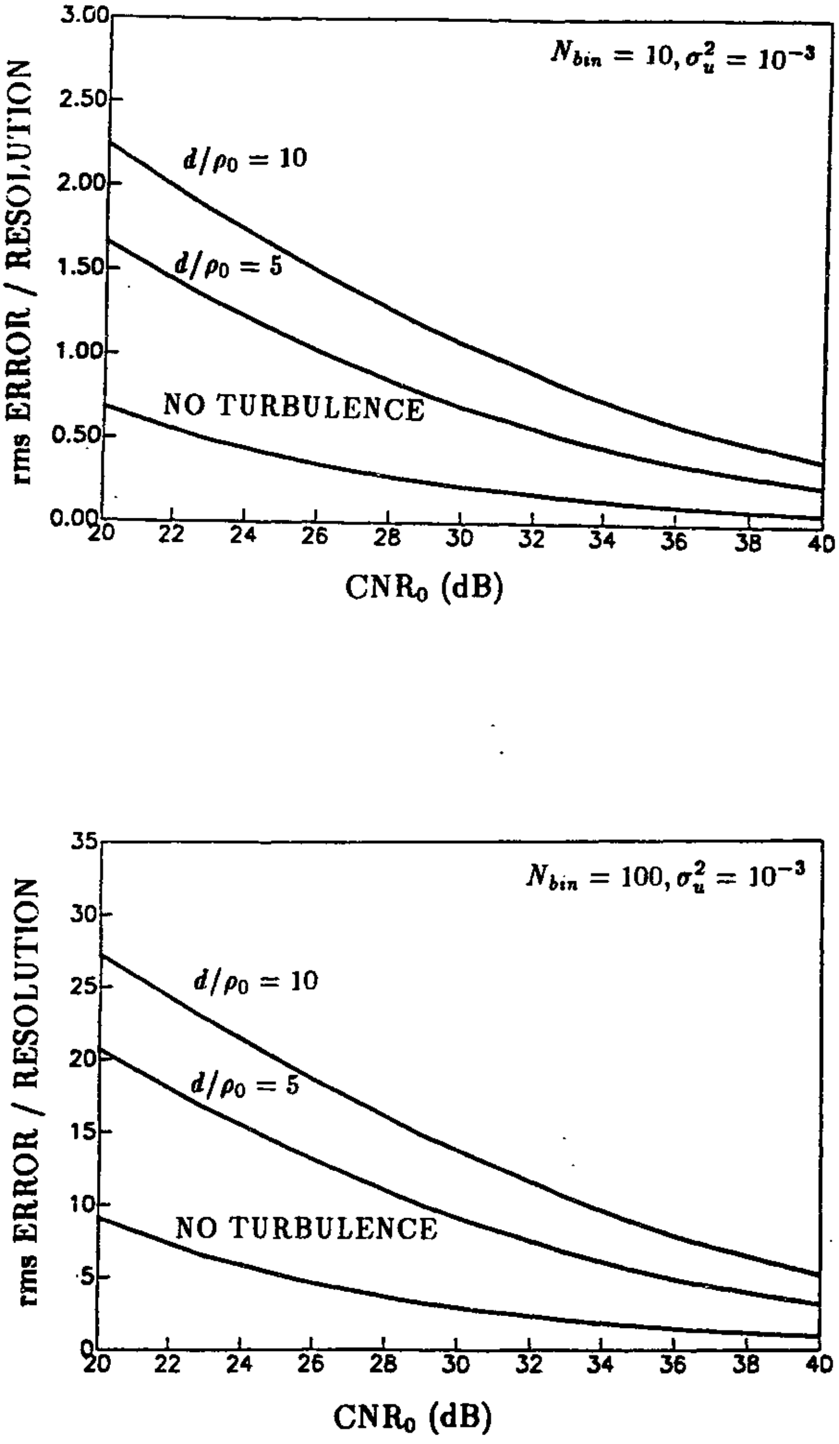

(Figures 4.2a and 4.2b)

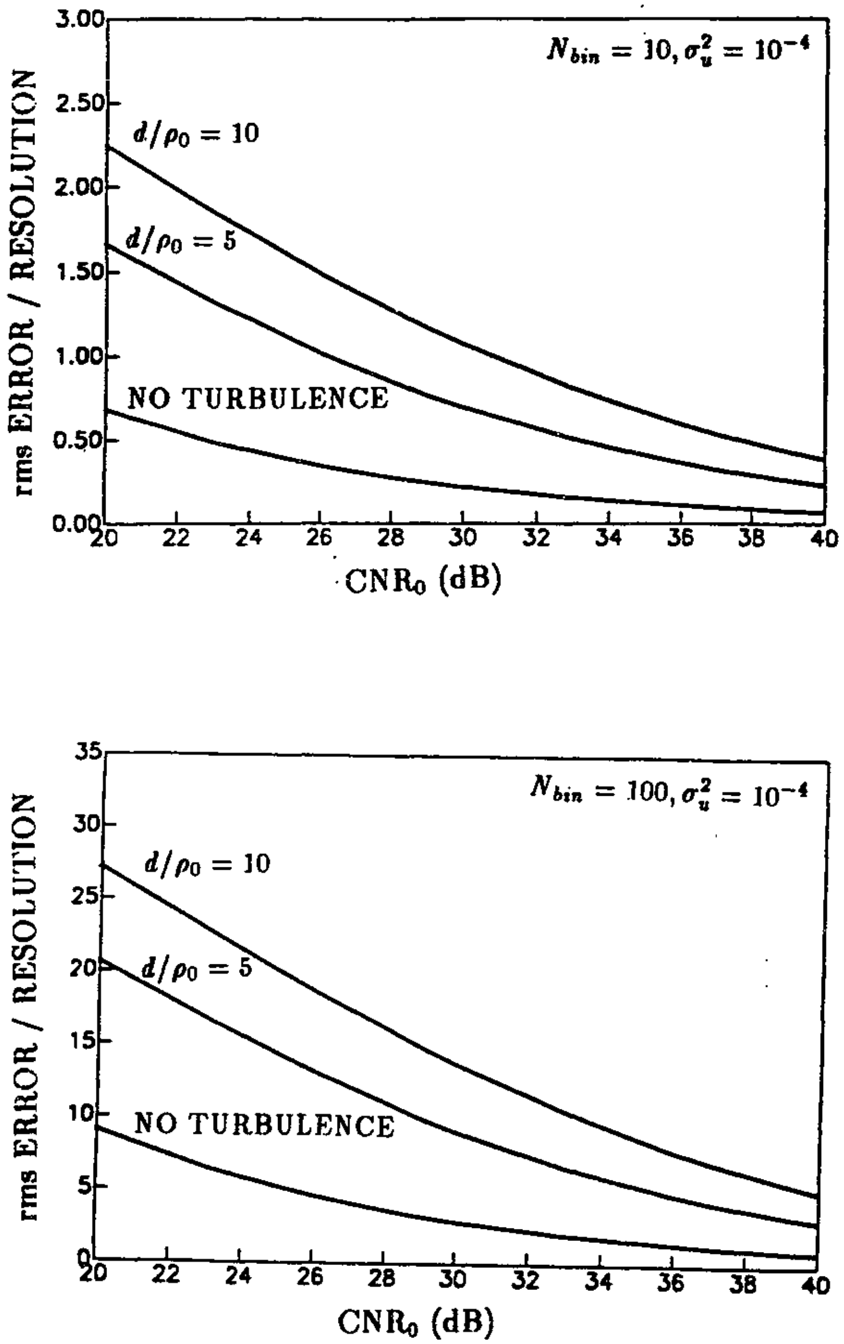

Figure 4.2: Normalized rms range or velocity error vs. carrier-to-noise ratio for various d/ρ_0 values; one beam corrected. (a) $N_{bin} = 10, \sigma_u^2 = 10^{-3}$, (b) $N_{bin} = 100, \sigma_u^2 = 10^{-3}$, (c) $N_{bin} = 10, \sigma_u^2 = 10^{-4}$, (d) $N_{bin} = 100, \sigma_u^2 = 10^{-4}$.

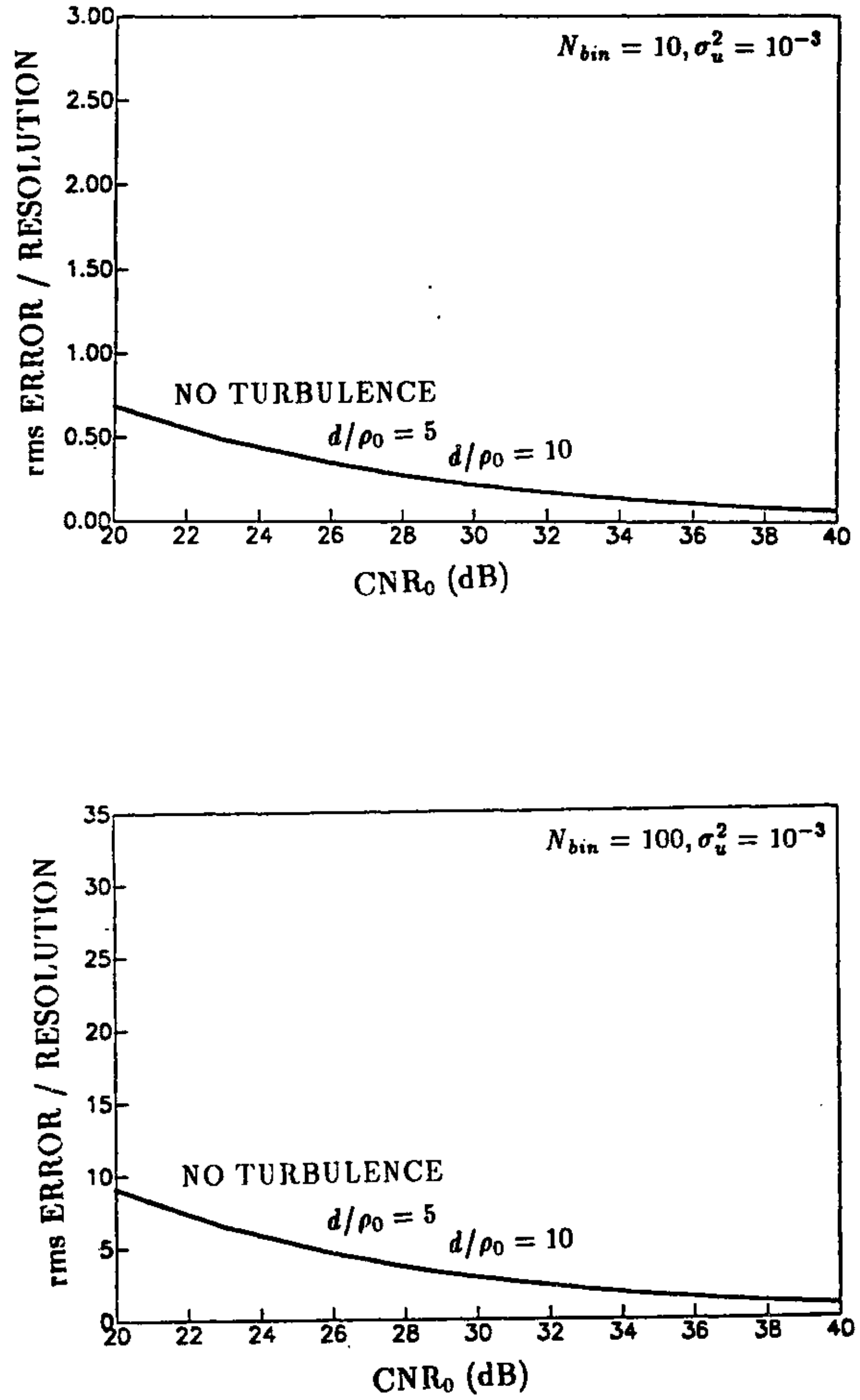

(Figures 4.3a and 4.3b)

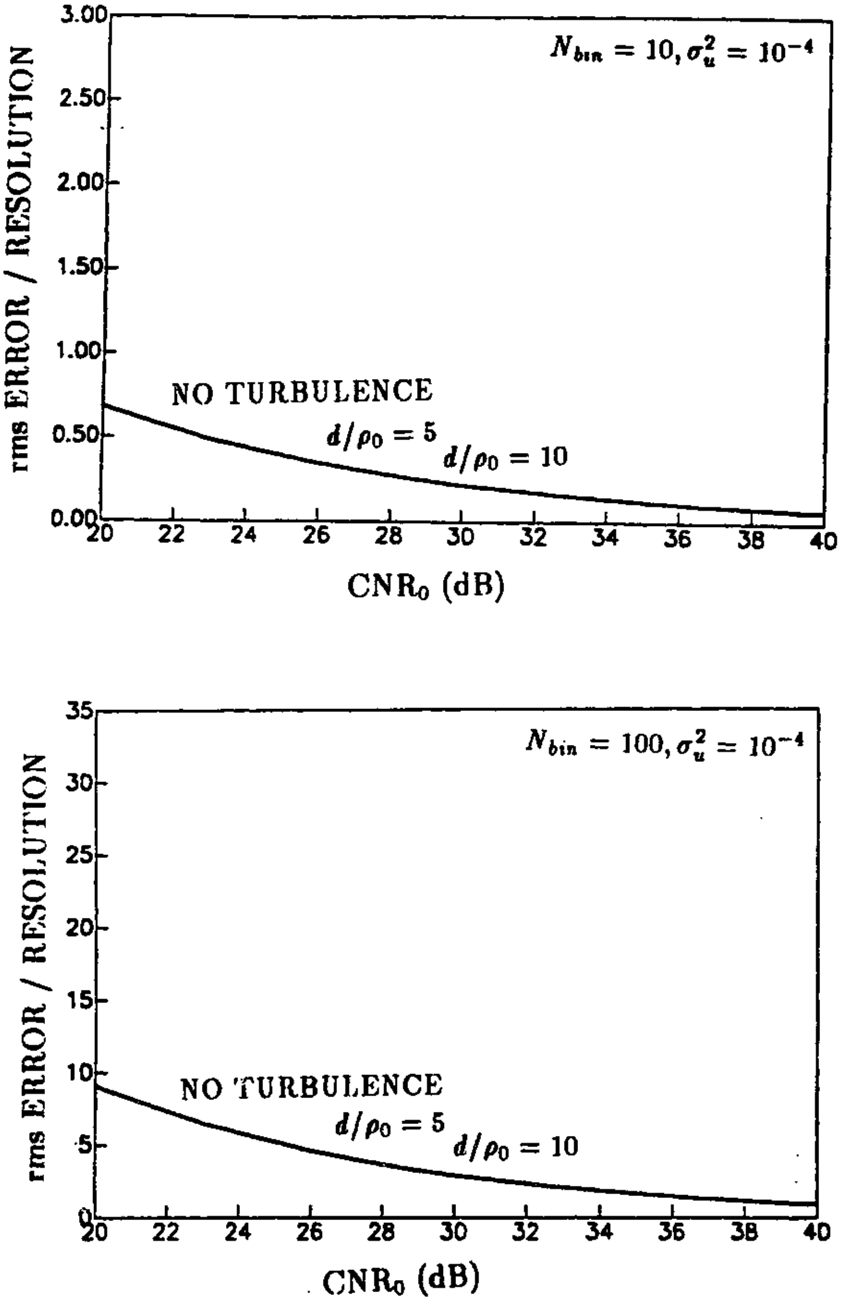

Figure 4.3: Normalized rms range or velocity error vs. carrier-to-noise ratio for various d/ρ_0 values; both beams corrected. (a) $N_{bin} = 10, \sigma_u^2 = 10^{-3}$, (b) $N_{bin} = 100, \sigma_u^2 = 10^{-3}$, (c) $N_{bin} = 10, \sigma_u^2 = 10^{-4}$, (d) $N_{bin} = 100, \sigma_u^2 = 10^{-4}$.

Chapter 5

A Phase Correction System and its Performance

The analysis in Chapter 3 shows that the performance of a coherent laser radar with a large aperture is significantly degraded by turbulence-induced distortions in the illuminator and BPLO beam patterns. The analysis in Chapter 4 shows that the no-turbulence performance can be nearly restored by correcting the transmitter and LO phases for the forward-path and return-path turbulence distortions, respectively. In order to design a system to implement these phase corrections, we must find a way to measure the information necessary to properly correct the wavefront distortions. To correct the LO wave, the turbulence-induced distortion that a wave incurs as it travels through return-path turbulence must be measured. Similarly, to correct the transmitted wave, the turbulence-induced distortion that a wave will incur as it travels through forward-path turbulence must be measured. In general, the only available source of turbulence information in a radar system is the target return. The received wave obviously contains the necessary information about the return-path turbulence, and can therefore be used to correct the LO wave. The turbulence information derived from the received wave could also be used to correct the transmitted wave were the two waves to travel through the same turbulence, because of the reciprocity of the turbulent atmosphere (see Eq. 2.13). However, since the target is moving with respect to the radar, the beam transmitted at a given time must be pointed ahead relative to the direction of arrival of the received beam at that time. Therefore, the turbulence through which the transmitted beam travels is different than the turbulence through which the received beam has traveled. If the point-ahead angle is small enough, then the turbulence in the two paths is highly correlated, so that the return-path turbulence information can still be used to correct the transmitted wave. The point-ahead angle is $2v_\perp/c$, where $v_\perp$ is the component of the target velocity perpendicular to the propagation path, and the angle that a target-plane coherence area subtends at the radar aperture is ρ_0'/L. Therefore, if

$$2v_\perp/c < \rho_0'/L \tag{5.1}$$

is obeyed, as we shall assume here, then the return-path turbulence information can be used to correct the transmitted wave [50]. The speed of a satellite in a circular orbit around the earth is $\sqrt{GM_e/(R_e+Z)}$, [51], where G is the graviatational constant, M_e and R_e are the mass and radius of the earth, and Z is the target altitude. The value of $v_\perp$ is less than or equal to this speed. For a satellite in an orbit at 100 km altitude, and a 10.6 μm wavelength, we find that ρ_0'=55.7 m for daytime turbulence conditions and ρ_0'=63.8 m for nighttime turbulence conditions, assuming a vertical propagation path and the $C_n^2(\eta)$ profiles cited in Chapter 2. In these cases, Eq. 5.1 is satisfied. For slant-path propagation at zenith angle θ to altitude L, $v_\perp = v\sqrt{1-(R_e\sin\theta/(R_e+L))^2}$, where v is the speed of the satellite, and $\rho_0'/L = [\rho_0'(\theta=0)/L](\cos\theta)^{13/5}$, where $\rho_0'(\theta=0)$ is the target-plane atmospheric coherence length for vertical propagation to altitude L. Thus, for sufficiently large zenith angles, Eq. 5.1 may not be satisfied.

The above discussion shows that in many cases of interest, the target return contains the information necessary for correction of both the transmitted and LO waves. If the target return is from a glint, as is generally assumed for adaptive transmitted-wave correction systems[19], or if it is from a spatially unresolved speckle target, then the distortion in the target return over the aperture region is due only to turbulence, so that the turbulence information can be easily extracted from it. However, in our case the target return is from a spatially resolved speckle target, so that the phase distortion of the target return is the sum of the turbulence and speckle phase components. In order to achieve the performance given above for perfect turbulence phase correction, these turbulence and speckle components must be separated. One way to accomplish this separation is to transmit multiple wavelengths, because, as is shown in the next paragraph, the speckle component of the received wave decorrelates more rapidly with wavelength than does the turbulence component. If multiple wavelengths are transmitted—such that the speckle components at each wavelength are uncorrelated but the turbulence components at all wavelengths are highly correlated—then averaging the phases received at the different wavelengths suppresses the speckle distortions without degrading measurement of the turbulence distortions. Speckle averaging (over pulses with independent speckle) has been previously proposed as a way to improve laser radar performance in the absence of turbulence [18]. Speckle reduction using various methods has also been considered in the context of optical imaging (in the absence of turbulence) [37]. The novelty of the radar system presented here is its use of multiple transmitted wavelengths to make it possible to measure the turbulence information which is necessary for wavefront correction from the target return of a spatially resolved speckle target.

The maximum number of wavelengths that can satisfy the above condition may be found by examining the frequency-dependent correlation functions of speckle and turbulence. According to Eq. 2.17, the speckle correlation function is reduced by a factor of e^{-2} when $|\Delta k| = 1/\sigma_h$, where $\Delta k = k_1 - k_2$. As mentioned in Section 2.3, the speckle target reflectivity model used here is valid only if $\sigma_h \gg \lambda_{av}$. Experimental measurements at the 10.6 μm CO_2 laser wavelength [14] have

$\lvert\Delta k\rvert/k_{av}$	$\lvert < e^{\psi(\vec{\rho}',\vec{\rho};k_1,t)} e^{\psi^*(\vec{\rho}',\vec{\rho};k_2,t)} > \rvert$	
	night	day
0.00	1.00	1.00
0.01	0.98	0.94
0.02	0.92	0.77
0.03	0.84	0.56
0.04	0.73	0.36
0.05	0.61	0.20
0.10	0.14	0.002

Table 5.1: Frequency-dependent Turbulence Correlation Function

supported this model. Therefore, we shall assume that $\sigma_h \approx 10\lambda_{av}$ for $\lambda_{av} = 10\,\mu$m (i.e. we assume that $\sigma_h = 100\,\mu$m), so that the speckle is decorrelated when

$$|\Delta k|/k_{av} \geq 0.016, \tag{5.2}$$

where $k_{av} \equiv 2\pi/\lambda_{av}$. We have computed some values of the magnitude of the frequency-dependent correlation function of the turbulence-induced field distortion from Eq. 2.12. These values are listed in Table 5.1 for the daytime and nighttime $C_n^2(\eta)$ profiles given in Chapter 2, with λ_{av}=10.6$\,\mu$m, a 100 m outer scale of turbulence, and $\psi(\cdot) \equiv \chi(\cdot) + i\phi(\cdot)$. From Eq. 5.2 and Table 5.1, it is apparent that if $|k_{max} - k_{min}|/k_{av} = 0.048$, then the nighttime turbulence will be significantly correlated for $k_{min} < k < k_{max}$, and up to four different values of k can be found in this range such that the speckle is uncorrelated. A similar argument shows that for the daytime turbulence, only two different values of k can be found such that the speckle is uncorrelated but the turbulence is significantly correlated. Note that these values for the maximum number of wavelengths have been obtained under the assumption that $\sigma_h = 100\,\mu$m, a reasonable value for typical speckle targets. However, if σ_h were larger, then the speckle would decorrelate more rapidly with wavelength variation, and thus the maximum number of wavelengths would be larger. For $\lambda_{av} = 1\,\mu$m, the maximum number of wavelengths for the nighttime turbulence profile is also four for $\sigma_h = 100\,\mu$m, because although the speckle decorrelates faster at shorter wavelengths, so does the turbulence.

If $\lambda_{av} = 10.6\,\mu$m and four wavelengths are used, then Eq. 5.2 shows that these wavelengths would be 10.35, 10.52, 10.69, and 10.86 μm. This list of wavelengths does not take into consideration the available CO_2 laser lines or the atmospheric absorption spectrum. If two wavelengths were used, then only the second and third of these four wavelengths would be used. For other values of λ_{av}, the values of the wavelengths used can also be found using Eq. 5.2.

5.1 System Structure

The basic structure of the multiwavelength radar system with adaptive wavefront correction is shown in Figure 5.1. The transmitted wave consists of M cw or long-pulse waves for turbulence measurement, as well as a single short-pulse wave if range measurements are made. The wavelength of the latter would be close to one of the former, so that only M LO wavelengths would be necessary. Velocity measurements can be made from one of the cw or long-pulse waves. The transmitter section functions as follows. The uncorrected transmitted beam pattern at each wavelength is the Gaussian beam of Eq. 3.1. The total transmitted wave—comprising all M wavelengths—impinges on an array of N aperture-plane correction elements. The corrected wave is then transmitted, if the target is in the far field, or focused at or near the target plane, if the target is in the near field.

In the receiver section, the free-space phase curvature of the received wave is removed, and then its various wavelengths are separated by a multi-chroic element. Each of the M cw or long-pulse waves is heterodyned with a plane-wave LO beam on an N-element detector array located in a minified aperture plane; the short-pulse wave is heterodyned by the same LO as one of the cw waves, but is beat to a nonoverlapping IF band. The output of the nth detector in the mth array is bandpass filtered and phase detected to yield a phase estimate for that particular detector/wavelength combination. The wavelength-averaged phase estimate for the nth detector element is then obtained by averaging over $1 \leq m \leq M$. If the carrier-to-noise ratio per detector per wavelength is much larger than 1, then this wavelength-averaged phase is the sum of the return-path turbulence phase, plus a speckle component which decreases as M increases, plus a shot noise component which decreases with increasing carrier-to-noise ratio. The wavelength-averaged phase from each detector is sent to the corresponding correction element for transmitter correction. The wavelength-averaged phase from each detector is also sent to its corresponding element in an electrical correction array that performs the electrical equivalent of LO compensation for the (short-pulse and/or cw) signals to be used for radar measurements. These corrected radar signals are summed over all the detectors and processed as in the non-adaptive radar system to produce a range or velocity estimate as well as an intensity estimate.

5.2 System Performance Analysis

First, consider two limiting cases for the performance of this system when the target return is strong enough that shot noise can be completely ignored in the phase estimation. At one extreme, $M = 1$ implies no separation of turbulence and speckle. In this case the applied phase correction is the sum of the turbulence and speckle phases of the received wave. The result of applying this correction to both beams can be seen from a modified version of the extended Huygens-Fresnel principle, Eq. 2.3. For $M = 1$, the turbulence phase in this expression is simply replaced by the conjugate of the received speckle phase. When wave transmission begins, there is not yet any received wave from which to derive information for wavefront correction. Therefore, the transmitted wave is initially uncorrected. This uncorrected transmitted wave gives rise, after round-trip propagation, to a received wave whose speckle component has a correlation length of the order of ρ_0. Thus, the phase correction applied to both waves is the sum of the proper turbulence phase correction, and a speckle phase whose correlation length is of the order of ρ_0. The corrected transmitted wave then gives rise, after round-trip propagation, to a received wave whose speckle component again has a correlation length of the order of ρ_0. Thus, the phase correction applied to both waves is again the sum of the proper turbulence phase correction, and a speckle phase whose correlation length is of the order of ρ_0. Repeating this argument for each round-trip propagation of the transmitted wave shows that the spatial resolution of the $M = 1$ adaptive system *cannot* be diffraction limited. In fact, the system performance analysis given below shows that the spatial resolution is *worse* than turbulence-limited, i.e., worse than the resolution with no correction. On the other hand, the $M = 1$ LO correction gives a better CNR than the correction for other values of M, because of its more-perfect spatial matching between the received wave and the LO wave.

At the other extreme, $M = \infty$ implies that the variance of the wavelength-averaged speckle phase is zero, so that the speckle component of the applied correction is completely suppressed. Because we are still assuming that the shot noise is negligible in the phase estimation, the applied phase correction in this case will be just the turbulence phase, so that the performance will be very close to that in the no-turbulence state, as explained in Chapter 4. Although, in principle, it may be possible to achieve very large values of M, this is not so when turbulence and speckle are separated by transmitting multiple wavelengths. For $\sigma_h = 100\,\mu\text{m}$ and for the $C_n^2(\eta)$ profiles used here, the maximum value of M is four. Therefore, the system performance will be analyzed for arbitrary M values, but numerical evaluations will be done only for M=1,2 and 4. We shall also account for the effects of shot noise on the phase estimation in the following analysis. Furthermore, the log-amplitude fluctuations are neglected in the following analysis, because their variance is so small that their effect on the radar's performance is negligible, as was shown in Chapter 4.

The transmitted wave leaving the radar exit optics at time t in the Figure 5.1 structure has normalized complex envelope

$$\zeta_T(\vec{\rho};t) = \int d\vec{\rho}_1 \, h(\vec{\rho}-\vec{\rho}_1)\xi_0(\vec{\rho}_1)e^{-i\hat{\phi}(\vec{\rho}_1;t)} \tag{5.3}$$

for all M wavelengths, where $\hat{\phi}(\vec{\rho};t)$ is the estimate of the return-path turbulence phase for all M wavelengths, $\phi_R(\vec{\rho},\vec{0};t)$, and where we have used the low-pass spatial impulse response,

$$h(\vec{\rho}) = \frac{N\pi}{d^2}e^{-N\pi^2\rho^2/d^2}, \tag{5.4}$$

as an approximate representation of the fitting error caused by there being only N correction elements in the compensation array. In Eq.5.3, $\xi_0(\cdot)$ is the Gaussian-beam uncompensated wavefront from Eq. 3.1. The number of elements in each correction and detector array, N, is assumed to be large enough that the turbulence distortion is constant over each array element. When this adaptive optics system is enabled, there is initially no received wave from which to measure any turbulence information for wavefront correction. The transmitted beam at this time is uncorrected, so that in the notation of Eq. 5.3,

$$\hat{\phi}(\vec{\rho};t) = 0 \quad \text{for } t_0 \leq t < t_0 + \frac{2L}{c}, \tag{5.5}$$

where t_0 is the time at which wave transmission begins. In writing Eq. 5.3, it has been assumed that the spot distribution on target which gives rise to the received wave is confined to a single turbulence coherence area in the target plane. That is, we assume that Eq. 4.1, the condition for the SCA approximation, is satisfied. If it is not satisfied, i.e. if the spot distribution on target which gives rise to the received wave covers more than one target-plane coherence area, then the conjugate of the received turbulence phase is the *sum* of the corrections to apply for transmission to each of these target-plane coherence areas [52]. In that case, it would be necessary to decompose this sum in order to find the correction to apply for transmission to a *particular* target-plane coherence area. It may not be possible to achieve this decomposition. However, if Eq. 4.1 is satisfied, then the conjugate of the received turbulence phase is itself the proper correction to apply when transmitting to the single target-plane turbulence coherence area. The illuminator beam pattern at wavelength k_m follows from Eq. 2.3, and is given by

$$\xi_t\left(\vec{\rho}\,';k_m,t+\frac{L}{c}\right)=e^{-\alpha L/2}\int_R d\vec{\rho}\,\zeta_T(\vec{\rho};t)\,e^{i\phi_F(\vec{0},\vec{\rho};t)}\,\frac{e^{ik_mL}}{i\lambda_mL}\,e^{i\frac{k_m}{2L}\rho'^2}\,e^{-i\frac{k_m}{L}\vec{\rho}\,'\cdot\vec{\rho}}, \tag{5.6}$$

where $\phi_F(\vec{0},\vec{\rho};t)$ is the phase distortion due to forward-path turbulence for all of the wavelengths. The turbulence-induced amplitude distortions are neglected here, since it was found in Chapter 4 that they have a very small effect on the radar performance when the target is high above the atmosphere, and the wavelength is in the infrared region. Note that the transmitted spatial beam pattern of Eq. 5.3 does not depend on wavelength, but the transmitted *wave* (see Eq. 2.2) does. Also, the free-space propagation kernel (the last three factors in Eq. 5.6) depends on the transmitted wavelength, and thus the illuminator beam pattern depends on the transmitted wavelength.

The received speckle pattern is given by

$$\begin{aligned}\zeta_R^0\left(\vec{\rho};k_m,t+\frac{2L}{c}\right) &= e^{-\alpha L/2}\int d\vec{\rho}_1\,h(\vec{\rho}-\vec{\rho}_1)\int d\vec{\rho}\,'\,\xi_t\left(\vec{\rho}\,';k_m,t+\frac{L}{c}\right)\cdot\\ &\qquad \mathbf{T}\left(\vec{\rho}\,',k_m,t+\frac{L}{c}\right)\frac{e^{ik_mL}}{i\lambda_mL}\,e^{i\frac{k_m}{2L}\rho'^2}\,e^{-i\frac{k_m}{L}\vec{\rho}_1\cdot\vec{\rho}\,'},\end{aligned} \tag{5.7}$$

where, in this case, the low-pass spatial impulse response $h(\cdot)$ models the spatial-frequency limitations of the N element detector array. The total received beam pattern is the above speckle pattern multiplied by $e^{i\phi_R(\vec{\rho},\vec{0};t+2L/c)}$.

Eqs. 5.3 through 5.7 describe the round-trip propagation of the corrected transmitted beam pattern, whether the transmitted beam is cw or pulsed. The following analysis concerns the waves used for measurement of turbulence and possibly velocity, which are cw. However, with minor modifications the analysis also applies to a pulsed wave, where P_T would be replaced by $E_T B$.

The part of the received beam pattern which impinges on the nth detector associated with the mth wavelength gives rise, after IF filtering to an IF signal with the following baseband complex envelope:

$$\mathbf{r}_n\left(k_m, t + \frac{2L}{c}\right) \equiv \boldsymbol{\ell}_n\left(k_m, t + \frac{2L}{c}\right) + \mathbf{n}_n\left(k_m, t + \frac{2L}{c}\right), \quad \text{for } m = 1 \text{ to } M. \tag{5.8}$$

Here $\boldsymbol{\ell}_n(k_m, t + 2L/c)$ is the target-return component, given by

$$\begin{aligned} \boldsymbol{\ell}_n\left(k_m, t + \frac{2L}{c}\right) &= \sqrt{P_T \epsilon_{opt}}\, e^{i(4\pi v_\parallel/\lambda_m)t} \cdot \\ &\int_{R_n} d\vec{\rho}\, \zeta_R^0\left(\vec{\rho}; k_m, t + \frac{2L}{c}\right) e^{i\phi_R(\vec{\rho},\vec{0};t+2L/c)} \xi_{LO}^*(\vec{\rho}), \end{aligned} \tag{5.9}$$

where R_n denotes the region of the radar aperture that minifies to the nth detector region in the photodetector array. In writing Eq. 5.9, it was assumed that the IF filter's bandwidth is large enough to pass the target return in an undistorted way. Also, the antenna theorem for heterodyne detection has been used to express the spatial overlap integral of Eq. 2.24 (for $\ell(k,t)$) in the radar aperture plane. The LO beam pattern used here is a truncated plane wave over the aperture region R, so that each part of the received wavefront undergoes the same LO-beam mixing gain in the heterodyne process, and therefore the phase estimates for each part of the wavefront have the same statistics. Thus,

$$\xi_{LO}^*(\vec{\rho}) = \sqrt{\frac{4N}{\pi d^2}} \quad \text{for } \vec{\rho} \epsilon R_n. \tag{5.10}$$

Furthermore, the received wave is assumed to be approximately constant in space over a detector region, for analytical convenience. This assumption can be justified as follows. To get good turbulence correction, N must be large enough that the turbulence distortion is nearly constant over each detector. This implies that the size of each detector must be smaller than ρ_0. The coherence length of the received speckle field, $\zeta_R^0(\vec{\rho}; k_m, t + 2L/c)$, is approximately $\lambda_m L/$[target-plane spot length]. Since the target-plane spot length is less than or equal to $\lambda_m L/\rho_0$, the turbulence-limited value, it follows that the coherence length of the received speckle field is greater than or equal to ρ_0. Because the coherence lengths of both the received turbulence distortion and the received speckle field are at least ρ_0, and the detector size is less than ρ_0, it is assumed that the received wave is approximately constant over a detector region. Therefore, it follows from Eqs. 5.9 and 5.10 that

$$\begin{aligned} \ell_n\left(k_m, t + \frac{2L}{c}\right) &= \sqrt{\frac{\pi P_T \epsilon_{opt} d^2}{4N}} e^{i(4\pi v_{\|}/\lambda_m)t} \zeta_R^0\left(\vec{\rho}_n; k_m, t + \frac{2L}{c}\right) \cdot \\ & \quad e^{i\phi_R(\vec{\rho}_n, \vec{0}; t+2L/c)}, \end{aligned} \tag{5.11}$$

with P_T equal to the power transmitted at each wavelength, and $\vec{\rho}_n$ being the center coordinate of R_n. The shot noise $\mathbf{n}_n(k_m, t)$ of Eq. 5.8 is a zero-mean low pass Gaussian random process for which

$$\langle |\mathbf{n}_n(k_m, t)|^2 \rangle = h\nu_0 B/\eta, \tag{5.12}$$

and which is statistically independent from one detector to another, and from one wavelength to another.

The set of IF signals $\{\mathbf{r}_n(k_m, t)\}$ is used for two purposes: measurement of the turbulence phase distortion in the received wave, and radar measurements. First the process of making turbulence phase measurements from $\mathbf{r}_n(k_m, t)$ is described, and then the process of making radar measurements is described.

When $|\ell_n(\cdot)|$ is large compared to $|\mathbf{n}_n(\cdot)|$ with high probability—when the carrier-to-noise ratio *on each detector* is high—the phase of the total IF signal $\mathbf{r}_n(\cdot) = \ell_n(\cdot) + \mathbf{n}_n(\cdot)$ can be linearized. The diagram in Figure 5.2 shows $\mathbf{r}_n(\cdot)$, $\ell_n(\cdot)$, and $\mathbf{n}_n(\cdot)$ in the complex plane. It can be seen by inspection that

$$|\mathbf{r}_n| \sin(\angle \mathbf{r}_n - \angle \ell_n) = |\mathbf{n}_n| \sin(\angle \mathbf{n}_n - \angle \ell_n). \tag{5.13}$$

Therefore,

$$\angle \mathbf{r}_n = \angle \boldsymbol{\ell}_n - \sin^{-1}\left[\frac{|\mathbf{n}_n|}{|\boldsymbol{\ell}_n + \mathbf{n}_n|}\sin(\angle \boldsymbol{\ell}_n - \angle \mathbf{n}_n)\right]. \tag{5.14}$$

When $|\boldsymbol{\ell}_n|$ is large compared to $|\mathbf{n}_n|$, then the magnitude of the argument of the inverse sine is much less than one, so that the inverse sine can be linearized. The result is

$$\angle \mathbf{r}_n \approx \angle \boldsymbol{\ell}_n - \frac{|\mathbf{n}_n|}{|\boldsymbol{\ell}_n|}\sin(\angle \boldsymbol{\ell}_n - \angle \mathbf{n}_n), \tag{5.15}$$

where we have also used the additional approximation $|\mathbf{n}_n|/|\boldsymbol{\ell}_n + \mathbf{n}_n| \approx |\mathbf{n}_n|/|\boldsymbol{\ell}_n|$. The validity of the approximation of Eq. 5.15 is examined in the Appendix by comparing the probability distributions of the exact and approximate phases of $\mathbf{r}_n$, and it is found to be a good approximation for $\mathrm{CNR}_{\mathrm{det}} \geq 10$, where

$$\begin{aligned} \mathrm{CNR}_{\mathrm{det}}(m,t) &\equiv \frac{\langle |\boldsymbol{\ell}_n(k_m,t)|^2\rangle}{\langle |\mathbf{n}_n(k_m,t)|^2\rangle} \\ &= \frac{\eta P_T \epsilon_{opt}}{h\nu_0 B}\frac{\pi d^2}{4N}\langle |\zeta_R^0(\vec{\rho};k_m,t)|^2\rangle \end{aligned} \tag{5.16}$$

is the carrier-to-noise per detector per wavelength. Within the linearization regime we have that the wavelength-averaged phase measurement yields the phase estimate

$$\hat{\phi}_n\left(t + \frac{2L}{c}\right) = \phi_R\left(\vec{\rho}_n, \vec{0}; t + \frac{2L}{c}\right) + \bar{\phi}_{sp}\left(\vec{\rho}_n; t + \frac{2L}{c}\right) \tag{5.17}$$

where

$$\begin{aligned} \bar{\phi}_{sp}\left(\vec{\rho}_n; t + \frac{2L}{c}\right) &\equiv \frac{1}{M}\sum_{m=1}^{M} \angle \zeta_R^0\left(\vec{\rho}_n; k_m, t + \frac{2L}{c}\right) \\ &\quad - \frac{1}{M}\sum_{m=1}^{M}\frac{|\mathbf{n}_n(k_m, t + 2L/c)|}{|\boldsymbol{\ell}_n(k_m, t + 2L/c)|}\sin\left(\angle \boldsymbol{\ell}_n\left(k_m, t + \frac{2L}{c}\right) - \angle \mathbf{n}_n\left(k_m, t + \frac{2L}{c}\right)\right). \end{aligned} \tag{5.18}$$

The Doppler frequency shift in $\boldsymbol{\ell}(k_m, t + 2L/c)$ is assumed to be tracked and cancelled in that part of the set of IF signals which is used for turbulence phase measurements; it is therefore neglected in the expression for the phase estimate. This tracking and cancelling should be done if velocity measurements are to be made, so that the applied wavefront correction does not cancel the Doppler frequency shift in the received wave. The phase estimate of Eq. 5.17 is substituted into Eq. 5.3 to give the corrected transmitted wave at time $t + 2L/c$, where $\hat{\phi}(\vec{\rho};t) \equiv \hat{\phi}_n(t)$ for $\vec{\rho}$ in the region R_n. This phase estimate is also used for correction of the signal used for radar measurement, a correction equivalent to phase correction of the LO wavefront.

Intensity and/or velocity measurements can be made from the set of cw signals $\mathbf{r}_n(k_m, t)$ as follows. Intensity measurements can be made by first summing over m to get the total signal from each detector, and then correcting each of these total signals by using the turbulence phase estimate $\hat{\phi}_n(t)$. All of these corrected signals are then added up to get the total corrected IF signal, which is processed to extract the target information as it would be processed in a nonadaptive system. Velocity measurements can be made from one or more of the wavelength components of the received wave by phase-correcting and processing each component individually. If the *sum* of the wavelength components were corrected and processed, then the velocity resolution would be slightly degraded. For example, for $M = 4$ and $k_{av} = 2\pi/(10.6\,\mu\text{m})$, the velocity resolution would vary about 5 percent between the smallest and largest wavelengths. If range measurements are to be made, then there will be an additional set of IF filters for one of the LO wavelengths, giving a set of pulsed IF signals $\mathbf{r}'_n(t)$. Each of these signals is corrected by using the turbulence phase estimate $\hat{\phi}_n(t)$, and the corrected signals are summed over n to give the total corrected IF signal, which is processed to extract the target information as it would be processed in a nonadaptive system. The following analysis deals with the cw waves for the case of intensity measurements (for the case of velocity measurements the sum over the M wavelengths would be dropped), and the analysis for a pulsed wave would proceed in a similar way.

According to the above-mentioned system description, and Eqs. 5.8 and 5.11, the total IF signal from each detector has the following baseband complex envelope:

$$\mathbf{r}_n\left(t+\frac{2L}{c}\right) = \sqrt{\frac{\pi P_T \epsilon_{opt} d^2}{4N}} e^{i\phi_R(\vec{\rho}_n,\vec{0};t+2L/c)} \sum_{m=1}^{M} e^{i(4\pi v_{\parallel}/\lambda_m)t} \zeta_R^0\left(\vec{\rho}_n; k_m, t+\frac{2L}{c}\right) + \sum_{m=1}^{M} \mathbf{n}_n\left(k_m, t+\frac{2L}{c}\right). \tag{5.19}$$

The corrected signal from detector n is given by

$$\mathbf{r}_n\left(t+\frac{2L}{c}\right) e^{-i\hat{\phi}_n(t+2L/c)}, \tag{5.20}$$

where $\hat{\phi}_n(t+2L/c)$ is given by Eq. 5.17. The total corrected signal is therefore given by $\ell_{\text{radar}}(t) + \mathbf{n}_{\text{radar}}(t)$, where the target-return component is

$$\ell_{\text{radar}}(t) \equiv \sqrt{\frac{\pi P_T \epsilon_{opt} d^2}{4N}} \sum_{n=1}^{N} e^{-i\bar{\phi}_{sp}(\vec{\rho}_n;t)} \sum_{m=1}^{M} e^{i(4\pi v_{\parallel}/\lambda_m)t} \zeta_R^0(\vec{\rho}_n; k_m, t), \tag{5.21}$$

and the shot noise component is

$$\mathbf{n}_{\text{radar}}(t) \equiv \sum_{m=1}^{M} \sum_{n=1}^{N} \mathbf{n}_n(k_m, t) e^{-i[\phi_R(\vec{\rho}_n,\vec{0};t)+\bar{\phi}_{sp}(\vec{\rho}_n;t)]}. \tag{5.22}$$

The function $\zeta_R^0(\vec{\rho}; k_m, t)$ is approximately spatially constant over each detector since it is defined as the spatially low-pass filtered received speckle field. Since $\bar{\phi}_{sp}(\vec{\rho}; t)$ is an average of the phases of $\zeta_R^0(\vec{\rho}; k_m, t)$ at the different wavelengths, it too is approximately constant over each detector. Therefore, the sum over n in Eq. 5.21 can be replaced by an integral, as follows

$$\ell_{\text{radar}}(t) = \sqrt{P_T \epsilon_{opt}} \sum_{m=1}^{M} e^{i(4\pi v_{\parallel}/\lambda_m)t} \int_R d\vec{\rho}\, \zeta_R^0(\vec{\rho}; k_m, t)\, e^{-i\bar{\phi}_{sp}(\vec{\rho};t)}\, \xi_{LO}^*(\vec{\rho}), \tag{5.23}$$

where Eq. 5.10 has been used for $\xi_{LO}^*(\vec{\rho})$.

The performance of this system can now be derived from Eqs. 5.3 through 5.23, which describe the operation of this system. These equations show that this system is a closed loop, because the transmitter correction is derived from the received wave, and the received wave is the result of propagation of the transmitted wave to the target and back. As mentioned in Eq. 5.5, for the first $2L/c$ seconds of wave transmission, the transmitted wave is uncorrected. Therefore, during this time period the phase distortion in the transmitted wave is simply the turbulence phase distortion. At time $t_0 + 2L/c$ the received wave first reaches the radar. From this time until time $t_0 + 4L/c$, the phase correction applied to the transmitted wave is the sum of the proper turbulence phase correction, and the speckle phase arising from an uncorrected transmitted wave. Thus, the transmitted phase between times $t_0 + 2L/c$ and $t_0 + 4L/c$ has different statistical properties than the transmitted phase between times t_0 and $t_0 + 2L/c$. These different statistical properties of the transmitted phase give rise to different statistical properties of the received speckle phase. Thus, the received speckle phase between times $t_0 + 4L/c$ and $t_0 + 6L/c$ has different statistical properties than the received speckle phase between times $t_0 + 2L/c$ and $t_0 + 4L/c$. Therefore, the transmitted phase correction between times $t_0 + 4L/c$ and $t_0 + 6L/c$ has different statistical properties than the transmitted phase correction between times $t_0 + 2L/c$ and $t_0 + 4L/c$. Continuing this argument shows that the statistical properties of the transmitted wave change at every $2L/c$ time increment after t_0.

What happens during each of these time intervals? In the speckle and turbulence models used here, the statistical properties of the speckle and of the turbulence are time-invariant. Thus, the statistical properties of the transmitted wave are time-invariant during each of the $2L/c$ time intervals, but they change at each multiple of $2L/c$ after t_0. Since these statistical properties change in a discrete manner, we shall say that the state of the system—i.e. the statistical properties of the transmitted wave, and quantities derived from these statistical properties—goes through an *iteration* during each $2L/c$ time interval after t_0. Note that although the statistics of the transmitted wave change in a discrete manner, the wave itself changes in a continuous manner.

Because of the closed-loop nature of this system, it can be argued that the system's spatial resolution should improve from one iteration to the next until it reaches a limiting value. In particular, in the first iteration (between t_0 and $t_0 + 2L/c$), the transmitted phase is the turbulence phase. The averaging of the speckle phase in the received wave leads to a corrected transmitted phase which has a larger coherence length than that of the transmitted phase in the first iteration. This increase in the coherence length of the transmitted phase from the first iteration to the second results in a smaller average spot size on target. The decrease in spot size on target from the first iteration to the second gives rise to a received speckle pattern with a larger coherence length in the second iteration. The coherence length of this received speckle pattern is then increased in the speckle averaging process. Therefore, in the third iteration the transmitted phase has both a reduced variance and an increased coherence length relative to the variance and coherence length of the transmitted phase in the second iteration. Thus, the average spot size on target in the third iteration is even smaller than that in the second iteration. Continuing this argument shows that this reduction in spot size on target should continue in each iteration until some phenomenon, e.g. diffraction or incomplete speckle suppression, prevents a further reduction. Because of the increased coherence length of the speckle component of the received phase in each iteration, the applied corrections derived from this received phase become closer to the perfect turbulence phase corrections which were discussed in Chapter 4. Thus, the spatial resolution, CNR and range and velocity accuracy should also improve in each iteration until they reach their steady-state values.

The following analysis leads to a quantitative confirmation of the above argument. In this analysis, the mean illuminator beam intensity is derived for each iteration in order to quantitatively examine the existence of and convergence to the steady state. From Eqs. 5.6, 5.3, 5.4, and 5.17, it follows that the mean intensity distribution on target is

$$\langle|\xi_t(\vec{\rho}\,';k_m,t+L/c)|^2\rangle = e^{-\alpha L}\frac{1}{(\lambda_m L)^2}e^{-\frac{2}{N}\left(\frac{d\rho'}{\lambda_m L}\right)^2}\frac{16}{\pi d^2}\cdot$$
$$\int d\vec{\rho}_1\int d\vec{\rho}_2\, e^{-\frac{4}{d^2}(\rho_1^2+\rho_2^2)}e^{-i\frac{k_m}{L}\vec{\rho}\,'\cdot(\vec{\rho}_1-\vec{\rho}_2)}\langle\exp(-i\bar{\phi}_{sp}(\vec{\rho}_1;t))\exp(i\bar{\phi}_{sp}(\vec{\rho}_2;t))\rangle \quad (5.24)$$

The correlation function of $\exp(-i\bar{\phi}_{sp}(\vec{\rho};t))$ can now be found from Eq. 5.18. The average over the shot noise statistics can be done by noting that $\mathbf{n}_n(k_m,t)$ and $\mathbf{n}_{n'}(k_{m'},t)$ are statistically independent for $n \neq n'$ or $m \neq m'$, and that

$$p_{\mathbf{n}}(\mathrm{N}) = \frac{1}{\pi\langle|\mathbf{n}|^2\rangle}e^{-\frac{|\mathrm{N}|^2}{\langle|\mathbf{n}|^2\rangle}} \quad (5.25)$$

where $\langle|\mathbf{n}|^2\rangle$ is given by Eq. 5.12. Averaging over the shot noise statistics gives, for $\vec{\rho}_1$ and $\vec{\rho}_2$ on different detectors,

$$\langle\,\exp(-i\bar{\phi}_{sp}(\vec{\rho}_1;t))\exp(i\bar{\phi}_{sp}(\vec{\rho}_2;t))\mid\{\ell_n(k_m;t)\}\,\rangle_{\text{shot noise}} =$$
$$\prod_{m=1}^{M}\exp\left[-i\frac{(\theta_{1m}-\theta_{2m})}{M}-\frac{1}{4M^2\mathrm{CNR}_{\mathrm{det}}(m,t)}\left(\frac{\langle r_{1m}^2\rangle}{r_{1m}^2}+\frac{\langle r_{2m}^2\rangle}{r_{2m}^2}\right)\right], \quad (5.26)$$

where $r_{1m}e^{i\theta_{1m}} \equiv \zeta_R^0(\vec{\rho}_1;k_m,t)$ and $r_{2m}e^{i\theta_{2m}} \equiv \zeta_R^0(\vec{\rho}_2;k_m,t)$. If $\vec{\rho}_1$ and $\vec{\rho}_2$ are on the same detector, then the right-hand side of Eq. 5.26 would be replaced by $\prod_{m=1}^{M}\exp(-i(\theta_{1m}-\theta_{2m})/M)$. In evaluating Eq. 5.24, the appropriate expression would be used, depending on whether $\vec{\rho}_1$ and $\vec{\rho}_2$ are on the same or different detectors. In order to average Eq. 5.26, we need the joint probability distribution for the quantities $\zeta_R^0(\vec{\rho}_1;k_m,t)$ and $\zeta_R^0(\vec{\rho}_2;k_m,t)$, which are given by Eq. 5.7. It is assumed here that they are jointly Gaussian random variables for the following reason. When the system is first turned on, the transmitted wave is uncorrected, so $\xi_t(\vec{\rho}\,';k_m,t_0+L/c)$ has many coherence areas. Therefore, by the central limit theorem, $\zeta_R^0(\vec{\rho};k_m,t_0+2L/c)$ is approximately Gaussian. After several iterations, $\xi_t(\vec{\rho}\,';k_m,t)$ has been well corrected, so that the randomness of $\zeta_R^0(\vec{\rho};k_m,t)$ is dominated by the target speckle, which is Gaussian. Therefore it is assumed that $\zeta_R^0(\vec{\rho};k_m,t)$ is Gaussian for all time. Furthermore, it is zero mean. Therefore, using the joint probability distribution for $r_{1m}, \theta_{1m}, r_{2m}$, and θ_{2m} it can be shown that[53]

$$\left\langle e^{-i\bar{\phi}_{sp}(\vec{\rho}_1;t+\frac{2L}{c})} e^{i\bar{\phi}_{sp}(\vec{\rho}_2;t+\frac{2L}{c})} \right\rangle =$$

$$\prod_{m=1}^{M} \frac{1}{\pi^2}(1-|\mathbf{x}_m|^2) \cdot \int_0^{2\pi} d\theta_1 \int_0^{2\pi} d\theta_2 \int_0^{\infty} du_1 \int_0^{\infty} du_2\, u_1 u_2$$

$$\exp\Big(-(u_1^2+u_2^2-2|\mathbf{x}_m|u_1u_2\cos(\theta_1-\theta_2-\angle\mathbf{x}_m))\Big)\exp\Big(-i\frac{1}{M}(\theta_1-\theta_2)\Big)$$

$$\exp\left(-\frac{1}{4M^2\mathrm{CNR}_{\mathrm{det}}(m,t+\frac{2L}{c})}\cdot\frac{1}{1-|\mathbf{x}_m|^2}\cdot\left(\frac{1}{u_1^2}+\frac{1}{u_2^2}\right)\right), \tag{5.27}$$

where

$$\mathbf{x}_m(\vec{\rho}_1,\vec{\rho}_2;t+2L/c) \equiv \frac{\langle \zeta_R^0(\vec{\rho}_1;k_m,t+\frac{2L}{c})\zeta_R^{0*}(\vec{\rho}_2;k_m,t+\frac{2L}{c})\rangle}{\langle|\zeta_R^0(\vec{\rho};k_m,t+\frac{2L}{c})|^2\rangle}. \tag{5.28}$$

Note that the denominator of Eq. 5.28 appears to depend on $\vec{\rho}$. However, it is actually spatially constant, as can be verified by evaluating it using Eq. 5.7. This evaluation is carried out below in Eq. 5.29.

For the case in which $\vec{\rho}_1$ and $\vec{\rho}_2$ are on different detectors, Eq. 5.27 gives the spatial correlation function $\langle\exp(-i\bar{\phi}_{sp}(\vec{\rho}_1;t+2L/c))\cdot\exp(i\bar{\phi}_{sp}(\vec{\rho}_2;t+2L/c))\rangle$. If $\vec{\rho}_1$ and $\vec{\rho}_2$ are on the same detector, then this spatial correlation function is given by the right-hand side of Eq. 5.27 without the final exponential term. Thus, the spatial correlation function for $\exp(i\bar{\phi}_{sp}(\vec{\rho},t))$ will be given by Eq. 5.27 except for some pairs of points for which $|\vec{\rho}_1-\vec{\rho}_2| < d/\sqrt{N}$ (i.e. pairs of points which are on the same detector). However, we shall make the approximation of using Eq. 5.27 for *all* pairs of points $\vec{\rho}_1$ and $\vec{\rho}_2$, for analytical convenience. This approximation can be justified as follows. As mentioned earlier, to get good turbulence correction N must be large enough that the turbulence distortion is nearly constant over each detector. This condition implies that N is large compared to $(d/\rho_0)^2$. Thus, Eq. 5.27 will be applicable except for some pairs of points whose separation is small compared to ρ_0. At pairs of points so close together, the received speckle pattern is highly correlated, so that $|\mathbf{x}_m|$ is close to 1, as can be seen from Eq. 5.28. Numerical evaluation of

Eq. 5.27 shows that for $|\mathbf{x}_m| \rightarrow 1$ and $\angle \mathbf{x}_m = 0$ (it will be shown later that $\angle \mathbf{x}_m = 0$ for the initial condition of Eq. 5.5), Eq. 5.27 approaches 1 if the final exponential term is not included, and it approaces a number close to 1 if this term is included. For example, if $M = 1$ and $\text{CNR}_{\text{det}} = 10.0$, then Eq. 5.27 approaches 0.85 for $|\mathbf{x}_m| \rightarrow 1$ if the final exponential term is included. The discrepancy between the two formulas is even smaller for values of $|\mathbf{x}_m|$ smaller than 1. Furthermore, M must be *at least* 1, and CNR_{det} should be *at least* 10.0 to give useful phase measurements. For larger values of M and/or CNR_{det} the discrepancy between the two formulas is even smaller than it is for $M = 1$ and $\text{CNR}_{\text{det}} = 10.0$. Thus, it seems to be a reasonable approximation to use Eq. 5.24 for all pairs of points $\vec{\rho}_1$ and $\vec{\rho}_2$ because N is large compared to $(d/\rho_0)^2$, and the larger M and CNR_{det} are, the better this approximation becomes.

The correlation function of the received speckle pattern can be found from Eq. 5.7 to be

$$\begin{aligned}\langle \zeta_R^0\left(\vec{\rho}_1; k_m, t + \frac{2L}{c}\right) \zeta_R^{0*}\left(\vec{\rho}_2; k_m, t + \frac{2L}{c}\right)\rangle = \\ \int d\vec{\rho}\,' \, \langle |\xi_t(\vec{\rho}\,'; k_m, t + L/c)|^2\rangle e^{-4\rho'^2/d_T^2} \, e^{-\frac{2}{N}\left(\frac{d\rho'}{\lambda_m L}\right)^2} e^{-i\frac{k_m}{L}\vec{\rho}\,'\cdot(\vec{\rho}_1 - \vec{\rho}_2)}.\end{aligned} \qquad (5.29)$$

Now Eqs. 5.24, 5.27, and 5.29 with their accompanying definitions constitute the iteration equations, i.e., the equations which give the spatial correlation functions of the transmitted and received waves and the mean illuminator beam intensity for each iteration. The initial condition, according to Eqs. 5.5, 5.17, and 2.8, is

$$\langle e^{-i\tilde{\phi}_{sp}(\vec{\rho}_1;t)} e^{i\tilde{\phi}_{sp}(\vec{\rho}_2;t)}\rangle = \exp\left(-\frac{1}{2}(|\vec{\rho}_1 - \vec{\rho}_2|/\rho_0)^{\frac{5}{3}}\right), \quad \text{for } t_0 \le t < t_0 + \frac{2L}{c}, \qquad (5.30)$$

where turbulence amplitude fluctuations have been neglected. This initial condition, together with the iteration equations, give the spot distribution on target, $\langle |\xi_t(\vec{\rho}\,'; k_m, t)|^2\rangle$, for each iteration.

The form of the initial condition of Eq. 5.30 leads to great simplifications in the iteration equations, Eqs. 5.24, 5.27, and 5.29. In particular, the fact that

$\langle \exp(-i\bar{\phi}_{sp}(\vec{\rho}_1; t_0)) \cdot \exp(i\bar{\phi}_{sp}(\vec{\rho}_2; t_0)) \rangle$ is real, positive, and a function of $|\vec{\rho}_1 - \vec{\rho}_2|$ implies, through Eq. 5.24, that $\langle |\xi_t(\vec{\rho}\,'; k_m, t_0 + L/c)|^2 \rangle$ is a function of $|\vec{\rho}\,'|$. Because $\langle |\xi_t(\vec{\rho}\,'; k_m, t_0 + L/c)|^2 \rangle$ is a function of $|\vec{\rho}\,'|$, it follows that $\langle \zeta_R^0(\vec{\rho}_1; k_m, t_0 + 2L/c) \cdot \zeta_R^{0*}(\vec{\rho}_2; k_m, t_0 + 2L/c) \rangle$ is real and a function of $|\vec{\rho}_1 - \vec{\rho}_2|$. Furthermore, substituting Eq. 5.24 into Eq. 5.29 shows that since $\langle \exp(-i\bar{\phi}_{sp}(\vec{\rho}_1; t_0)) \cdot \exp(i\bar{\phi}_{sp}(\vec{\rho}_2; t_0)) \rangle$ is positive, it follows that $\langle \zeta_R^0(\vec{\rho}_1; k_m, t_0 + 2L/c) \cdot \zeta_R^{0*}(\vec{\rho}_2; k_m, t_0 + 2L/c) \rangle$ is also positive. Since $\langle \zeta_R^0(\vec{\rho}_1; k_m, t_0 + 2L/c) \cdot \zeta_R^{0*}(\vec{\rho}_2; k_m, t_0 + 2L/c) \rangle$ is real, positive, and a function of $|\vec{\rho}_1 - \vec{\rho}_2|$, it is clear from Eq. 5.28 that $\mathbf{x}_m(\vec{\rho}_1, \vec{\rho}_2; t_0 + 2L/c)$ is real, positive, and a function of $|\vec{\rho}_1 - \vec{\rho}_2|$. Because $\mathbf{x}_m(\vec{\rho}_1, \vec{\rho}_2; t_0 + 2L/c)$ is a function of $|\vec{\rho}_1 - \vec{\rho}_2|$, it follows from Eq. 5.27 that $\langle \exp(-i\bar{\phi}_{sp}(\vec{\rho}_1; t_0 + 2L/c)) \cdot \exp(i\bar{\phi}_{sp}(\vec{\rho}_2; t_0 + 2L/c)) \rangle$ is also a function of $|\vec{\rho}_1 - \vec{\rho}_2|$. Because $\mathbf{x}_m(\vec{\rho}_1, \vec{\rho}_2; t_0 + 2L/c)$ is real and positive, its angle is zero, and therefore the symmetry of the integrand of Eq. 5.27 implies that $\langle \exp(-i\bar{\phi}_{sp}(\vec{\rho}_1; t_0 + 2L/c)) \cdot \exp(i\bar{\phi}_{sp}(\vec{\rho}_2; t_0 + 2L/c)) \rangle$ is real. Furthermore, numerical evaluations of Eq. 5.27 have shown that when $\angle \mathbf{x}_m = 0$, and when M is an integer greater than or equal to 1, then $\langle \exp(-i\bar{\phi}_{sp}(\vec{\rho}_1; t_0 + 2L/c)) \cdot \exp(i\bar{\phi}_{sp}(\vec{\rho}_2; t_0 + 2L/c)) \rangle$ is positive for $|\mathbf{x}_m(\vec{\rho}_1, \vec{\rho}_2; t_0 + 2L/c)|$ between 0 and 1, the range of values which the latter may take on. Thus, the argument above shows that if $\langle \exp(-i\bar{\phi}_{sp}(\vec{\rho}_1; t_0)) \cdot \exp(i\bar{\phi}_{sp}(\vec{\rho}_2; t_0)) \rangle$ is real, positive, and a function of $|\vec{\rho}_1 - \vec{\rho}_2|$, then $\langle \exp(-i\bar{\phi}_{sp}(\vec{\rho}_1; t_0 + 2L/c)) \cdot \exp(i\bar{\phi}_{sp}(\vec{\rho}_2; t_0 + 2L/c)) \rangle$ has these same properties. Therefore, since the initial condition of Eq. 5.30 applies for all times t such that $t_0 \leq t < t_0 + 2L/c$, it follows by induction that all of the functional properties mentioned in this paragraph apply for all times t such that $t \geq t_0$.

The functional properties derived in the preceding paragraph can now be used to simplify the iteration equations. Since $\langle \exp(-i\bar{\phi}_{sp}(\vec{\rho}_1; t)) \cdot \exp(i\bar{\phi}_{sp}(\vec{\rho}_2; t)) \rangle$ is a function of $|\vec{\rho}_1 - \vec{\rho}_2|$, the following definition can be used to simplify the notation:

$$C_{sp}(|\vec{\rho}_1 - \vec{\rho}_2|/d; t) \equiv \langle e^{-i\bar{\phi}_{sp}(\vec{\rho}_1; t)} e^{i\bar{\phi}_{sp}(\vec{\rho}_2; t)} \rangle. \tag{5.31}$$

Substituting this definition into Eq. 5.24 leads to the following expression for the mean illuminator beam intensity:

$$\begin{aligned}\langle|\xi_t(\vec{\rho}\,';k_m,t+L/c)|^2\rangle &= e^{-\alpha L}\left(\frac{d}{\lambda_m L}\right)^2 e^{-\frac{2}{N}\left(\frac{d\rho'}{\lambda_m L}\right)^2}\cdot\\ &\quad\cdot\int d\vec{u}\,e^{-4u^2}C_{sp}(u;t)e^{-i2\pi\left(\frac{d\vec{\rho}\,'}{\lambda_m L}\right)\cdot\vec{u}}. \end{aligned} \tag{5.32}$$

Equation 5.27 for $C_{sp}(|\vec{\rho}_1-\vec{\rho}_2|/d;t)$ can be simplified by noting that $\angle \mathrm{x}_m(\vec{\rho}_1,\vec{\rho}_2;t+2L/c) = 0$. Performing the change of variables $\alpha = (\theta_1+\theta_2)/2$, $\beta = \theta_1-\theta_2$ and carrying out the α integral shows, by symmetry of the β integrand, that only the real part of the term $e^{-i\beta/M}$ contributes to the integral. Eq. 5.27 then becomes

$$\begin{aligned}&C_{sp}\left(\frac{|\vec{\rho}_1-\vec{\rho}_2|}{d};t+\frac{2L}{c}\right) =\\ &\prod_{m=1}^{M} 2\frac{1-|\mathrm{x}_m|^2}{\pi^2}\int_0^{2\pi}d\beta\int_0^{\infty}du_1\int_0^{\infty}du_2\,u_1u_2\cdot\\ &\exp\Big(-(u_1^2+u_2^2-2|\mathrm{x}_m|u_1u_2\cos\beta)\Big)\,(2\pi-\beta)\cos(\beta/M)\cdot\\ &\exp\left(-\frac{1}{4M^2\mathrm{CNR}_{\mathrm{det}}(m,t+\frac{2L}{c})}\cdot\frac{1}{1-|\mathrm{x}_m|^2}\cdot\left(\frac{1}{u_1^2}+\frac{1}{u_2^2}\right)\right).\end{aligned} \tag{5.33}$$

The integral of Eq. 5.33 can be further simplified by making the change of variables $w = 2u_1u_2$, $c = u_1/u_2$. The c integral can be evaluated by using [54]

$$\int_0^{\infty}dx\,\frac{1}{x}\,e^{-A(x+1/x)} = 2K_0(2A),\quad \mathrm{Re}(A)>0, \tag{5.34}$$

where K_0 is the zeroth-order modified Bessel function of the second kind. Carrying out the c integral gives, finally,

$$C_{sp}\left(\frac{|\vec{\rho}_1-\vec{\rho}_2|}{d};t+\frac{2L}{c}\right) = \prod_{m=1}^{M}F_M\left(\left|\mathrm{x}_m\left(\vec{\rho}_1,\vec{\rho}_2;t+\frac{2L}{c}\right)\right|,\mathrm{CNR}_{\mathrm{det}}\left(m,t+\frac{2L}{c}\right)\right), \tag{5.35}$$

where

$$\begin{aligned}F_M(x,y) &\equiv \frac{1-x^2}{\pi}\int_0^{2\pi}d\beta\int_0^{\infty}dw\,w\,e^{xw\cos\beta}(1-\frac{\beta}{2\pi})\cos\left(\frac{\beta}{M}\right)\cdot\\ &\quad K_0\left(w+\frac{1}{M^2y}\frac{1}{1-x^2}\frac{1}{w}\right).\end{aligned} \tag{5.36}$$

The spatial correlation function of $\zeta_R^0(\vec{\rho}; k, t + 2L/c)$ can be found in terms of $C_{sp}(|\vec{\rho}_1 - \vec{\rho}_2|/d; t)$ by substituting Eq. 5.32 into Eq. 5.29. The result is

$$\left\langle \zeta_R^0\left(\vec{\rho}_1; k_m, t + \frac{2L}{c}\right) \zeta_R^{0*}\left(\vec{\rho}_2; k_m, t + \frac{2L}{c}\right)\right\rangle = \\ e^{-2\alpha L} \frac{\rho}{L^2} \frac{N_{eff}}{4d^2} \int d\vec{\rho}\, e^{-4\rho^2/d^2} e^{-\pi^2 N_{eff} |\vec{\rho}_1 - \vec{\rho}_2 + \vec{\rho}|^2/(4d^2)} C_{sp}\left(\frac{\rho}{d}; t\right), \tag{5.37}$$

where

$$\frac{1}{N_{eff}} \equiv \frac{1}{N} + \left(\frac{\lambda_m L}{d d_T}\right)^2. \tag{5.38}$$

The parameter N_{eff} represents the amount of power and information loss that occurs due to finite spatial bandwidths in the system. Since the spatial dependence of the correlation function of Eq. 5.37 is on $|\vec{\rho}_1 - \vec{\rho}_2|$, it is convenient to introduce the following definition:

$$C_R\left(\frac{|\vec{\rho}_1 - \vec{\rho}_2|}{d}; k_m, t\right) \equiv \frac{\langle \zeta_R^0(\vec{\rho}_1; k_m, t) \zeta_R^{0*}(\vec{\rho}_2; k_m, t)\rangle}{\langle |\zeta_R^0(\vec{\rho}; k_m, t)|^2\rangle}, \tag{5.39}$$

which can be evaluated using Eq. 5.37 to be

$$C_R\left(\frac{|\vec{\rho}_1 - \vec{\rho}_2|}{d}; k_m, t + \frac{2L}{c}\right) = \\ \frac{\int d\vec{u}_0\, e^{-4u_0^2} e^{-\pi^2 N_{eff} |(\vec{\rho}_1 - \vec{\rho}_2)/d + \vec{u}_0|^2/4}\, C_{sp}(u_0; t)}{\int d\vec{u}_0\, e^{-4u_0^2} e^{-\pi^2 N_{eff} u_0^2/4}\, C_{sp}(u_0; t)}. \tag{5.40}$$

Note that

$$\mathbf{x}_m\left(\vec{\rho}_1, \vec{\rho}_2; t + \frac{2L}{c}\right) \equiv C_R\left(\frac{|\vec{\rho}_1 - \vec{\rho}_2|}{d}; k_m, t + \frac{2L}{c}\right). \tag{5.41}$$

The carrier-to-noise ratio per detector per wavelength can be evaluated using Eqs. 5.16 and 5.37, and is found to be

$$\begin{aligned} \mathrm{CNR}_{\mathrm{det}}\left(m, t + \frac{2L}{c}\right) &= \frac{\eta P_T \epsilon_{opt}}{h\nu_0 B} \frac{\pi d^2}{4N} \mathrm{e}^{-2\alpha L} \frac{\rho}{4L^2} N_{eff} \cdot \\ &\quad \int d\vec{u}\, e^{-4u^2} e^{-\pi^2 N_{eff} u^2/4}\, C_{sp}(u; t). \end{aligned} \tag{5.42}$$

At this point the expressions and notations for the iteration equations have been simplified, and are summarized in Table 5.2. The equations of Table 5.2 can

<table>
<tr><th>Function</th><th></th><th>Formula</th></tr>
<tr><td>$C_{sp}(u;t)$</td><td>$=$</td><td>$e^{-\frac{1}{2}(du/\rho_0)^{5/3}}$ for $t_0 \le t < t_0 + \frac{2L}{c}$</td></tr>
<tr><td colspan="3">Initial condition; correlation function of speckle component of applied phase correction</td></tr>
<tr><td>$C_R\left(u;k_m,t+\frac{2L}{c}\right)$</td><td>$=$</td><td>$[\int d\vec{u}_0\, e^{-4u_0^2}\, e^{-\pi^2 N_{eff}|\vec{u}+\vec{u}_0|^2/4}\, C_{sp}(u_0;t)]/$
$[\int d\vec{u}_0\, e^{-4u_0^2}\, e^{-\pi^2 N_{eff} u_0^2/4}\, C_{sp}(u_0;t)]$</td></tr>
<tr><td colspan="3">Normalized correlation function of received speckle field</td></tr>
<tr><td>$\mathrm{CNR}_{\mathrm{det}}\left(m,t+\frac{2L}{c}\right)$</td><td>$=$</td><td>$\frac{\eta P_T \epsilon_{opt}}{h\nu_0 B}\frac{\pi d^2}{4N}e^{-2\alpha L}\frac{\rho}{4L^2}N_{eff}\cdot$
$\int d\vec{u}\, e^{-4u^2}\, e^{-\pi^2 N_{eff} u^2/4}\, C_{sp}(u;t)$</td></tr>
<tr><td colspan="3">Phase-measurement carrier-to-noise ratio per detector per wavelength</td></tr>
<tr><td>$C_{sp}\left(u;t+\frac{2L}{c}\right)$</td><td>$=$</td><td>$\prod_{m=1}^{M} F_M\left(C_R\left(u;k_m,t+\frac{2L}{c}\right), \mathrm{CNR}_{\mathrm{det}}\left(m,t+\frac{2L}{c}\right)\right)$</td></tr>
<tr><td colspan="3">Correlation function of speckle component of appled phase correction</td></tr>
</table>

Table 5.2: System Iteration Equations

be used to find the state of the system—i.e. $C_{sp}(u;t)$, $C_R(u;k_m,t+2L/c)$, and $\mathrm{CNR}_{\mathrm{det}}(m,t+2L/c)$—at any time after t_0, and Eq. 5.32 gives the mean illuminator beam intensity at any time after t_0. These equations depend on four parameters: d/ρ_0 (for the initial condition), $\mathrm{CNR}_{\mathrm{det}}$, M, and N_{eff}. A steady state equation can be found by substituting the second and third equations of Table 5.2 into the fourth one, and setting the temporal argument of the left hand side of the fourth equation to t. This steady state equation is clearly difficult to solve in the general case, although a numerical solution can easily be obtained for the case in which $N_{\mathit{eff}} \to \infty$ and $\mathrm{CNR}_{\mathrm{det}} \to \infty$. The steady state for finite values of N_{eff}, $\mathrm{CNR}_{\mathrm{det}}$, and M can be found approximately by cycling through the iteration equations of Table 5.2—i.e. evaluating $C_{sp}(u;t)$ for $t = t_0 + 2L/c, t_0 + 4L/c, t_0 + 6L/c, \ldots$—until the state changes very little. The next section describes the use of this procedure to find the steady state.

5.3 Numerical Evaluation of Iteration Equations

In the numerical evaluation of the iteration equations, two approximations are made. The first approximation is that $\mathrm{CNR}_{\mathrm{det}}$ is assumed to be constant for all iterations, independent of t as well as of m. Thus, the expression used for $\mathrm{CNR}_{\mathrm{det}}$ is

$$\mathrm{CNR}_{\mathrm{det}} = \frac{\eta P_T}{h\nu_0 B}\frac{\pi d^2}{4N}\left[\frac{\rho}{\pi L^2}e^{-2\alpha L}\epsilon\right]\epsilon_{opt}, \tag{5.43}$$

where the term in brackets is equal to $\langle|\zeta_R^0(\vec{\rho};k_m,t)|^2\rangle$, and ϵ is the reduction factor in this intensity due to the finiteness of N_{eff}, i.e. due to the finite target size and the finite detector and corrector element size. This reduction factor is given by

$$\epsilon = \frac{\pi}{4}N_{\mathit{eff}}\int d\vec{u}\, e^{-4u^2}\, e^{-\pi^2 N_{\mathit{eff}} u^2/4}\, C_{sp}(u;t), \tag{5.44}$$

which approaches 1 as $N_{\mathit{eff}} \to \infty$, since $C_{sp}(0;t) = 1$ by definition. This loss factor was actually evaluated in each iteration in order to check the validity of this approximation, and it showed little variation after five iterations for the values of N_{eff} used. The second approximation is that functions which depend on k_m are evaluated at k_{av}. Thus, although N_{eff} has a different value for each of the wavelengths used, it is assumed to have a fixed value which is obtained by setting the wavelength equal to $2\pi/k_{av}$. Also, the fourth equation of Table 5.2 is approximated by

$$C_{sp}\left(u; t + \frac{2L}{c}\right) \approx \left[F_M\left(C_R\left(u; k_{av}, t + \frac{2L}{c}\right), \mathrm{CNR_{det}}\right)\right]^M, \qquad (5.45)$$

i.e. the product from $m = 1$ to M is replaced by raising the argument of the product to the Mth power, with k_m replaced by k_{av} in each term. This approximation can be justified by noting that the relative separation among the transmitted wavelengths is small. Recall from the discussion connected with Table 5.1 that $|k_M - k_1|/k_{av} \leq 0.048$ (with equality for $M = 4$), so the relative separation among the wavelengths is in fact small.

Using the equations of Table 5.2 together with the approximations mentioned above, the steady state can be conveniently evaluated as a function of d/ρ_0 (for the initial condition), $\mathrm{CNR_{det}}$, M, and N_{eff}. At this point, the steady state can be most simply described in terms of the mean illuminator beam intensity. A comparison of this intensity distribution with the no-turbulence distribution will give a measure of the quality of wavefront correction that this system can achieve in steady state.

In order to obtain useful results for the mean illuminator beam intensity, we must find realistic values for the four parameters mentioned above. The first parameter to consider is d/ρ_0, the initial condition. The analysis of Chapter 3 shows that the performance of a coherent laser radar is significantly degraded by turbulence when d/ρ_0 is large compared to 1. Thus, an adaptive system would be used to compensate the turbulence-induced wavefront distortions when d/ρ_0 is close to 10 or larger. Figures 5.3a and 5.3b show the value of θ needed to give $\rho_0 = d/10$ for the daytime and nighttime C_n^2 profiles of Figure 2.2. Note that $\rho_0(\theta) = \rho_0(\theta = 0)(\cos\theta)^{3/5}$ where

parameter	definition	value
η	quantum efficiency	0.5
P_T	transmitter power	100 W
B	IF bandwidth	10 kHz
$\epsilon_{total} \equiv \epsilon \cdot \epsilon_{opt}$	total system loss	0.05
ρ	target reflectivity	0.1
$e^{-2\alpha L}$	atmospheric loss	0.5 for vertical path

Table 5.3: System Parameter Values

$\rho_0(\theta)$ and $\rho_0(\theta = 0)$ are both for propagation to the same altitude.[1] At a wavelength of 10.6 μm, either the aperture diameter or the zenith angle must be rather large in order for wavefront correction to be necessary. At a wavelength of 5 μm, the turbulence effects are more severe, so that wavefront correction would be necessary for smaller apertures and zenith angles. Thus, Figures 5.3a and 5.3b show under what conditions wavefront correction would be useful.

The second parameter is $\mathrm{CNR}_{\mathrm{det}}$, the CNR per detector per wavelength, given by Eq. 5.43. This parameter tells how well the phase of the received wave can be measured. As shown in the Appendix, the linearization we have done of the phase of the IF signal is valid when $\mathrm{CNR}_{\mathrm{det}}$ is 10 or larger. Thus, we shall take $\mathrm{CNR}_{\mathrm{det}} \geq 10$ to be the condition under which the multiwavelength adaptive system described here would be able to operate effectively. In order to determine the parameter values for which this condition is met, we shall assume the parameter values listed in Table 5.3, and examine the dependence of $\mathrm{CNR}_{\mathrm{det}}$ on the remaining, as yet unspecified, parameter values. Note that the IF bandwidth B must be at least as large as the temporal bandwidth of the turbulence fluctuations, which is of the order of v_w/ρ_0, where v_w is the component of the wind velocity perpendicular to the propagation path.

In evaluating Eq. 5.43 for CNR_{det}, we use $N = 4(d/\rho_0)^2$, since N must be at

---

[1] ρ_0 varies very slightly with altitude for altitudes between 100 and 1000 km, the range of altitudes considered here.

least this large in order to adequately detect and correct the wavefront distortions [55]. When the parameter values of Table 5.3 are used, and when $N = 4(d/\rho_0)^2$, then $\mathrm{CNR}_{\mathrm{det}}$ is a function of λ, ρ_0, L, and θ (note that ρ_0 itself is a function λ, L, and θ, as well as of the $C_n^2(\eta)$ profile). Figures 5.4a and 5.4b show the maximum target altitude for which $\mathrm{CNR}_{\mathrm{det}} = 10$ as a function of θ, for wavelengths of 10.6 and 5 μm. They also show the minimum altitude, 100 km, below which assumptions used in this analysis may not be valid. Thus, assuming that the target altitude is at least 100 km, Figures 5.4a and 5.4b show under what conditions the target return is strong enough for its phase to be measured over each detector at each wavelength—i.e. under what conditions this system would be able to operate—for the parameter values assumed here. The difference in maximum altitude for the two wavelengths is due to two effects. First, the shot noise variance is larger at shorter wavelengths, so that a stronger target return is necessary in order to give the same carrier-to-noise ratio. Second, at shorter wavelengths, the turbulence coherence length is shorter, so that for a given aperture diameter, more detectors are required to measure the wavefront distortions. Therefore, the target return must be stronger in order to provide the same amount of target return power per detector. Thus, at shorter wavelengths, the target must be closer to the radar in order to be able to use this system. From Figures 5.3a, 5.3b, 5.4a, and 5.4b, it can be seen that at a wavelength of 10.6 μm, this system would be useful for aperture diameters of at least 3 m and for target altitudes of several hundred km. At a wavelength of 5 μm, this system would be useful for aperture diameters of at least 2 m and for target altitudes of only a few hundred km. Note that the plots of Figures 5.4a and 5.4b assume that the transmitted power per wavelength is 100 Watts (see Table 5.3). If this power is larger, then the maximum target altitudes will be larger.

The third parameter is M, the number of transmitted wavelengths. The mean illuminator beam intensity is evaluated for $M = 2$ and for $M = 4$, since these are the smallest and largest values possible for this technique of turbulence and speckle separation. The mean illuminator beam intensity is also evaluated for $M = 1$, in order to quantitatively confirm the performance prediction for this limiting case, which was discussed in the beginning of Section 5.2.

The fourth parameter is N_{eff}, which represents the power and information loss due to finite spatial bandwidths (the larger N_{eff}, the lower the loss), and which is defined in Eq. 5.38. The paramter N_{eff} depends on five parameters: N, λ, L, d, and d_T. The behavior of N_{eff} can be more simply examined by assuming that $\mathrm{CNR}_{\mathrm{det}} = 10.0$ with the parameter values of Table 5.3, and by continuing to assume that $N = 4(d/\rho_0)^2$. When these assumptions are made, N_{eff} becomes a function of d/ρ_0, λ, and d_T.

In Figures 5.5a and 5.5b, N_{eff} is plotted as a function of d_T for various values of d/ρ_0, for $\lambda = 10.6\,\mu$m and $\lambda = 5\,\mu$m, respectively. In these plots, $\theta = 45°$. For a different value of θ, ρ_0 would be different. Also, the atmospheric loss is approximated as $e^{-2\alpha L/\cos\theta}$ for slant-path propagation at zenith angle θ, so the dependence of $\mathrm{CNR}_{\mathrm{det}}$ on λ, L, and ρ_0 changes with changing θ. Figure 5.5a shows N_{eff} for $\lambda = 10.6\,\mu$m. The assumed parameter values, and the assumptions that $\mathrm{CNR}_{\mathrm{det}} = 10.0$ and $N = 4(d/\rho_0)^2$, imply that L=890 km and ρ_0=0.50 m (for the daytime $C_n^2(\eta)$ profile of Figure 2.2) for the $10.6\,\mu$m wavelength. Thus, N_{eff} is plotted only for $d_T \geq 20$ m, because for smaller values of d_T, the target is unresolved by the turbulence-limited spot size. Figure 5.5a shows that at the $10.6\,\mu$m wavelength, N_{eff} is a few hundred for the parameters values assumed here. If L is smaller than 890 km, so that $\mathrm{CNR}_{\mathrm{det}} > 10.0$, then N_{eff} would be even larger. Figure 5.5b shows N_{eff} for $\lambda = 5\,\mu$m. In this case, the assumed parameter values and the assumptions concerning $\mathrm{CNR}_{\mathrm{det}}$ and N imply that L=240 km and ρ_0=0.20 m, for the daytime $C_n^2(\eta)$ profile of Figure 2.2. Thus, N_{eff} is plotted only for $d_T \geq 8$ m, because for smaller values of d_T, the target is unresolved by the turbulence-limited spot size.

Figure 5.5a shows that at the $5\,\mu m$ wavelength, N_{eff} is several hundred for the parameters values assumed here. If L is smaller than 240 km, so that $\mathrm{CNR_{det}} > 10.0$, then N_{eff} can be as large as 1000 or more.

Now that we have discussed the range of values which d/ρ_0, $\mathrm{CNR_{det}}$, M, and N_{eff} may be expected to assume, the remaining question to be answered before evaluating the steady-state mean illuminator beam intensity is: after how many iterations does the system reach steady state. To answer this question, the 0.5 and 0.1 spot radii of the illuminator beam pattern were found in each iteration for ten iterations, for $\mathrm{CNR_{det}} = 10.0$, $M = 2$, $N_{eff} = 2000$, and d/ρ_0=5.0, 10.0, and 20.0. These attenuation radii are plotted in Figures 5.6a, 5.6b, and 5.6c as a function of the iteration number. For all three values of d/ρ_0, the initial condition, the spot radii converged to the same values--the relative difference in the spot radii after ten iterations for the different values of d/ρ_0 is less than 0.4 percent. The rate of convergence is slower for smaller values of d/ρ_0, but even for d/ρ_0=5.0 the system converges to steady state after about six iterations. The rate of convergence may be different for different values of $\mathrm{CNR_{det}}$, M, and N_{eff}. However, numerical evaluation of ϵ (see Eq. 5.44) in each iteration has shown that ϵ varies little after five iteations for all values of $\mathrm{CNR_{det}}$, M, and N_{eff} for which the performance has been evaluated, except for cases in which $M = 1$. Thus, the radar performance at the end of ten iterations can safely be regarded as the steady-state performance for $M > 1$ and the values of $\mathrm{CNR_{det}}$ and N_{eff} used here.

For $M = 1$ there is no speckle averaging, so it does not seem that the spot size on target will decrease from one iteration to the next. In fact, numerical evaluations have shown that the spot size increases in each iteration for at least the first few iterations. This increase occurs because of the particular form of the correlation function of the transmitted speckle distortion as compared to that of the turbulence distortion, i.e. the transmitted distortion in the absence of wavefront correction. Thus, the spot size on target is larger in the second iteration than it is in the first. Therefore, the coherence length of the speckle component of the applied phase correction is smaller in the third iteration than in the second, and so on. However, the spot size on target cannot increase indefinitely, for two reasons. First, the correction elements and detectors have a finite size, which limits the spot size on target. Second, the target size is finite, so that if the spot size on target is so large that it fills the target, then the coherence length of the received speckle pattern will remain constant for the remaining iterations, and therefore the coherence length of the transmitted speckle phase will also remain constant. Thus, if the spot size keeps increasing until it fills the target, then at *that* time the system will have reached steady state.

It would be interesting to know whether, for $M = 1$, the system may reach steady state before the spot fills the target. That is, although the spot size increases in each iteration, it may be possible that the rate of increase slows down enough that the system reaches steady state before the spot fills the target. To address this question, the spot distributions were evaluated for 20 iterations, for $d/\rho_0 = 10.0$, $\text{CNR}_{\text{det}} = 10.0$, $M = 1$, and $N_{eff} = \infty$. The reason they were evaluated for $N_{eff} = \infty$ is that in this case there are no finite spatial bandwidths, i.e. finite correction element and detector size or finite target size, that would force the system to reach steady state as described above. Thus, if the system reaches steady state in this case, it shows that the system may reach steady state through some mechanism other than the limitation in spot size imposed by finite spatial bandwidths. The 0.5 and 0.1 spot radii for this case are plotted in Figure 5.7. They do not show any leveling off after six iterations. In fact, examination of the iteration equations shows that for $M = 1$ and $N_{eff} = \infty$, $C_{sp}(u;t) \rightarrow 0$ as $t \rightarrow \infty$ for all u, except that $C_{sp}(0;t) = 1$ for all t. Thus, it is clear that in this case the spot distribution becomes wider in each iteration[2], and the system has no steady state. Therefore, it seems that the steady state for $M = 1$ is always the state in which the spot fills the target.

Now the steady-state (for $M > 1$) mean illuminator beam intensity may be evaluated for parameter values of interest. Figures 5.8 and 5.9 show the 0.5 and 0.1 spot radii (respectively) of the mean illuminator beam intensity after ten iterations for $\mathrm{CNR}_{\mathrm{det}} = 10.0$ as a function of N_{eff} for $M = 1$, 2, and 4. They also show the spot radii of an uncorrected beam for $d/\rho_0 = 10.0$. Note that these results do not necessarily assume the parameter values of Table 5.3. For the initial condition, $d/\rho_0 = 10.0$ was used. However, the results given here for $M > 1$ do not depend on the initial condition, since the system has reached steady state.

For $M = 1$, the results given are those obtained at the end of ten iterations. In the case of $M = 1$, the spot radii are even larger than the no-correction results because of the lack of speckle averaging, as discussed earlier. Note that these results for the $M = 1$ spot radii are valid only if these radii are smaller than the target size. This condition is met for the data presented here, for the following reason. We are assuming that the target is spatially resolved by the turbulence-limited spot size. Therefore, $\lambda L/\rho_0 < d_T$, so that $(d/\rho_0)(\lambda L/d) < d_T$. Since these $M = 1$ results are for $d/\rho_0 = 10.0$, it follows that $10\lambda L/d < d_T$. The diffraction-limited 0.5 and 0.1 spot radii are $0.53\lambda L/d$ and $0.97\lambda L/d$ respectively, so that the normalized spot radii plotted in in Figures 5.8 and 5.9 for $M = 1$ are all less than $6\lambda L/d$, which is clearly less than d_T for d/ρ_0=10.0.

For $M = 2$ and $M = 4$, the steady-state 0.5 spot radius is less than 1.2 times diffraction-limited for N_{eff} between 200 and 2000, and the steady-state 0.1 spot radius is less than 1.5 times diffraction-limited for N_{eff} between 200 and 2000. The

---

[2] Note that if $d_T > \rho_0'$, then when the spot on target becomes larger than ρ_0', the SCA approximation is violated, so that the performance may be even worse than that predicted by this analysis.

larger M is, the smaller the spot size is, because the residual speckle component of the wavefront correction is smaller. The spot size depends very weakly on N_{eff} in these plots, because it is assumed that N is large enough for the turbulence distortions to be perfectly corrected. Therefore, the size of a correction element is small compared to ρ_0, so that it is also small compared to the speckle coherence length (for $M > 1$). Thus, increasing N further has little effect on the radar performance as long as CNR_{det} is held fixed. Furthermore, it is assumed that the target is spatially resolved by the turbulence-limited spot size. Therefore, the target is always spatially resolved for $M > 1$, so that increasing $(dd_T/(\lambda L))^2$ further has little effect on the radar performance.

The results illustrated in Figures 5.8 and 5.9 show that in steady state, the wavefront correction for $M > 1$ is close enough to the perfect turbulence phase correction of Chapter 4, that the width of the mean illuminator beam intensity distribution is close to what it would be in the absence of turbulence. This fact indicates that the spatial resolution in steady state for $M > 1$ will be close to the no-turbulence performance, as is seen in the following section.

5.4 Performance of Multiwavelength Radar System

In this section the spatial resolution and CNR are derived for the multiwavelength radar system shown in Figure 5.1. An approximation for the range and velocity accuracy is also given. The formulas derived can be used to evaluate the steady state radar performance.

5.4.1 Spatial Resolution

The spatial resolution can be found, as was done in Section 3.1, by expressing the mean target-return power in terms of a spatial overlap integral in the target plane. The target-return component of the IF signal can be expressed in terms of a target-plane integral by substituting Eq. 5.7 into Eq. 5.23, with the following result:

$$\begin{aligned}\ell_{\text{radar}}\left(t+\frac{2L}{c}\right) &= \sqrt{P_T\epsilon_{opt}}\sum_{m=1}^{M} e^{i(4\pi v_{\parallel}/\lambda_m)t}\,\cdot \\ &\quad \int d\vec{\rho}\,'\,\xi_t\left(\vec{\rho}\,';k_m,t+\frac{L}{c}\right)\cdot \\ &\quad \mathbf{T}\left(\vec{\rho}\,';k_m,t+\frac{L}{c}\right)\zeta_{lo}^{*}\left(\vec{\rho}\,';k_m,t+\frac{L}{c}\right), \qquad (5.46)\end{aligned}$$

where $\zeta_{lo}^{*}(\vec{\rho}\,';k_m,t+L/c)$ is the spatially back-propagated corrected LO beam pattern, and is given by

$$\begin{aligned}\zeta_{lo}^{*}\left(\vec{\rho}\,';k_m,t+\frac{L}{c}\right) &= e^{-\alpha L/2}\int_R d\vec{\rho}\,\xi_{LO}^{*}(\vec{\rho})e^{-i\check{\phi}_{sp}(\vec{\rho};t+2L/c)}\,\cdot \\ &\quad \frac{e^{ik_mL}}{i\lambda_m L}e^{i\frac{k_m}{2L}\rho'^2}\int d\vec{\rho}_1\,h(\vec{\rho}-\vec{\rho}_1)e^{-i\frac{k_m}{L}\vec{\rho}_1\cdot\vec{\rho}\,'}. \qquad (5.47)\end{aligned}$$

The mean target-return power at time $t+2L/c$ is $\langle|\ell_{\text{radar}}(t+2L/c)|^2\rangle$, and is found from Eq. 5.46 to be

$$\begin{aligned}\left\langle\left|\ell_{\text{radar}}\left(t+\frac{2L}{c}\right)\right|^2\right\rangle &= P_T\epsilon_{opt}\sum_{m=1}^{M}\sum_{m'=1}^{M} e^{i4\pi v_{\parallel}(1/\lambda_m-1/\lambda_{m'})t}\,\cdot \\ &\quad \langle\int d\vec{\rho}_1{}'\int d\vec{\rho}_2{}'\,\xi_t\left(\vec{\rho}_1{}';k_m,t+\frac{L}{c}\right)\xi_t^{*}\left(\vec{\rho}_2{}';k_{m'},t+\frac{L}{c}\right)\cdot \\ &\quad \mathbf{T}\left(\vec{\rho}_1{}';k_m,t+\frac{L}{c}\right)\mathbf{T}^{*}\left(\vec{\rho}_2{}';k_{m'},t+\frac{L}{c}\right)\cdot \\ &\quad \zeta_{lo}^{*}\left(\vec{\rho}_1{}';k_m,t+\frac{L}{c}\right)\zeta_{lo}\left(\vec{\rho}_2{}';k_{m'},t+\frac{L}{c}\right)\rangle. \qquad (5.48)\end{aligned}$$

In the absence of LO correction, $\xi_t(\cdot)$, $\mathbf{T}(\cdot)$, and $\zeta_{lo}^{*}(\cdot)$ would all be statistically independent of each other, so that the mean of the integrand in Eq. 5.48 could be expressed as the product of three means. However, the LO correction at time $t+2L/c$ is derived from the received wave, which is a function of both the illuminator beam pattern and the target reflectivity at time $t+L/c$. Therefore, $\zeta_{lo}^{*}(\cdot)$ is statistically dependent on both $\xi_t(\cdot)$ and $\mathbf{T}(\cdot)$, so that the mean in Eq. 5.48 cannot be evaluated simply. However, an examination of the spatial characteristics of the terms in the integrand of Eq. 5.48 leads to a simplification of this equation. In particular, both $\xi_t(\vec{\rho}\,';k_m,t+L/c)$ and $\zeta_{lo}^*(\vec{\rho}\,';k_m,t+L/c)$ cannot have spatial variations in the target plane over spatial scales smaller than about $\lambda_m L/d$, since each of them is the result of the propagation of a beam from the diameter-d radar aperture. On the other hand, $\mathbf{T}(\vec{\rho}\,';k_m,t+L/c)$ has spatial variations on scales of the order of λ_m, much shorter than the scale of variations of the target-plane beam patterns. Since $\mathbf{T}(\vec{\rho}\,';k_m,t+L/c)$ is zero-mean, it can be argued that on an instantaneous basis, if $\mathbf{T}(\vec{\rho}_1\,';k_m,t+L/c)$ and $\mathbf{T}^*(\vec{\rho}_2\,';k_m,t+L/c)$ are spatially offset from each other by more than a wavelength for $m=m'$, or if $m\neq m'$, then the uncorrelated, high spatial frequency oscillations about zero of each of these terms will cancel each other when the spatial integration over $\vec{\rho}_1$ and $\vec{\rho}_2$ is carried out. Therefore, the integral over $\vec{\rho}_1$ and $\vec{\rho}_2$ in Eq. 5.48 is close to zero at each instant unless $m=m'$, and $\mathbf{T}(\vec{\rho}_1\,';k_m,t+L/c)$ and $\mathbf{T}^*(\vec{\rho}_2\,';k_m,t+L/c)$ are separated from each other by less than λ_m. Thus, we can replace $\mathbf{T}(\vec{\rho}_1\,';k_m,t+L/c)\mathbf{T}^*(\vec{\rho}_2\,';k_m,t+L/c)$ in the integrand of Eq. 5.48 with $|\mathbf{T}(\vec{\rho}_1\,';k_m,t+L/c)|^2\lambda_{av}^2\delta(\vec{\rho}_1\,'-\vec{\rho}_2\,')\delta_{mm'}$, and therefore,

$$\left\langle\left|\ell_{\text{radar}}\left(t+\frac{2L}{c}\right)\right|^2\right\rangle \approx P_T\epsilon_{opt}\lambda_{av}^2\sum_{m=1}^{M}\int d\vec{\rho}\,'\left\langle\left|\xi_t\left(\vec{\rho}\,';k_m,t+\frac{L}{c}\right)\right|^2\cdot\right.$$
$$\left.\left|\mathbf{T}\left(\vec{\rho}\,';k_m,t+\frac{L}{c}\right)\right|^2\left|\zeta_{lo}^*\left(\vec{\rho}\,';k_m,t+\frac{L}{c}\right)\right|^2\right\rangle. \quad (5.49)$$

Equation 5.49 shows that at each instant, the region of the target illuminated by the two target-plane beam patterns is given by the size of $|\xi_t(\vec{\rho}\,';k_m,t+L/c)|^2|\zeta_{lo}^*(\vec{\rho}\,';k_m,t+L/c)|^2$. The instantaneous spatial resolution is given by the e^{-2} attenuation point of this product. Thus, the non-random spatial resolution can be defined as the e^{-2} attenuation point of the mean of this term, i.e.

$$r_{res}\left(t+\frac{2L}{c}\right)\equiv$$
$$e^{-2}\text{ attenuation point of }\left\langle\left|\xi_t\left(\vec{\rho}\,';k_m,t+\frac{L}{c}\right)\right|^2\left|\zeta_{lo}^*\left(\vec{\rho}\,';k_m,t+\frac{L}{c}\right)\right|^2\right\rangle. \quad (5.50)$$

In principle, the spatial resolution can be evaluated in each iteration using

Eq. 5.50. However, in steady state the spatial resolution can be more simply evaluated, for the following reason. Figures 5.8 and 5.9 show that for $M > 1$, the steady-state mean illuminator beam distribution is close to diffraction limited. This beam distribution is not narrower than diffraction limited at any instant. Therefore, the results shown in Figures 5.8 and 5.9 imply that the illuminator beam distribution is close to diffraction limited at every instant. Because the same correction is applied to both the transmitted and LO beam, the two target-plane beam patterns have the same statistical properties in steady state, and therefore the corrected BPLO beam distribution is also close to diffraction limited at every instant in steady state. Thus, it follows that the target-plane spot distributions do not fluctuate much in steady state, so that the e^{-2} attenuation point of the mean of the product of the target-plane beam intensities can be approximated as the e^{-2} attenuation point of the product of the mean beam intensities, using Eqs. 4.12 and 4.13.

Figure 5.10 shows the spatial resolution, evaluated at the end of ten iterations (hence presumably in the steady state), as a function of N_{eff} with $k_m \equiv 2\pi/\lambda_{av}$, for $M = 2$ and 4, and for $\text{CNR}_{\text{det}} = 10.0$. The $M = 1$ results are not the steady-state results, as discussed in Section 5.3, but they are shown for comparison with the other results. The $M = 1$ results were evaluated using the approximation mentioned in the previous paragraph. Although the argument on which this approximation is based does not apply to the $M = 1$ case, so that these $M = 1$ results are not, strictly speaking, the spatial resolution, these results still give an idea of how the spatial resolution for $M = 1$ would compare to that for $M = 2$ or $M = 4$.

The curves of Figure 5.10 are very similar to those of Figures 5.8 and 5.9, which show the spot sizes of the illuminator beam pattern. That is expected, since both target-plane beam patterns have the same statistical properties in steady state, so that both of the mean target-plane beam intensity distributions have approximately the same shape in steady state. The only difference between the two intensity distributions is due to the fact that the uncorrected transmitted beam pattern is the Gaussian beam of Eq. 3.1, whereas the uncorrected LO beam pattern is a truncated plane wave, but this leads to a spot size difference of less than 10 percent. As mentioned in connection with Figures 5.8 and 5.9, Figure 5.10 shows that the steady-state spatial resolution is close to diffraction-limited for $M > 1$, but for $M = 1$ the spatial resolution is no better than the no-correction result; in fact it is somewhat worse. The spatial resolution is essentially independent of N_{eff} for fixed values of $\mathrm{CNR}_{\mathrm{det}}$ and of M, as long as N is large enough that the turbulence distortions may be measured and corrected nearly perfectly.

5.4.2 Carrier-to-noise Ratio

The CNR at time t of the multiwavelength radar system is given (for the cw case) by $\langle|\ell_{\mathrm{radar}}(t)|^2\rangle/\langle|\mathbf{n}_{\mathrm{radar}}(t)|^2\rangle$, where $\ell_{\mathrm{radar}}(t)$ and $\mathbf{n}_{\mathrm{radar}}(t)$, the IF filtered, phase-corrected target return and shot noise, are given by Eqs. 5.23 and 5.22 respectively. The mean-squared target return can be written as

$$\begin{aligned}\langle|\ell_{\mathrm{radar}}(t)|^2\rangle \quad = \quad & P_T\epsilon_{opt}\frac{4N}{\pi d^2}\sum_{m=1}^{M}\sum_{m'=1}^{M} e^{i4\pi v_{\parallel}(1/\lambda_m-1/\lambda_{m'})t}\cdot\\ & \int_R d\vec{\rho}_1\int_R d\vec{\rho}_2\,\langle\zeta_R^0(\vec{\rho}_1;k_m,t)e^{-i\bar{\phi}_{sp}(\vec{\rho}_1;t)}\cdot\\ & \zeta_R^{0*}(\vec{\rho}_2;k_{m'},t)e^{i\bar{\phi}_{sp}(\vec{\rho}_2;t)}\rangle, \end{aligned} \tag{5.51}$$

where Eq. 5.10 has been substituted into Eq. 5.23. In Section 5.4.1, an examination of the expression for $\langle|\ell_{\mathrm{radar}}(t)|^2\rangle$ in terms of the target-plane spatial overlap integrals showed that the contributions to $\langle|\ell_{\mathrm{radar}}(t)|^2\rangle$ from terms for which $m \neq m'$ are approximately zero. Using this approximation in Eq. 5.51 gives

$$\begin{aligned}\langle|\ell_{\mathrm{radar}}(t)|^2\rangle \quad = \quad & P_T\epsilon_{opt}\frac{4N}{\pi d^2}\sum_{m=1}^{M}\int_R d\vec{\rho}_1\int_R d\vec{\rho}_2\langle\zeta_R^0(\vec{\rho}_1;k_m,t)e^{-i\bar{\phi}_{sp}(\vec{\rho}_1;t)}\cdot\\ & \zeta_R^{0*}(\vec{\rho}_2;k_m,t)e^{i\bar{\phi}_{sp}(\vec{\rho}_2;t)}\rangle. \end{aligned} \tag{5.52}$$

In order to evaluate $\langle|\ell_{\mathrm{radar}}(t)|^2\rangle$, the mean in Eq. 5.52 must be evaluated. Because the only factor which depends on shot noise in the expression to be averaged is $e^{-i\bar{\phi}_{sp}(\vec{\rho}_1;t)}e^{i\bar{\phi}_{sp}(\vec{\rho}_2;t)}$, Eq. 5.26 can be used to evaluate the mean over the shot noise fluctuations in Eq. 5.52. The result is

$$\begin{aligned}
&\langle \zeta_R^0(\vec{\rho}_1;k_m,t)e^{-i\bar{\phi}_{sp}(\vec{\rho}_1;t)}\zeta_R^{0*}(\vec{\rho}_2;k_m,t)e^{i\bar{\phi}_{sp}(\vec{\rho}_2;t)}\rangle = \\
&\quad \langle r_{1m}r_{2m}e^{i(\theta_{1m}-\theta_{2m})}\prod_{m'=1}^{M}\{\exp\left(-i\frac{1}{M}(\theta_{1m'}-\theta_{2m'})\right)\cdot \\
&\quad \exp\left(-\frac{1}{4M^2\mathrm{CNR}_{\mathrm{det}}(m',t)}\left(\frac{\langle r_{1m'}^2\rangle}{r_{1m'}^2}+\frac{\langle r_{2m'}^2\rangle}{r_{2m'}^2}\right)\right)\}\rangle,
\end{aligned} \tag{5.53}$$

where $r_{1m}e^{i\theta_{1m}} \equiv \zeta_R^0(\vec{\rho}_1;k_m,t)$ and $r_{2m}e^{i\theta_{2m}} \equiv \zeta_R^0(\vec{\rho}_2;k_m,t)$. Equation 5.53 is applicable when $\vec{\rho}_1$ and $\vec{\rho}_2$ are on different detectors. However, we make the approximation of using Eq. 5.53 for all pairs of points $\vec{\rho}_1$ and $\vec{\rho}_2$, for reasons explained in connection with Eq. 5.27. Because the received speckle field $\zeta_R^0(\vec{\rho};k_m,t)$ is statistically independent at two different values of m, Eq. 5.53 can be written as

$$\begin{aligned}
&\langle \zeta_R^0(\vec{\rho}_1;k_m,t)e^{-i\bar{\phi}_{sp}(\vec{\rho}_1;t)}\zeta_R^{0*}(\vec{\rho}_2;k_m,t)e^{i\bar{\phi}_{sp}(\vec{\rho}_2;t)}\rangle = \\
&\quad \left\langle r_{1m}r_{2m}\exp\left(i\frac{M-1}{M}(\theta_{1m}-\theta_{2m})\right)\exp\left(-\frac{1}{4M^2\mathrm{CNR}_{\mathrm{det}}(m,t)}\left(\frac{\langle r_{1m}^2\rangle}{r_{1m}^2}+\frac{\langle r_{2m}^2\rangle}{r_{2m}^2}\right)\right)\right\rangle \\
&\quad \prod_{m'\neq m}^{M}\left\langle\exp\left(-i\frac{1}{M}(\theta_{1m'}-\theta_{2m'})\right)\exp\left(-\frac{1}{4M^2\mathrm{CNR}_{\mathrm{det}}(m',t)}\left(\frac{\langle r_{1m'}^2\rangle}{r_{1m'}^2}+\frac{\langle r_{2m'}^2\rangle}{r_{2m'}^2}\right)\right)\right\rangle.
\end{aligned} \tag{5.54}$$

The means in the right hand side of Eq. 5.54 can be evaluated by using the assumption, explained in connection with Eqs. 5.26 and 5.27, that $\zeta_R^0(\vec{\rho}_1;k_m,t)$ and $\zeta_R^0(\vec{\rho}_2;k_m,t)$ are jointly Gaussian random variables. Using this assumption, the first term on the right hand side of Eq. 5.54 can be written as [53]

$$\begin{aligned}
&\left\langle r_{1m}r_{2m}\exp\left(i\frac{M-1}{M}(\theta_{1m}-\theta_{2m})\right)\exp\left(-\frac{1}{4M^2\mathrm{CNR}_{\mathrm{det}}(m,t)}\left(\frac{\langle r_{1m}^2\rangle}{r_{1m}^2}+\frac{\langle r_{2m}^2\rangle}{r_{2m}^2}\right)\right)\right\rangle \\
&\quad = \frac{1}{\pi^2}(1-|\mathrm{x}_m|^2)^2\langle|\zeta_R^0(\vec{\rho};k_m,t)|^2\rangle\int_0^{2\pi}d\theta_1\int_0^{2\pi}d\theta_2\int_0^{\infty}du_1\int_0^{\infty}du_2\,u_1^2u_2^2\cdot \\
&\quad \exp(-(u_1^2+u_2^2-2|\mathrm{x}_m|u_1u_2\cos(\theta_1-\theta_2-\angle\mathrm{x}_m))\exp\left(i\frac{M-1}{M}(\theta_1-\theta_2)\right)\cdot
\end{aligned}$$

$$\exp\left(-\frac{1}{4M^2\mathrm{CNR}_{\mathrm{det}}(m,t)}\cdot\frac{1}{1-|\mathbf{x}_m|^2}\cdot\left(\frac{1}{u_1^2}+\frac{1}{u_2^2}\right)\right). \tag{5.55}$$

Equation 5.55 can be evaluated as follows. As explained in Section 5.2, the form of the initial condition Eq. 5.30 implies that $\angle\mathbf{x}_m = 0$. Performing the change of variables $\alpha = (\theta_1+\theta_2)/2$, $\beta = \theta_1 - \theta_2$, $w = 2u_1u_2$, $c = u_1/u_2$, evaluating the α integral, and using Eq. 5.34 to evaluate the c integral gives

$$\begin{aligned}\Bigg\langle r_{1m}r_{2m}\exp\left(i\frac{M-1}{M}(\theta_{1m}-\theta_{2m})\right)\exp\left(-\frac{1}{4M^2\mathrm{CNR}_{\mathrm{det}}(m,t)}\left(\frac{\langle r_{1m}^2\rangle}{r_{1m}^2}+\right.\right.&\\ \left.\left.\frac{\langle r_{2m}^2\rangle}{r_{2m}^2}\right)\right)\Bigg\rangle &= \langle|\zeta_R^0(\vec\rho;k_m,t)|^2\rangle\, G_M(|\mathbf{x}_m(\vec\rho_1,\vec\rho_2;t)|,\mathrm{CNR}_{\mathrm{det}}(m,t)), \end{aligned} \tag{5.56}$$

where

$$\begin{aligned}G_M(x,y) &\equiv \frac{(1-x^2)^2}{2\pi}\int_0^{2\pi}d\beta\int_0^{\infty}dw\,w^2\,e^{xw\cos\beta}\left(1-\frac{\beta}{2\pi}\right)\cos\left(\frac{M-1}{M}\beta\right)\cdot\\ &\qquad K_0\left(w+\frac{1}{M^2y}\frac{1}{1-x^2}\frac{1}{w}\right).\end{aligned} \tag{5.57}$$

Equation 5.56 allows the first mean in the right hand side of Eq. 5.54 to be evaluated; the second term has been evaluated in Section 5.2 and is given by $\prod_{m'\neq m}^{M} F_M(|\mathbf{x}_{m'}(\vec\rho_1,\vec\rho_2;t)|,\mathrm{CNR}_{\mathrm{det}}(m',t))$, where $F_M(x,y)$ is defined in Eq. 5.36. Thus, evaluation of the right hand side of Eq. 5.54 gives

$$\begin{aligned}&\langle\zeta_R^0(\vec\rho_1;k_m,t)e^{-i\phi_{sp}(\vec\rho_1;t)}\zeta_R^{0*}(\vec\rho_2;k_m,t)e^{i\phi_{sp}(\vec\rho_2;t)}\rangle =\\ &\quad\langle|\zeta_R^0(\vec\rho;k_m,t)|^2\rangle G_M(|\mathbf{x}_m(\vec\rho_1,\vec\rho_2;t)|,\mathrm{CNR}_{\mathrm{det}}(m,t))\cdot\\ &\quad\prod_{m'\neq m}^{M} F_M(|\mathbf{x}_{m'}(\vec\rho_1,\vec\rho_2;t)|,\mathrm{CNR}_{\mathrm{det}}(m',t)),\end{aligned} \tag{5.58}$$

and substituting Eq. 5.58 into Eq. 5.52 gives

$$\begin{aligned}\langle|\ell_{\mathrm{radar}}(t)|^2\rangle &= P_T\epsilon_{opt}\frac{4N}{\pi d^2}\sum_{m=1}^{M}\langle|\zeta_R^0(\vec\rho;k_m,t)|^2\rangle\cdot\\ &\qquad\int_R d\vec\rho_1\int_R d\vec\rho_2\,G_M(|\mathbf{x}_m(\vec\rho_1,\vec\rho_2;t)|,\mathrm{CNR}_{\mathrm{det}}(m,t))\cdot\\ &\qquad\prod_{m'\neq m}^{M} F_M(|\mathbf{x}_{m'}(\vec\rho_1,\vec\rho_2;t)|,\mathrm{CNR}_{\mathrm{det}}(m',t))\end{aligned} \tag{5.59}$$

for the mean-squared, phase-corrected, IF filtered target return.

To complete the evaluation of the CNR, the mean-squared, phase-corrected, IF filtered shot noise $\langle|\mathbf{n}_{\text{radar}}(t)|^2\rangle$ must be evaluated. Equation 5.22 shows that $\mathbf{n}_{\text{radar}}(t)$ is the sum of terms in which the filtered LO shot noise $\mathbf{n}_n(k_m, t)$, is multiplied by the phase factor $e^{-i\{\phi_R(\vec{\rho}_n,\vec{0};t)+\bar{\phi}_{sp}(\vec{\rho}_n;t)\}}$. The turbulence phase, $\phi_R(\vec{\rho}_n, \vec{0}; t)$, is clearly independent of the LO shot noise. When $\text{CNR}_{\text{det}}(m, t)$ is large, the fluctuations in $\bar{\phi}_{sp}(\vec{\rho}_n; t)$ are dominated by the fluctuations in the received speckle fields at the various wavelengths, rather than by the fluctuations in the LO shot noise (see Eq. 5.18). Thus, we shall make the approximation that for $\text{CNR}_{\text{det}}(m, t) \geq 10$, $\bar{\phi}_{sp}(\vec{\rho}_n; t)$ is independent of $\mathbf{n}_n(k_m, t)$. In this case, we have from Eq. 5.22 that

$$\begin{aligned} \langle|\mathbf{n}_{\text{radar}}(t)|^2\rangle \;=\; & \sum_{m=1}^{M}\sum_{n=1}^{N}\sum_{m'=1}^{M}\sum_{n'=1}^{N}\langle \mathbf{n}_n(k_m, t)\mathbf{n}^*_{n'}(k_{m'}, t)\rangle \cdot \\ & \langle e^{-i\{\phi_R(\vec{\rho}_n,\vec{0};t)+\bar{\phi}_{sp}(\vec{\rho}_n;t)\}} e^{i\{\phi_R(\vec{\rho}_{n'},\vec{0};t)+\bar{\phi}_{sp}(\vec{\rho}_{n'};t)\}}\rangle. \end{aligned} \tag{5.60}$$

Using the fact that $\mathbf{n}_n(k_m. t)$ is independent from one detector to another and from on wavelength to another, and using Eq. 5.12, Eq. 5.60 can be simplified, giving

$$\langle|\mathbf{n}_{\text{radar}}(t)|^2\rangle = MNh\nu_0 B/\eta. \tag{5.61}$$

Finally, the CNR can be found from the ratio of Eq. 5.59 to Eq. 5.61, and is given by

$$\begin{aligned} \text{CNR} \;=\; & \frac{\eta P_T \epsilon_{opt}}{h\nu_0 B}\frac{4}{\pi d^2}\frac{1}{M}\sum_{m=1}^{M}\langle|\zeta_R^0(\vec{\rho}; k_m, t)|^2\rangle \cdot \\ & \int_R d\vec{\rho}_1 \int_R d\vec{\rho}_2\, G_M(|\mathbf{x}_m(\vec{\rho}_1, \vec{\rho}_2; t)|, \text{CNR}_{\text{det}}(m, t)) \cdot \\ & \prod_{m' \neq m}^{M} F_M(|\mathbf{x}_{m'}(\vec{\rho}_1, \vec{\rho}_2; t)|, \text{CNR}_{\text{det}}(m', t)). \end{aligned} \tag{5.62}$$

In the numerical evaluation of Eq. 5.62, the two approximations discussed in the beginning of Section 5.3 are made. The first is that in sequencing through the iteration equations in order to arrive at steady state, $\text{CNR}_{\text{det}}(m, t)$ is assumed to be independent of m and of t. Thus, $\langle|\zeta_R^0(\vec{\rho};k_m,t)|^2\rangle$ is written as $\rho/(\pi L^2)e^{-2\alpha L}\epsilon$, where ϵ is a constant. The second is that each term which depends on k_m is approximated by its value at k_{av}. Using these approximations, together with Eq. 5.41, in Eq. 5.62 gives

$$\begin{aligned} \text{CNR} \;=\; & \frac{\eta P_T \epsilon_{opt}}{h\nu_0 B}\frac{4}{\pi d^2}\frac{\rho}{\pi L^2}e^{-2\alpha L}\epsilon \cdot \\ & \int_R d\vec{\rho}_1 \int_R d\vec{\rho}_2\, G_M\left(C_R\left(\frac{|\vec{\rho}_1-\vec{\rho}_2|}{d};k_{av},t\right), \text{CNR}_{\text{det}}\right)\cdot \\ & \left[F_M\left(C_R\left(\frac{|\vec{\rho}_1-\vec{\rho}_2|}{d};k_{av},t\right), \text{CNR}_{\text{det}}\right)\right]^{M-1}, \end{aligned} \tag{5.63}$$

where we have used the fact that $\mathrm{x}_m(\vec{\rho}_1,\vec{\rho}_2;t)$ is real and positive, a consequence of the form of the initial condition, Eq. 5.30.

The significance of the CNR formula of Eq. 5.63 can be seen by comparing it with the corresponding result in the absence of turbulence and of wavefront correction, i.e. the CNR for the case in which the transmitted beam pattern is the Gaussian beam of Eq. 3.1, and the LO beam pattern is a uniform plane wave over the aperture region. It can be seen from Eq. 5.51 that in the absence of turbulence, when only one wavelength is transmitted, the mean-squared IF filtered target return is given by

$$\langle|\ell(t)|^2\rangle = P_T\epsilon_{opt}\frac{4}{\pi d^2}\int_R d\vec{\rho}_1\int_R d\vec{\rho}_2\langle\zeta_R^0(\vec{\rho}_1;k,t)\zeta_R^{0*}(\vec{\rho}_2;k,t)\rangle, \tag{5.64}$$

where we have used $\xi_{LO}^*(\vec{\rho}) = \sqrt{4/(\pi d^2)}$ for the LO beam pattern. In the absence of turbulence and of wavefront correction, $\zeta_R^0(\vec{\rho};k,t)$ is given by Eq. 5.7 without the spatial low pass filter, i.e. with $h(\vec{\rho}) = \delta(\vec{\rho})$, and with $\xi_t(\vec{\rho}\,';k,t)$ given by Eq. 5.6 with $\zeta_T(\vec{\rho};t) = \xi_0(\vec{\rho})$ and $\phi_F(\vec{0},\vec{\rho};t) = 0$. Using Eq. 5.7 and 5.6 with the above modifications gives

$$\langle\zeta_R^0(\vec{\rho}_1;k,t)\zeta_R^{0*}(\vec{\rho}_2;k,t)\rangle = \frac{\rho}{\pi L^2}e^{-2\alpha L}\cdot\frac{1}{1+\left(\frac{4\lambda L}{\pi d d_T}\right)^2}\cdot\exp\left\{-\frac{4|\vec{\rho}_1-\vec{\rho}_2|^2/d^2}{1+\left(\frac{4\lambda L}{\pi d d_T}\right)^2}\right\}, \tag{5.65}$$

in the absence of turbulence and of wavefront correction. The CNR in the absence of turbulence and of wavefront correction can be found by substituting Eq. 5.65 into Eq. 5.64, and by using Eq. 5.12 for $\langle|\mathbf{n}(t)|^2\rangle$. The result is

$$\begin{aligned}\mathrm{CNR}_0 &= \frac{\eta P_T \epsilon_{opt}}{h\nu_0 B}\frac{4}{\pi d^2}\frac{\rho}{\pi L^2}e^{-2\alpha L}\cdot\frac{1}{1+\left(\frac{4\lambda L}{\pi d d_T}\right)^2}\cdot \\ &\quad \int_R d\vec{\rho}_1\int_R d\vec{\rho}_2 \exp\left[-\frac{4|\vec{\rho}_1-\vec{\rho}_2|^2/d^2}{1+\left(\frac{4\lambda L}{\pi d d_T}\right)^2}\right].\end{aligned} \tag{5.66}$$

The ratio of the CNR of the multiwavelength system with phase correction of both beams to the corresponding no-turbulence, no-correction CNR is the ratio of Eq. 5.63 to Eq. 5.66. This ratio is evaluated here for the case of an infinite target (i.e. $\pi d d_T \gg 4\lambda L$) for simplicity, and in this limiting case is given by

$$\frac{\mathrm{CNR}}{\mathrm{CNR}_0} = \frac{\epsilon\int_0^1 du\,u\,f(u)\,G_M(C_R(u;k_{av},t),\mathrm{CNR}_{\mathrm{det}})[F_M(C_R(u;k_{av},t),\mathrm{CNR}_{\mathrm{det}})]^{M-1}}{\int_0^1 du\,u\,f(u)e^{-4u^2}}, \tag{5.67}$$

where

$$f(u) \equiv \frac{1}{2}(\cos^{-1}(u) - u\sqrt{1-u^2}) \tag{5.68}$$

is the area of overlap between two circles [56] of diameter 1 whose centers are separated by a distance u. In evaluating Eq. 5.67 the factor ϵ is evaluated by using Eq. 5.41 with $C_{sp}(u,t)$ being the result at the end of ten iterations, and with N_{eff} evaluated at $k_m = k_{av}$. The ratio given in Eq. 5.67 is plotted in Figure 5.11 as a function of N_{eff} (which equals N for $d_T \rightarrow \infty$), for $\mathrm{CNR}_{\mathrm{det}} = 10.0$, and for $M = 1$, 2, and 4 at the end of ten iterations. The initial condition used was $d/\rho_0 = 10.0$, but only the $M = 1$ results depend on the initial condition. The no-correction result for $d/\rho_0 = 10.0$ is also shown for comparison. Figure 5.11 shows that for both $M = 2$ and $M = 4$, the CNR reduction factor is between 0.52 and 0.56. In other words, the multiwavelength radar system described here can restore the CNR to within 3 decibels of the no-turbulence value when the system is in steady state. When

$M = 1$, the CNR is even larger than the no-turbulence value, as predicted in the beginning of Section 5.2. When $M = 1$, the LO phase correction (for large $\mathrm{CNR}_{\mathrm{det}}$) is the complex conjugate of the sum of the turbulence phase and the speckle phase of the received wave, so that the phase distortions in the received wave are entirely cancelled. This LO correction gives a better spatial matching between the received and LO waves than any other phase correction.

For other finite values of M, the speckle component of the LO phase correction is the speckle phase averaged over the different wavelengths, so it does not exactly match the speckle distortions in the received wave. However, for $M \to \infty$, the speckle component of the transmitted-wave and LO corrections is completely suppressed, and therefore the CNR approaches its no-turbulence value for large values of N_{eff}. Mathematically, this can be seen by examining the behavior of the functions $F_M(x, y)$ and $G_M(x, y)$ as $M \to \infty$. It can be seen from Eq. 5.27 that when $M \to \infty$, each factor in the product from $m = 1$ to M is the integral of a probability distribution, which is identically 1. Thus, Eq. 5.35 shows that the function $F_M(x, y)$ must be identically 1 for $M \to \infty$, and for the linearization of the IF signal phase used here. A similar argument can be made regarding the function $G_M(x, y)$. It can be seen from Eq. 5.54 that when $M \to \infty$, the right hand side of this equation approaches $\langle r_{1m} r_{2m} \exp(i(\theta_{1m} - \theta_{2m}))\rangle$, which by definition equals $\langle \zeta_R^0(\vec{\rho}_1; k_m, t)\zeta_R^{0*}(\vec{\rho}_2; k_m, t)\rangle$. Thus, Eqs. 5.57 and 5.28 show that the function $G_M(x, y)$ must approach x for $M \to \infty$, and for the linearization of the IF signal used here. In order to evaluate the ratio $\mathrm{CNR}/\mathrm{CNR}_0$ from Eq. 5.67, we must now find ϵ and $C_R(u; k_{av}, t)$ in the limit of $M \to \infty$. Both of these quantities can be simply evaluated from Eqs. 5.44 and 5.40 respectively, by noting that since $F_M(x, y) \equiv 1$ for $M \to \infty$, it follows that $C_{sp}(u; t) \equiv 1$ for $M \to \infty$. Using these results, it is found that

$$\lim_{M \to \infty} \frac{\mathrm{CNR}}{\mathrm{CNR}_0} = \frac{[\pi^2 N_{\mathit{eff}}/(16 + \pi^2 N_{\mathit{eff}})] \cdot \int_0^1 du\, u f(u) e^{-4\pi^2 N_{\mathit{eff}} u^2/(16+\pi^2 N_{\mathit{eff}})}}{\int_0^1 du\, u f(u) e^{-4u^2}}. \qquad (5.69)$$

It can be seen from Eq. 5.69 that for $M \rightarrow \infty$ and$N_{eff} \rightarrow \infty$, CNR/CNR$_0 \rightarrow 1$. Figure 5.11 shows that for the values of N_{eff} plotted, the CNR would be very close to its no-turbulence value for $M \rightarrow \infty$. On the other hand, when CNR$_{det} \rightarrow \infty$ for finite M, the CNR does not approach the no-turbulence value because of the incomplete speckle suppression and the resulting spatial mismatch between the received and LO beams. Mathematically, Eq. 5.27 and 5.35 show that when CNR$_{det} \rightarrow \infty$ for finite M, $F_M(x, y)$ does not approach 1. Similarly, Eqs. 5.57 and 5.28 show that when CNR$_{det} \rightarrow \infty$ for finite M, $G_M(x, y)$ does not approach x. Thus, CNR/CNR$_0$ does not approach 1 as CNR$_{det} \rightarrow \infty$ for finite M.

The CNR reduction factor depends very weakly on N for those values shown in the plot, because it is assumed in deriving all the results given here that N is large enough so that the turbulence phase distortions can be perfectly measured and corrected. If N is this large, then increasing N further does not appreciably affect the performance, for CNR$_{\text{det}}$ fixed.

5.4.3 Range and Velocity Accuracy

In order to derive the range and velocity accuracy, we must find the probability of anomaly and the local mean-squared error. In Section 3.4 results for these quantities in the presence of turbulence were obtained from the no-turbulence speckle target results. However, such a procedure cannot be used to find the steady-state range and velocity accuracy of this multiwavelength radar system, for the following reason. It is assumed here that this system can perfectly correct the turbulence phase distortions, so that the only imperfection in the applied phase corrections is the residual speckle component $\bar{\phi}_{sp}(\vec{\rho}; t)$ (which includes the shot noise effects). Thus, the only deviation in the steady-state performance of the system from the no-turbulence speckle target performance is due to this residual speckle phase. Therefore, the target return depends on the $\mathbf{T}(\vec{\rho}'; k, t)$ term in the target-plane spatial overlap integral, as it does in the no-turbulence case, but it also depends on $\mathrm{T}(\vec{\rho}\,'; k, t)$ through its dependence on $\bar{\phi}_{sp}(\vec{\rho}; t)$. Therefore, the probability distribution of the target return intensity due to the speckle randomness is no longer exponential. This implies, for example, that in the Pr(A) expression of Eq. 3.12, we must replace the term $\exp[-u/(1+\mathrm{CNR})]/(1+\mathrm{CNR})$ by an expression with a different dependence on the mean-squared target return and on the mean-squared shot noise; we cannot simply replace CNR with an expression of the form $\mathrm{CNR}_T \cdot x$. Similarly, the likelihood ratio of Eq. 3.15, which represents the randomness in the target return due to speckle and shot noise, would have a different form.

Although it is difficult to evaluate the range and velocity accuracy of this system, an approximation for the accuracy can be obtained as follows. Since it is assumed here that this system can perfectly correct the turbulence phase distortions, it follows that the fluctuations in the target return are due only to speckle. As mentioned above, the target return depends on speckle through its dependence on $\mathrm{T}(\vec{\rho}\,'; k, t)$ in the target-plane spatial overlap integral, and through its dependence on $\bar{\phi}_{sp}(\vec{\rho}; t)$ in the transmitted-wave and LO correction. It was found in Sections 5.4.1 and 5.4.2 that for $M > 1$ the steady-state spatial resolution is very close to diffraction-limited (see Figure 5.10), and the CNR is within 3 decibels of the no-turbulence value. These results suggest that for $M > 1$, the speckle fluctuations in the target return in steady state are due mainly to the term $\mathrm{T}(\vec{\rho}\,'; k, t)$ in the target-plane spatial overlap integral, rather than to the term $\bar{\phi}_{sp}(\vec{\rho}; t)$ in the transmitted-wave and LO correction. Therefore, the accuracy can be approximated by by using the no-turbulence formula evaluated at the CNR of Eq. 5.63. Making this approximation amounts to saying that the term $\bar{\phi}_{sp}(\vec{\rho}; t)$ affects the accuracy by reducing the mean-squared target return, but not by causing fluctuations in the target return. Thus, the actual accuracy would be worse than that given by this approximation, because the fluctuations in $\bar{\phi}_{sp}(\vec{\rho}; t)$ would lead to additional fading in the target return, which would increase the probability of anomaly and increase the local mean-squared error.

The discussion in the previous paragraph applies to cases in which $M > 1$. For $M = 1$, Figure 5.11 shows that the CNR is even larger than the no-turbulence value, due to the high degree of spatial matching between the phases of the received and of the LO wave. In this case, the only fluctuations in the target return are due to the fluctuations in $|\zeta_R^0(\vec{\rho}; k_m, t)|$ (see Eq. 5.23), but the target return depends on the integral of $|\zeta_R^0(\vec{\rho}; k_m, t)|$ over the aperture, so the fluctuations in $|\zeta_R^0(\vec{\rho}; k_m, t)|$ are reduced by aperture averaging (recall that for $M = 1$ the spot size on target is even larger than turbulence-limited, and therefore the coherence length of $\zeta_R^0(\cdot)$ is less than ρ_0). Thus, in this case the speckle fluctuations in the target return are less than what they would be in the absence of turbulence and of wavefront correction. Therefore, for $M = 1$ the range and velocity accuracy should be close to or slightly better than the no-turbulence accuracy.

5.5 Summary

In Chapter 5, a radar system with adaptive phase correction was presented, and its performance was analyzed. This system corrects the turbulence phase distortions in both the transmitted and LO beams. It measures the turbulence information necessary for wavefront correction from the target return. The beginning of Chapter 5 discusses a way to obtain the necessary turbulence information from the target return. Section 5.1 presents the structure and operation of the proposed radar system. Section 5.2 derives the iteration equations that can be used to evaluate the system's performance. Section 5.3 discusses some approximations used in the numerical evaluation of the iteration equations. It mentions the parameters on which the system's performance depends, and gives ranges of values of these parameters which correspond to the expected operating conditions of such a system. It also discusses the convergence to steady state for $M > 1$ and for $M = 1$. Section 5.4 derives equations for the spatial resolution and CNR, and evaluates them in steady state for the ranges of parameter values selected in Section 5.3. It also discusses the improvement in range and velocity measurement accuracy which this system can be expected to give. A more detailed summary of the results obtained in Chapter 5 is given below.

The beginning of Chapter 5 points out that the target return contains the turbulence information necesssary for LO correction. This turbulence information can also be used to correct the transmitted wave because of the reciprocity of the turbulent atmosphere, under two conditions. First, the point-ahead angle, $2v_{\perp}/c$, must be smaller than ρ_0'/L to ensure that the turbulence through which the target return has traveled is highly correlated with the turbulence through which the transmitted wave will travel. Second, the spot size on target, whose turbulence-limited value is of the order of $\lambda L/\rho_0$, must be smaller than ρ_0' to ensure that the correction to apply for transmission to a single target-plane turbulence coherence area can be obtained from the target return.

Even if the above two conditions are met, so that the target return contains the necessary turbulence information for correction of both waves, the turbulence distortions in the received wave must be separated from the speckle distortions in order to extract this turbulence information. This separation can be accomplished by transmitting multiple wavelengths, such that the received speckle distortions at the different wavelengths are uncorrelated, but the received turbulence distortions are highly correlated. It was found that up to four wavelengths can be used for the nighttime turbulence profile of Figure 2.2, and up to two wavelengths can be used for the corresponding daytime turbulence profile. Section 5.1 describes the structure and operation the system shown in Figure 5.1.

In Section 5.2 the system's iteration equations are derived. First, two limiting cases are qualitatively considered for the case in which shot noise has a negligible effect on phase estimation. For $M = 1$ it is expected that the spatial resolution will be close to turbulence-limited, but that the CNR will be larger than the no-turbulence value. For $M \rightarrow \infty$, the performance is expected to be very close to the no-turbulence performance.

After consideration of these limiting cases, the equations which describe the propagation and correction of the waves are derived. In this derivation it is assumed that N is large enough that the received turbulence distortions are approximately constant over each detector. It is also assumed that $\mathrm{CNR}_{\mathrm{det}} \geq 10.0$ so that the phase of the IF signal can be linearized. The procedure for making intensity, velocity, and/or range measurements with this radar system is then described.

The nature of the system equations just derived indicates that the statistical properties of the wavefronts chage discretely in time, at every $2L/c$ after t_0. The nature of these equations also shows that the system is a closed loop, and that it should reach steady state after some number of iterations. In deriving the iteration equations it is assumed that $\zeta_R^0(\vec{\rho}_1; k_m, t)$ and $\zeta_R^0(\vec{\rho}_2; k_m, t)$ are jointly Gaussian random variables. The form of the initial condition, Eq. 5.30, allows the iteration equations to be greatly simplified, and the simplified equations are displayed in Table 5.2.

Section 5.3 discusses the procedure used for numerical evaluation of the iteration equations. First, the approximations used are discussed. $\mathrm{CNR}_{\mathrm{det}}(m, t)$ is assumed to be independent of m and of t. Also, all functions of k_m are evaluated at $k_m = k_{av}$, since the relative separation among the wavelengths is small.

It is pointed out that the system performance depends on four parameters: d/ρ_0 (for the initial condition), $\mathrm{CNR}_{\mathrm{det}}$, M, and N_{eff}. The section then discusses the values these parameters may be expected to take on in the operation of this system. The parameter d/ρ_0 may be expected to be close to 10 or larger, since the turbulence-induced wavefront distortions severely degrade the radar performance for such values of d/ρ_0. Figures 5.3a and 5.3b show aperture diameters and zenith angles for which $d/\rho_0 = 10$, for two different wavelengths and for the daytime and nighttime turbulence profiles of Figure 2.2. The parameter $\mathrm{CNR}_{\mathrm{det}}$ has already been assumed to be at least 10 in order to linearize the phase of the IF signal. Furthermore, $\mathrm{CNR}_{\mathrm{det}}$ is expected to satisfy this condition in order to ensure the usefulness of the phase measurements derived from the received wave. Figures 5.4a and 5.4b show the maximum altitude for which $\mathrm{CNR}_{\mathrm{det}} = 10$ as a function of zenith angle, for two different wavelengths and for the daytime and nighttime turbulence profiles of Figure 2.2. The maximum possible value of the parameter M is expected to be in the range of 2 to 4, depending on the turbulence conditions. The fourth parameter, N_{eff}, is a function of five other parameters. To get an idea of what range of values it may be expected to take on, it is plotted in Figures 5.5a and 5.5b as a function of d_T and d/ρ_0, for two different wavelengths. In these plots it is assumed that $\mathrm{CNR}_{\mathrm{det}} = 10.0$ with the parameter values of Table 5.3, that $\theta = 45^\circ$, and that $N = 4(d/\rho_0)^2$. For $\lambda = 10.6\mu\mathrm{m}$, N_{eff} would be a few hundred, while for $\lambda = 5\mu\mathrm{m}$, N_{eff} would be several hundred or even larger.

The next issue addressed is the convergence to steady state. For $M > 1$, the system converges to steady state within about six iterations for d/ρ_0 between 5 and 20, and it converges more rapidly for large values of d/ρ_0. For $M = 1$, the spot size on target gets larger in each iteration until it fills the target. When the spot fills the target, the system is in steady state. Figures 5.8 and 5.9 show the 0.5 and 0.1 spot sizes at the end of ten iterations for $d/\rho_0 = 10.0$; $\mathrm{CNR}_{\mathrm{det}} = 10.0$; $M = 1$, 2, and 4; and N_{eff} between 200 and 2000. The $M = 2$ and $M = 4$ results are very close to diffraction-limited, but the $M = 1$ results are worse than the results for no correction.

Section 5.4 derives the spatial resolution and CNR of this system, and estimates its range and velocity accuracy. In deriving the spatial resolution, the approximation is made that in the expansion of the mean-squared target return as a double sum over the M transmitted wavelengths, the contribution of terms which are a product of terms corresponding to received waves at two different wavelengths is zero. This approximation is based on consideration of the spatial characteristics of the terms in the target-plane spatial overlap integral. The spatial resolution is plotted in Figure 5.10 as a function of the same parameter values used in Figures 5.8 and 5.9. The steady-state spatial resolution for $M > 1$ is very close to diffraction limited. For $M = 1$ it is worse than it would be in the absence of wavefront correction. It is not *better* than the no-correction result, because there is no speckle averaging to reduce the residual speckle component of the wavefront correction in each iteration. Furthermore, it is *worse* than the no-correction result because of the particular form of the correlation function of the transmitted speckle distortion as compared to that of the turbulence distortion, i.e. the transmitted distortion in the absence of wavefront correction.

In deriving the CNR, the approximation mentioned above in connection with the derivation of the spatial resolution is used again. Also, the approximation is made that when $\mathrm{CNR}_{\mathrm{det}}$ is large, the randomness of $\bar{\phi}_{sp}(\vec{\rho};t)$ is dominated by the speckle fluctuations as opposed to the shot noise fluctuations. Using these approximations, the CNR reduction factor is derived. This reduction factor is the ratio of the CNR of the multiwavelength radar system with both beams corrected to the no-turbulence, no-correction CNR when the transmitted and LO beam patterns are the corresponding uncorrected beam patterns of the multiwavelength radar system. This reduction factor is plotted in Figure 5.11, which shows that for $M > 1$, the steady-state CNR is within 3 decibels of the no-turbulence value. The steady-state CNR for $M \rightarrow \infty$ approaches the no-turbulence value for large values of N_{eff}, when the IF signal phase linearization used here is valid. However, for $\mathrm{CNR}_{det} \rightarrow \infty$, the CNR does not approach its no-turbulence value. Figure 5.11 also shows that for $M = 1$, the CNR (after 10 iterations) is slightly larger than the no-turbulence value. Because both the turbulence and speckle phase distortions in the received wave are corrected when $M = 1$, the spatial matching between the received and LO waves is better than it is in the absence of turbulence. Thus, for $M = 1$ it would be best to correct only the LO, since it is the LO correction which gives the CNR improvement, while the transmitter correction just degrades the spatial resolution.

The accuracy of range and velocity measurements was not actually derived, but it was argued that the spatial resolution and CNR results given here show that the fluctuations in $\bar{\phi}_{sp}(\vec{\rho};t)$ must be small in steady state, and therefore the dependence of the range and velocity accuracy on CNR_0 should be close to its dependence on CNR_0 in the no-turbulence case. Since the residual speckle distortion $\bar{\phi}_{sp}(\vec{\rho};t)$ leads to a steady-state CNR loss of less than 3 decibels, the range and velocity accuracy should be close to their no-turbulence values.

In conclusion, a radar system is presented which corrects the phases of both the transmitted and LO waves. Its performance is theoretically derived, and numerically evaluated for conditions under which such a system may be expected to operate. The performance results presented show that for $M > 1$, the steady-state performance is close to the no-turbulence performance, which is a dramatic improvement over the no-correction performance for large d/ρ_0. For $M = 1$, the spatial resolution is worse than the no-correction result. However, the CNR is better than the no-turbulence value, and so it is expected that the accuracy of range and velocity measurements is close to and perhaps better than the no-turbulence value. Thus, it seems worthwhile to try to build such a system, if the radar would be operating in conditions for which $d/\rho_0 \geq 10$, and if the conditions necessary for measurement of the turbulence phase from the target return can be met (i.e. if $2v_\perp/c < \rho_0'/L$, $\lambda L/\rho_0 < \rho_0'$, and $\mathrm{CNR}_{\mathrm{det}} \geq 10$ for $N \geq 4(d/\rho_0)^2$).

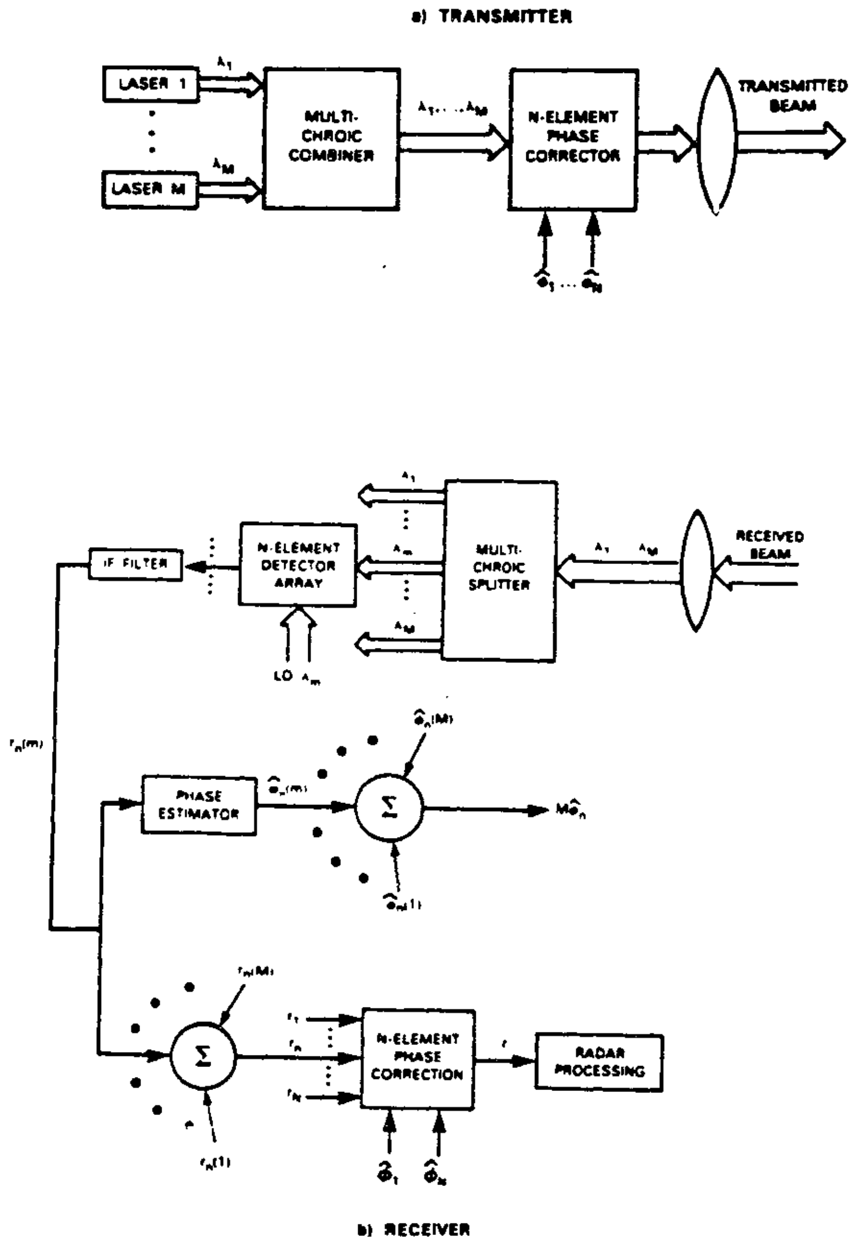

Figure 5.1: Multiwavelength phase correction system for a coherent laser radar—intensity imaging. (a) transmitter, (b) receiver.

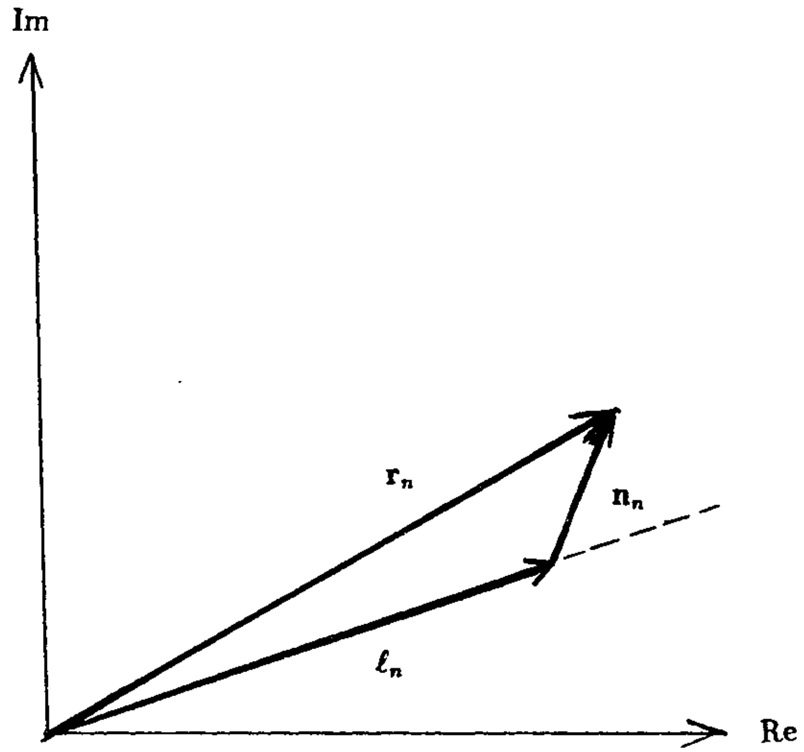

Figure 5.2: Diagram to illustrate linearization of IF signal phase.

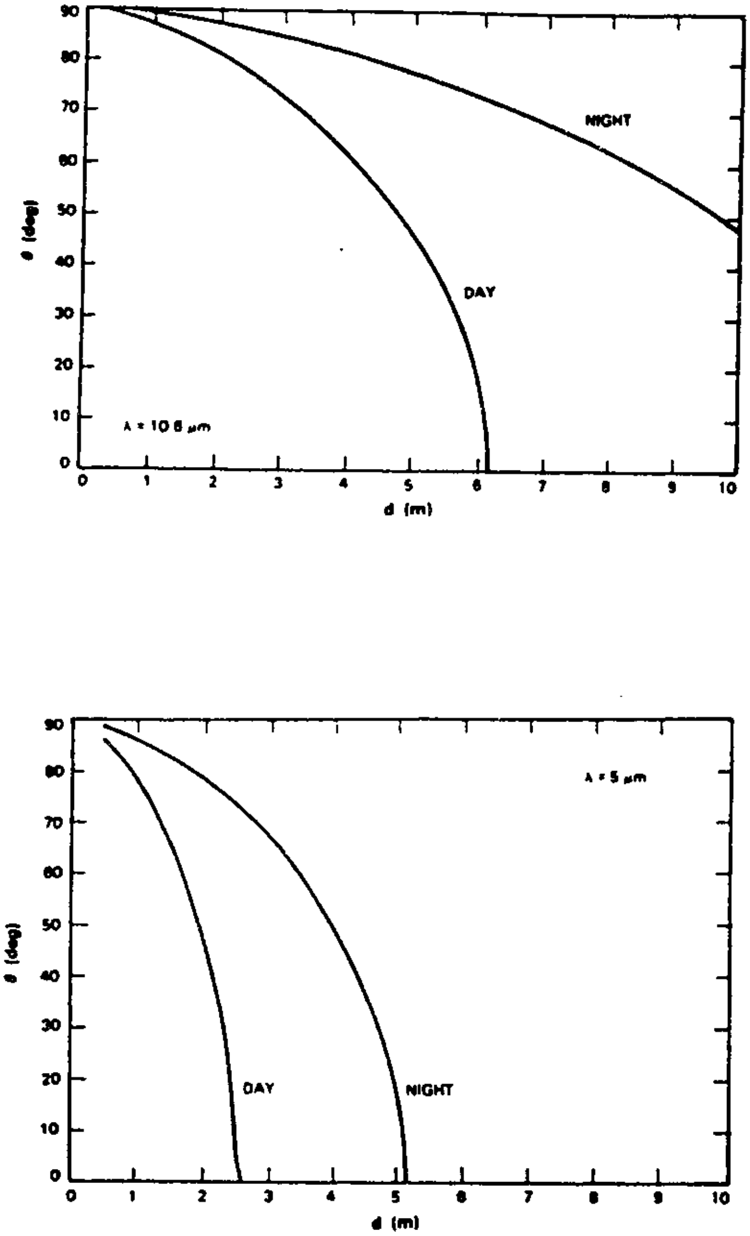

Figure 5.3: Zenith angle θ vs. aperture diameter d such that $d/\rho_0 = 10$ in daytime and nighttime turbulence. (a) $\lambda = 10.6\,\mu$m, (b) $\lambda = 5\,\mu$m.

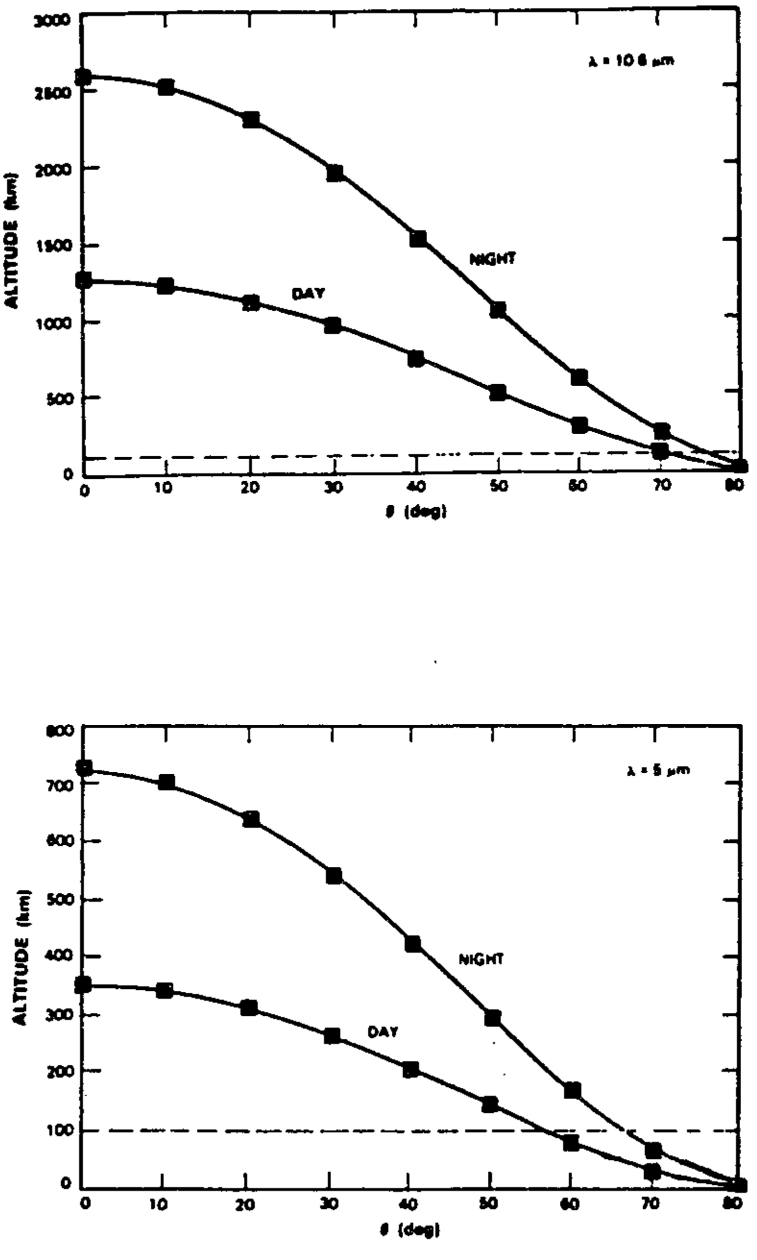

Figure 5.4: Maximum altitude vs. zenith angle for achieving $\mathrm{CNR}_{det} = 10$ in daytime and nighttime turbulence. (a) $\lambda = 10.6\,\mu\mathrm{m}$, (b) $\lambda = 5\,\mu\mathrm{m}$.

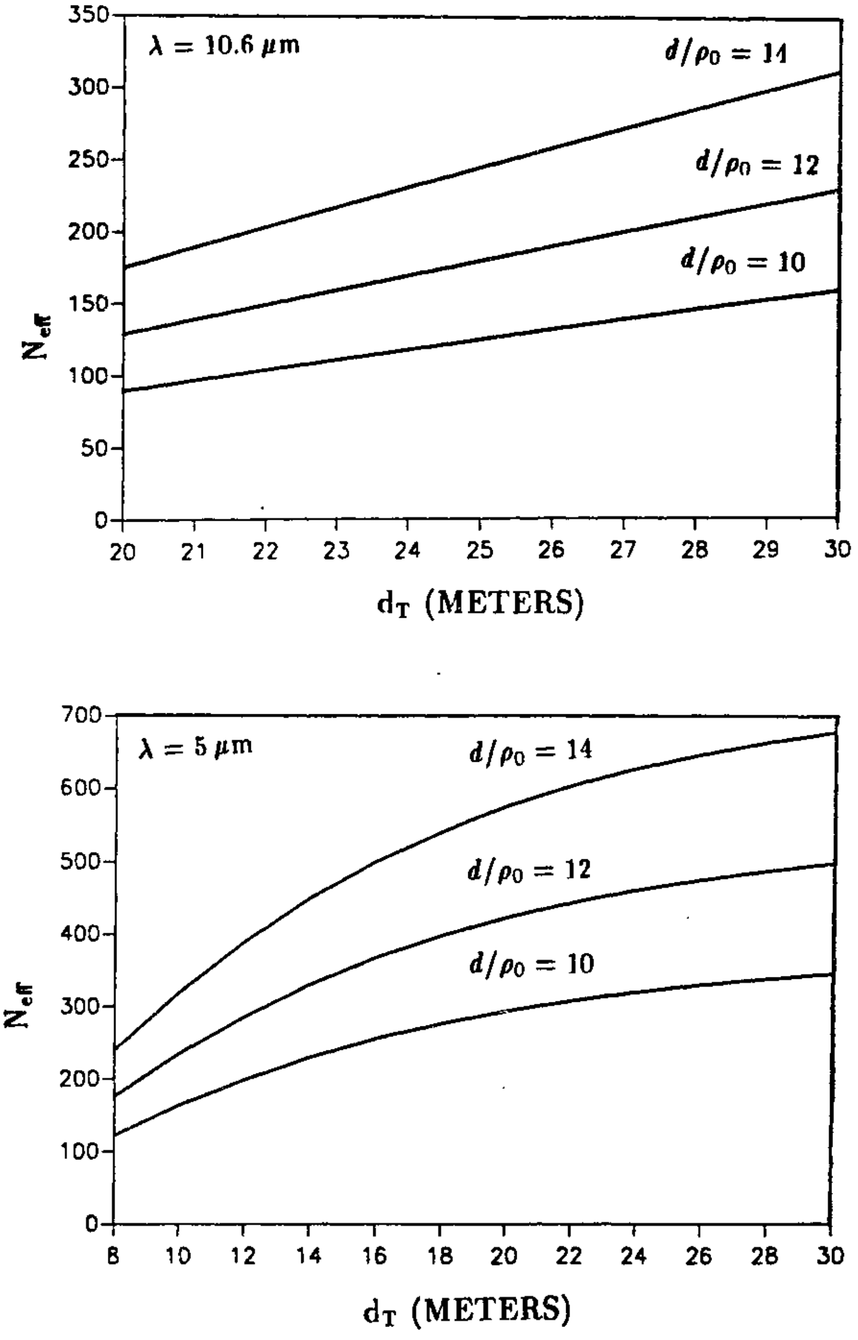

Figure 5.5: Power & information loss parameter N_{eff} vs. target diameter for various d/ρ_0 values; $\text{CNR}_{det} = 10.0$, $N = 4(d/\rho_0)^2$, $\theta = 45°$, with parameter values of Table 5.3. (a) $\lambda = 10.6\,\mu m$, (b) $\lambda = 5\,\mu m$.

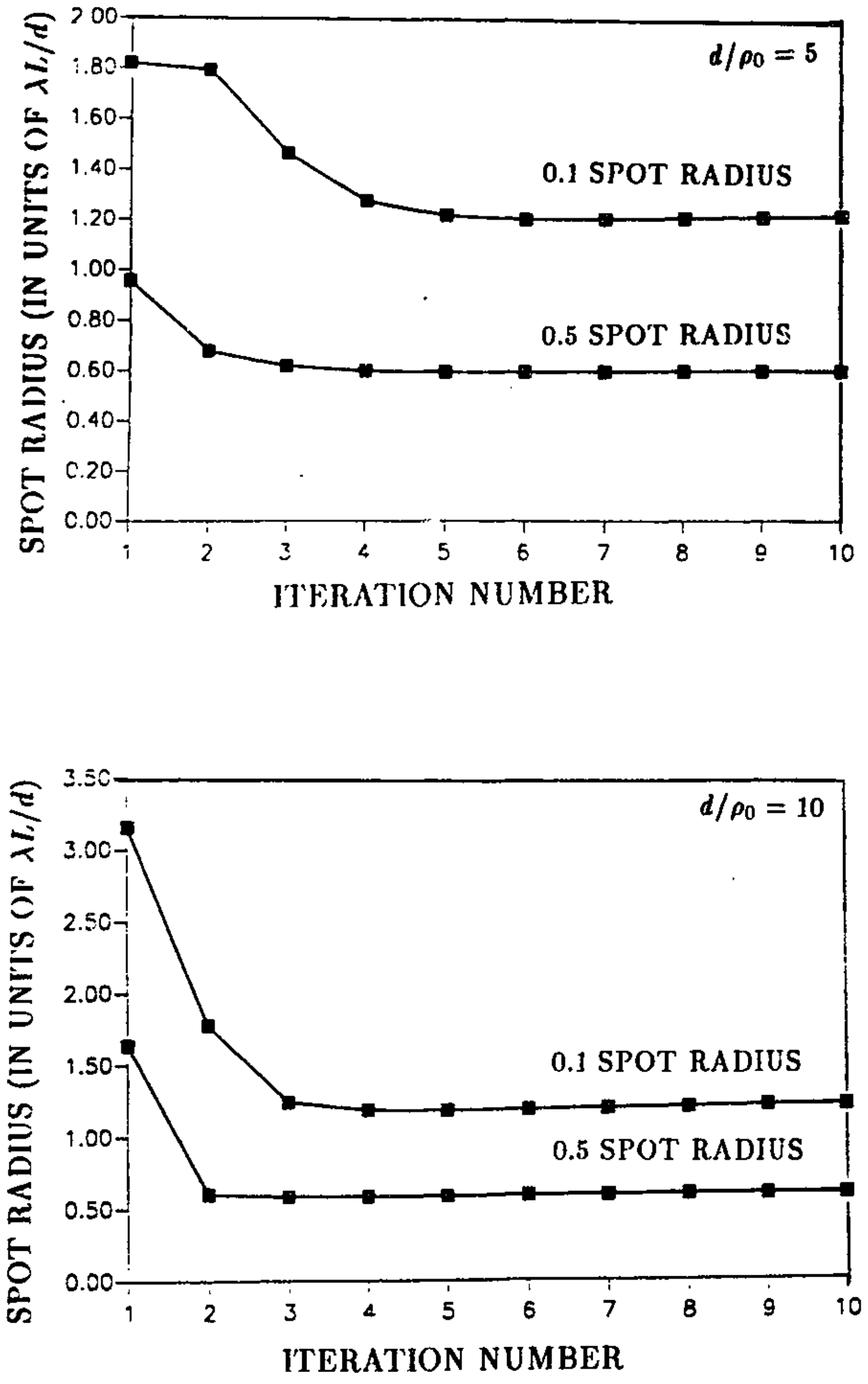

(Figures 5.6a and 5.6b)

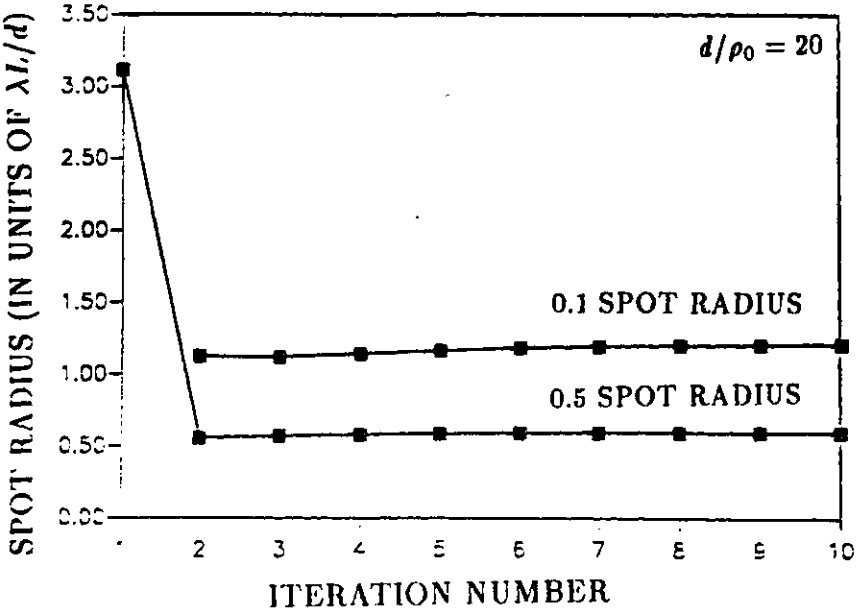

Figure 5.6: Convergence to steady state: spot radius vs. iteration number; $\mathrm{CNR}_{det} = 10.0$, $M = 2$, $N_{eff} = 2000$. (a) $d/\rho_0 = 5.0$, (b) $d/\rho_0 = 10.0$, (c) $d/\rho_0 = 20.0$.

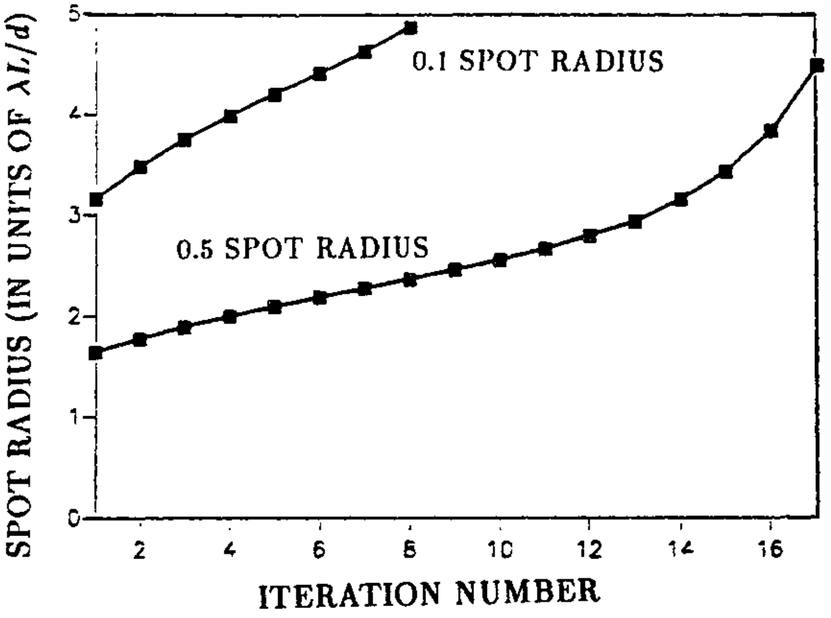

Figure 5.7: Spot radius vs. iteration number for $M = 1$; $\mathrm{CNR}_{det} = 10.0$, $d/\rho_0 = 10.0$, $N_{eff} \to \infty$.

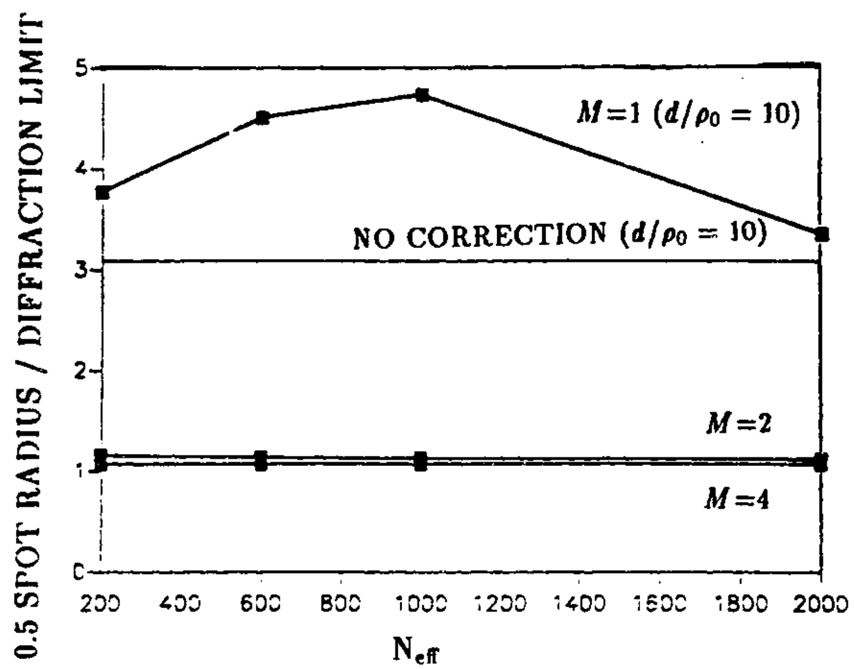

Figure 5.8: Normalized 0.5 spot radius after ten iterations vs. N_{eff}; $CNR_{det} = 10.0$.

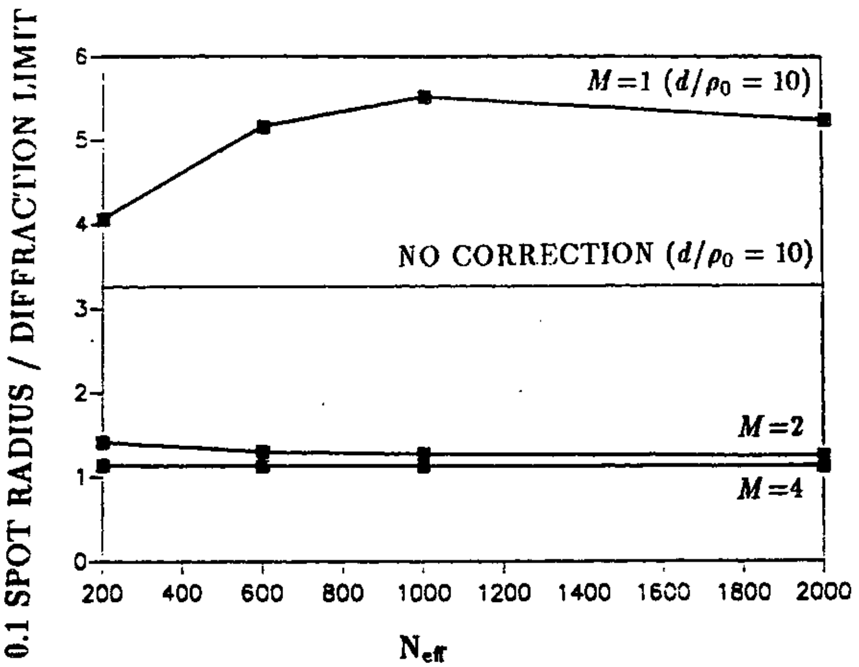

Figure 5.9: Normalized 0.1 spot radius after ten iterations vs. N_{eff}; $CNR_{det} = 10.0$.

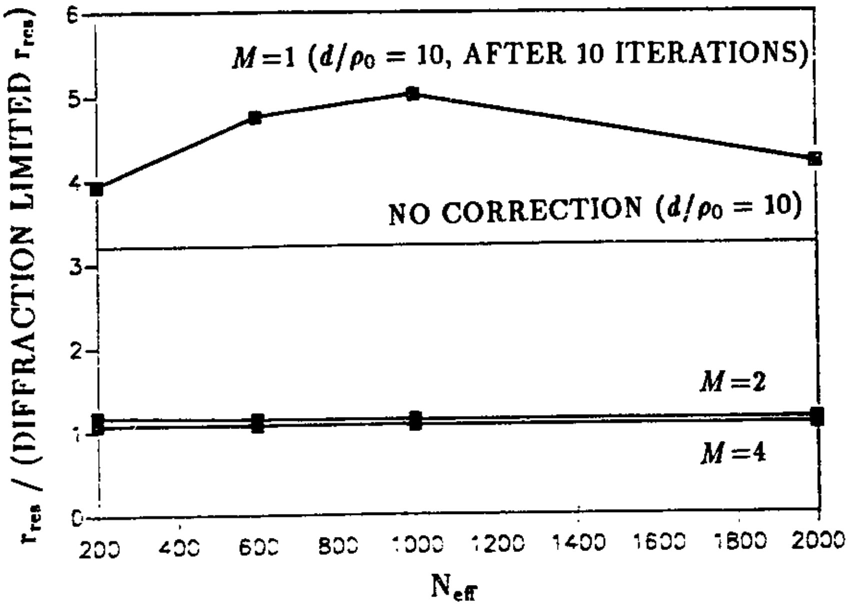

Figure 5.10: Steady-state spatial resolution vs. N_{eff}; CNR$_{det}$ = 10.0.

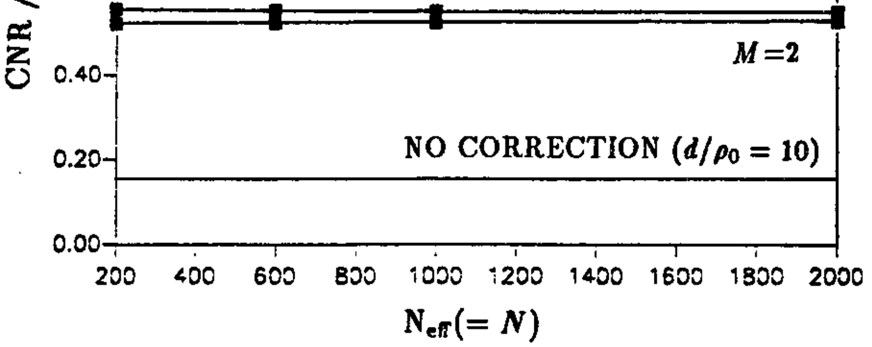

Figure 5.11: Steady-state CNR vs. N_{eff}; infinite target, CNR$_{det}$ = 10.0.

Chapter 6

Discussion of Results

This chapter summarizes and discusses the results obtained in the previous chapters. Section 6.1 summarizes the key results, together with the conditions under which they are applicable. Section 6.2 discusses some technological issues that must be considered in building the adaptive-optical radar system proposed in Chapter 5. Section 6.3 discusses a few possible variations on the system-target scenario considered here, and their effects on the system's performance. Finally, Section 6.4 mentions some areas in which further work could extend or build on the results obtained here.

6.1 Summary of Results

The goal of this thesis was to quantify the degradation in the performance of large aperture coherent laser radars by atmospheric turbulence, and to find the improvement in performance that can be obtained by using adaptive optics to compensate for the effects of turbulence.

Chapter 3 derived the effect of turbulence on the spatial resolution, CNR, and the resolution and accuracy of range and velocity measurements for angle-angle imaging of a spatially-resolved, speckle target. We found that for the turbulence and target scenario assumed here, the spatial resolution, CNR, and range and velocity measurement accuracy are all significantly degraded when the radar aperture-diameter, d, is large compared to the atmospheric coherence length in the radar plane, ρ_0, but the resolution of range and velocity measurements is not significantly affected if target spinning and tilting can be neglected.

The results given here for the spatial resolution, CNR, and range and velocity accuracy all assume that the turbulence through which the transmitted wave travels in the forward path, and the turbulence through which the reflected wave travels in the return path, are statistically independent[1]. All the results given assume that the turbulence is smoothly varying along the propagation path. That is, at spatial wavenumbers of interest, the spectral shape remains constant over the propagation path but the intensity of the fluctuations (represented by $C_n^2(\eta)$) varies slowly along the path [23]. Therefore the turbulence can be said to have the coherence lengths ρ_0 and ρ_0', which are spatially invariant within the radar plane and the target plane, respectively. Furthermore, all the results assume that the target is a speckle target with the spatial and spatial-frequency coherence properties given in Section 2.3, and that the mean-squared target reflectivity is uniform over a target pixel region.

The results given for the resolution and accuracy of range and velocity measurements are based on further assumptions in addition to those mentioned above. These assumptions imply that the temporal fluctuations in the IF signal due to temporal variations in the speckle and turbulence distortions are negligible during a pulse duration or pixel dwell time. In particular, five conditions were assumed in order to ensure that these temporal variations are negligible. Let T denote the pulse duration of a transform-limited pulse or the pixel dwell time for a continuous wave. The first condition is that the multipath pulse spread is small compared to T; this condition is supported by coherence-bandwidth measurements of starlight. The

---

[1] However, it has been shown [13] that when the turbulence in the forward and return paths are identical, the CNR is also degraded when $d/\rho_0 > 1$.

second condition is that $d/v_w \gg T$, where v_w is the component of the wind velocity perpendicular to the propagation path. The quantity d/v_w is the time scale of the IF signal fluctuations due to temporal turbulence fluctuations, using the frozen flow model for temporal turbulence fluctuations. The third condition is that $\rho_0'/v_\perp \gg T$, where $v_\perp$ is the component of the satellite velocity perpendicular to the propagation path. This condition ensures that the turbulence decorrelation due to beam slewing is negligible during time T. The fourth condition is that $d/v_\perp \gg T$; this condition ensures that the speckle decorrelation due to beam slewing is negligible during time T. The fifth condition is that the target does not spin or tilt enough during time T to cause speckle decorrelation. The speckle decorrelates if the target tilt angle is larger than d/L, and therefore the maximum angular rate of the target is $d/(LT)$. In Section 3.3 it was shown that for typical values of d, v_w, ρ_0', $v_\perp$, and T, the second, third, and fourth conditions are satisfied. The fifth condition was assumed to be satisfied; if it is not, then the analysis becomes somewhat more complicated, as is discussed below in Section 6.3.

Chapter 4 derived the radar performance that would be obtained if the turbulence-induced phase distortions in one or both beams are perfectly corrected. We found that if both beams are corrected, the performance is very close to the no-turbulence performance. Even if only one beam is corrected, the spatial resolution is very close to the no-turbulence value. Phase correction on both beams does not completely restore the no-turbulence performance because of scintillation, i.e. the nonzero value of σ_χ^2. However, the value of σ_χ^2 is very small for vertical propagation paths and infrared wavelengths, so scintillation effects are minimal under these conditions.

All the formulas derived in Chapter 4 are valid under the same restrictions that were imposed in deriving the corresponding formulas in Chapter 3. Furthermore, several additional conditions must be met in order for it to be possible in principle to perfectly correct the turbulence-induced phase distortions. In particular, correction of the transmitted wave depends on the reciprocity property of atmospheric turbulence. In order to apply this property to correction of the transmitted wave, the received wave from which the turbulence is measured must travel through the same propagation path, including the same turbulence, as the transmitted wave which is being corrected. Thus, the point-ahead angle $2v_{\perp}/c$ must be smaller than the isoplanatic angle ρ_0'/L to ensure that the turbulence through which the two waves travel is highly correlated. Also, the turbulence must not change between the time the received wave enters the turbulence and the time the transmitted wave leaves it. For a ground-based radar, this condition is met when $2L_a/c < \rho_0/v_w$, where $2L_a$ is the length of the round-trip propagation path through the turbulent atmosphere. When these conditions on the point-ahead angle and the round-trip propagation time through the turbulence are met, the reciprocity property of the turbulence can be used to measure the turbulence information for transmitter correction from a wave received from the point (or coherence area) to which the transmitted wave is directed. However, in order to correct the entire illuminator beam pattern, the spot size on target ($\lambda L/d$ for a perfectly corrected beam) must be smaller than ρ_0'. The issue of how the turbulence information for wavefront correction may be obtained in a radar system is examined in Chapter 5.

The condition for correcting the LO is simpler than the conditions for correcting the transmitted wave. As long as the received wave comes from a single coherence area in the target plane (i.e. the size of the spot on target which gives rise to the received wave is smaller than ρ_0'), the LO can be corrected by applying to it the same turbulence distortion that is in the received wave. This latter condition is satisfied when $\lambda L/\rho_0 < \rho_0'$, the SCA approximation.

If all of the above-mentioned conditions concerning correction of the transmitted and LO waves are met, and if there is a received wave coming from the target from which the turbulence information can be measured, then the results of Chapter 4 show that the performance can nearly be restored to the no-turbulence level. It was shown in Chapter 4, and in the beginning of Chapter 5, that the conditions concerning correction of the transmitted and LO waves are met if the target is a satellite in a circular orbit high above the atmosphere, if the target is at a sufficiently small zenith angle, and if the wavelength is sufficiently large. There may be conditions under which only the LO can be corrected, but the results of Chapter 4 show that even when only one beam can be corrected, the spatial resolution can be restored to close to its no-turbulence value.

The question addressed in Chapter 5 was how to measure the turbulence information necessary for wavefront correction in a radar system when the target is a spatially resolved speckle target. In general, the only available source of such information is the target return. The conditions under which the target return can be used for wavefront correction include all the conditions mentioned in connection with Chapter 4 regarding when correction of the transmitted and LO waves is possible, as well as an additional condition. This condition is that it must be possible to distinguish between the turbulence and speckle distortions in the received wave. It was shown that the received speckle distortions decorrelate more rapidly with wavelength variation than do the received turbulence distortions. Therefore, if a set of wavelengths is transmitted such that the received speckle distortions at the different wavelengths are uncorrelated, but the received turbulence distortions are highly correlated, then averaging the received phase distortions over the different wavelengths suppresses the speckle distortions without impairing measurement of the turbulence distortions.

The structure of a system which transmits such a set of wavelengths was presented, and its performance was derived. Such a system is expected to operate in situations in which d/ρ_0 is close to or greater than 10, since it is in such cases that the turbulence-induced wavefront distortions severely degrade the radar performance. In order for a wavefront correction system to be effective, it must have enough detectors and correction elements to accurately measure and correct the wavefront distortions. When $N \geq 4(d/\rho_0)^2$ this latter condition should be met [55]. However, other studies [57] have shown that even when there are fewer correction elements, a turbulence-distorted image can still be improved to a significant degree. Another condition necessary for effective operation of this multiwavelength radar system is that the CNR per detector per wavelength must be large enough to make useful measurements of the received phase distortions. In this thesis we have taken $\mathrm{CNR}_{det} \geq 10$ to be the necessary condition. Furthermore, the bandwidth of the IF filters must be at least as large as the temporal bandwidth of the turbulence fluctuations, which is of the order of v_w/ρ_0.

The conditions mentioned above regarding d/ρ_0, N, CNR_{det} are necessary for useful and effective operation of the system proposed here. However, some additional conditions were assumed to be met in order to simplify the analysis of the system's performance, and therefore the radar performance results that are given are also based on these conditions. First, it was assumed that the target is spatially resolved by the uncorrected spot size on target, i.e. $d_T > \lambda L/\rho_0$. Second, the local homogeneity of the turbulence, i.e. its spatial stationarity within the radar plane and the target plane, was used to simplify the iteration equations. Third, it was assumed that the relative separation among the wavelengths is small—and it must be in order for the turbulence distortions at all of the wavelengths to be correlated—in order to simplify the numerical evaluation of the radar performance.

The analysis of the performance of the multiwavelength radar system, based on all of the assumptions and conditions mentioned above, shows that when both beams are corrected, the spatial resolution and CNR are quite close to the no-turbulence values for system parameter values that are expected to prevail in the operation of such a system. If only one wavelength is used, the CNR is slightly larger than the no-turbulence value, and the spatial resolution is worse than turbulence-limited. It was argued that the spatial resolution and CNR results indicate that the range and velocity measurement accuracy are also close to the no-turbulence values.

The results obtained in Chapter 5 show that under certain conditions, the free-space performance advantage of large aperture coherent laser radars can also prevail in the presence of turbulence, if adaptive optics are used to correct the turbulence-induced wavefront distortions. The CNR and the range and velocity accuracy can also be improved in other ways besides the use of adaptive optics. For example, the CNR could be increased without using adaptive optics if the transmitted power is increased. However, the IF signal fluctuations would still degrade the range and velocity measurement accuracy. Alternatively, when $d \gg \rho_0$, array detection can improve the CNR and the range and velocity accuracy. Although increasing the transmitted power or using array detection would improve the CNR and the range and velocity accuracy, these approaches would not restore the no-turbulence performance. In order to obtain the no-turbulence CNR and range and velocity accuracy, the IF signal fluctuations must be continually compensated, e.g. by using adaptive optics. Actually, the no-turbulence CNR and range and velocity accuracy could be obtained with a single-wavelength radar system by simply correcting the LO wavefront to match the received wavefront.

The new horizon opened up by this multiwavelength radar system is in achieving very high spatial resolution with angle-angle imaging. To achieve high spatial resolution with angle-angle imaging in the absence of turbulence, the wavelength must be decreased and/or the aperture diameter must be increased. Either of these changes would make the turbulence effects on the spatial resolution even more severe, and therefore the spatial resolution could not be improved beyond a certain value[2]. The only way to achieve a better spatial resolution than this value in angle-

---

[2] The turbulence-limited spatial resolution is proportional to $\lambda^{-1/5}$, which worsens very slowly

angle imaging is to decrease the wavelength and/or increase the aperture size, and also to use adaptive optics to compensate for the turbulence-induced wavefront distortions. In general, the only source of the turbulence information necessary for wavefront correction in a radar system is the target return, but if the target is a spatially resolved speckle target, then the speckle and turbulence components of the received wavefront distortions must be separated. Thus, a radar system with adaptive optics which can separate the turbulence from the speckle, such as the multiwavelength radar system presented here, must be used in order to achieve very high spatial resolution in angle-angle imaging of a speckle target.

6.2 Technology for System Implementation

This section discusses the feasibility of constructing the multiwavelength radar system proposed here, considering the types of components that can be built using available technology. Most of the parts of the system have already been used in laser radar and/or adaptive optics systems, with the exceptions of the laser or lasers used to generate the multiwavelength transmitted beam, and the wavefront correction and measurement arrays of a few hundred elements. However, in one recent experiment [58], a phase-conjugate adaptive optics system with a 69-actuator deformable mirror was constructed and used for wavefront compensation in a laboratory experiment. Further work is under way to develop adaptive optics systems with even larger numbers of actuators. Thus, construction of adaptive optics systems with 100 or more actuators should be feasible in the not-too-distant future.

The part of the multiwavelength radar system which is focused on in this section is the laser or lasers used to generate the multiwavelength transmitted beam. As mentioned in the beginning of Chapter 5, the fractional separation between each

---

with decreasing wavelength, but decreasing the wavelength still cannot *improve* the spatial resolution in the turbulence-limited regime the way it can in the absence of turbulence.

pair of wavenumbers must be at least 0.016 (when $\sigma_h = 10\lambda_{av}$ at $\lambda_{av} = 10\,\mu\text{m}$) to give uncorrelated received speckle patterns, but the fractional separation between the largest and smallest wavenumber must be less than 0.05 (for the nighttime turbulence profile used here) to give correlated received turbulence distortions. Furthermore, if the system is to give the radar performance described in Sections 5.3 and 5.4, then the power transmitted at each wavelength must be in the vicinity of 100 Watts, assuming the rest of the parameter values of Table 5.3. There are three types of lasers which emit infrared light at wavelengths which are not strongly absorbed by the atmosphere, which can put out on the order of 100 Watts in cw operation, and for which the SCA approximation is valid. (It is not valid for wavelengths of about $1\,\mu\text{m}$ or shorter for the $C_n^2(\eta)$ profiles used here and for vertical propagation through the atmosphere to an altitude of 100 km or higher.) These lasers are, in order of increasing wavelength, deuterium flouride (DF), carbon monoxide (CO), and carbon dioxide (CO_2). The suitability of each of these types of lasers for use in the system presented here will now be discussed.

The DF laser emission lines range from approximately $3.6\,\mu\text{m}$ to $4.2\,\mu\text{m}$. The wavelengths and relative powers of the emission lines are shown in Figure 6.1a. The laser can be made to emit only a single line by placing a wavelength-dispersive element, such as prism or a diffraction grating, within the laser cavity [59, Chapter 4]. If the desired set of wavelengths cannot be simultaneously extracted from a single laser, more than one laser would have to be used. The maximum single-line power from a commercial DF laser is 25 Watts, according to a book published in 1986 [59, Chapter 11], and custom-built laboratory lasers and military demonstration systems have produced thousands of times more power [59, Chapter 11]. The atmospheric transmission at the DF wavelengths is good. On the other hand, the frequency stability of DF lasers is generally not good, and line control is difficult [60]. Also, large amounts of power are required to operate a cw DF laser [59, Chapter 11]. Thus, one or more DF lasers could in principle be used in the multiwavelength radar system, but some technological obstacles would need to be overcome.

The CO laser emission lines range from approximately $4.8\,\mu$m to $6\,\mu$m. The wavelengths and relative powers of the emission lines of a particular CO laser are shown in Figure 6.1b. The CO laser can emit high power levels [59, Chapter 16]. For example, the laser whose output spectrum is shown in Figure 6.1b emitted a total power as large as 940 Watts. CO lasers also have good frequency stability [60]. On the other hand, most of the lines emitted by a CO laser, i.e. those whose wavelengths are $5\,\mu$m or longer, are strongly absorbed by water vapor in the atmosphere [62]. However, supersonically cooled CO lasers, such as the one whose output spectrum is shown in Figure 6.1b, operate on transitions between low vibrational levels, which occur at wavelengths below $5\,\mu$m [61]. Thus, it may be possible to use one or more CO lasers in the multiwavelength radar system.

The CO_2 laser emission lines range from approximately $9\,\mu$m to $11\,\mu$m. The wavelengths and energies of the emission lines of a pulsed CO_2 laser are shown in Figure 6.1c. Numerical values of the CO_2 laser lines have been tabulated for several different CO_2 isotopic species [63]. CO_2 lasers can emit very high powers—commercially available CO_2 lasers can put out powers as high as 15 KWatt [59, Chapter 10]. CO_2 lasers which put out cw beams with a power of about 100 Watts must operate at low pressures, in which case the laser puts out a narrow range of wavelengths [60]. Thus, a different laser would have to be used for each transmitted wavelength in the multiwavelength radar system. The different wavelengths may be obtained from different lines of lasers with the same isotope (although bigger lasers would be required for the weaker lines) or they may be obtained from one or more different lines of lasers with different isotopes. The beams from the different lasers could be combined using a grating. The atmospheric transmission of CO_2 laser wavelengths is good, and they have already been used extensively for laser radars.

To sum up, each of three types of lasers mentioned above, i.e. DF, CO, and CO_2, may potentially be used for a multiwavelength radar system of the type described here. The DF laser does not have good stability, and most of the CO lines are strongly absorbed by the atmosphere, so at present the CO_2 laser seems to be the most promising for this application. It appears from the wavelength spectra cited here that $M = 2$ or $M = 3$ could be achieved for the nighttime turbulence profile used here (i.e. $\Delta k/k_{av} \geq 0.016$ and $|k_{max} - k_{min}|/k_{av} \leq 0.05$) with each of the three types of lasers, but it may not be possible to achieve $M = 4$ due to the particular spacings of the laser lines. For the daytime turbulence profile used here, and for the assumed value of σ_h, (i.e. $100\,\mu$m) M cannot be larger than 2, and $M = 2$ can clearly be achieved with these types of lasers.

The remaining component of the transmitter section of the multiwavelength radar, besides the laser(s) and possibly a grating to combine the laser beams if there are more than one, is the wavefront correction device for the transmitted wave. Wavefront correction devices have been extensively used in adaptive optics applications for turbulence compensation [19]. In this radar system the wave impinging on the wavefront correction device would have high power—a few hundred Watts—which may restrict the types of devices that may be used for wavefront correction. However, adaptive optics, e.g. deformable mirrors, have been proposed [65], and their effectiveness has been tested [66,67], for compensation of wavefront distortions resulting from thermal blooming. These tests were done in a laboratory, and the laser power was just a few Watts. However, it is also of interest to compensate for thermal blooming in the atmosphere, which occurs with laser powers much larger than a few hundred Watts. Thus, the type of wavefront correction devices that would be used to compensate for thermal blooming in the atmosphere may also be usable for correction of the transmitted wave in the multiwavelength radar system. (One technique for adaptive phase correction of high-power laser beams is described in Reference [58].)

Note that the multiwavelength radar system proposed here is not expected to be faced with thermal blooming. This expectation is based on consideration of the thermal distortion parameter N_T. When N_T is much smaller than 1, the peak irradiance on target is negligibly affected by thermal blooming [64]. Using an approximate formula for N_T [64] for the case of a transmitted power of 400 Watts, a transverse wind velocity of the order of 1 m/sec, a $1/e$ transmitted-beam radius of the order of 1 meter, and a laser wavelength in the range of the laser wavelengths mentioned here, we find that the thermal distortion parameter N_T is much smaller than 1. The approximations on which this formula is based are that the transmitted beam is strongly focused, that there is no beam slewing or beam jitter, and that the absorption number, αL, is much less than 1. In the case of the radar system mentioned here, the transmitted beam will most likely *not* be strongly focused, and there *will* be beam slewing, but both of these effects make thermal blooming even less significant. Since the transmitted wavelength would be chosen in such a way as to minimize atmospheric absorption, it is reasonable to assume that αL is much less than 1 in evaluating the effect of thermal blooming on the transmitted beam.

The components in the receiver section of the multiwavelength radar system are all standard components of adaptive optics and/or laser radar systems, except for the detector array of several elements. However, individual detectors exist for IR wavelengths, so there does not seem to be a fundamental reason why large arrays of such detectors could not be assembled. Also, the laser power levels in the receiver section should not impose any unusual restrictions on the types of devices that may be used. Thus, it seems possible to construct the receiver section from devices that are presently in use.

In conclusion, it should be possible to construct the multiwavelength radar system proposed here, using technology that is either available or under development in the areas of lasers, adaptive optics, and laser radar components.

6.3 Variations on the System-Target Scenario

In this thesis, a particular system-target scenario has been assumed, which includes assumptions about the radar operation, the target characteristics, and the propagation path between the radar and the target. It would also be of interest to find the radar performance results given here for other system-target scenarios similar to the one assumed here. This section briefly addresses how the analysis and results given here would be modified in three different variations on the system-target scenario considered here. The first variation considered is the effect on radar performance if, in the multiwavelength radar system of Chapter 5, the phase correction applied to the received wave at wavelength λ_m is $\exp(-i\hat{\phi}_n(m))$ instead of $\exp(-i\frac{1}{M}\sum_{m=1}^{M}\hat{\phi}_n(m))$. In other words, what is the effect of not using speckle averaging in the LO correction? The second variation considered is the effect on radar performance if the target is spinning or tilting in such a way that the received speckle distortions decorrelate during a pulse duration or pixel dwell time. The third variation considered is the effect on radar performance if the target is a glint target, instead of a speckle target as was assumed here.

6.3.1 Correction of the LO without Speckle Averaging

In the multiwavelength radar system proposed in Chapter 5, the same phase correction is applied to both the transmitted and the LO (or equivalently, to the IF signal). This phase correction is the sum of the turbulence phase and the wavelength-averaged speckle phase, which includes the shot noise effects. In the limit of an infinite number of wavelengths, the wavelength-averaged speckle phase would have zero variance, and this correction would be the best phase correction to apply to compensate for the turbulence effects. For finite values of M, the analysis of Section 5.4 shows that this correction gives a spatial resolution very close to the diffraction-limited value because of the speckle averaging in both the transmitted-wave and LO correction. However, the CNR is largest for $M = 1$, because in that case there is no speckle averaging in the LO correction, so that the speckle and turbulence distortions in the corrected LO wave most closely match the speckle and turbulence distortions in the received wave.

Now suppose that for all values of M, the phase correction applied to the IF signal $\mathbf{r}_n(m)$ is $\exp(-i\hat{\phi}_n(m))$ instead of $\exp(-i\frac{1}{M}\sum_{m=1}^{M}\hat{\phi}_n(m))$ as is done in the system of Figure 5.1. Then the CNR would be larger than the results shown in Figure 5.11, and for large CNR_{det} (e.g. $\mathrm{CNR}_{det} \geq 10$) the CNR would be larger than the no-turbulence value. On the other hand, the back-propagated corrected LO wave would have a larger spot size than it would with the LO correction of Figure 5.1, so that the spatial resolution would be worse than the results shown in Figure 5.10. However, it would not be much worse, because the illuminator beam pattern would still be the same as it is in the system of Figure 5.1, and it was shown in Section 4.1 that the spatial resolution when only one beam is corrected is only slightly (a factor of $\sqrt{2}$) worse than the spatial resolution when both beams are corrected, in the large aperture limit. Another disadvantage of the LO correction mentioned in this section is that more equipment would be required in the radar system, since a separate N-element phase correction array would be required for the IF signal at each of the M wavelengths.

To summarize, the LO correction mentioned in this section would give a better CNR than the LO correction of the Figure 5.1 system, at the expense of a slightly worse spatial resolution and a more complex receiver section in the radar. Depending on the particular application of the radar system, one type of LO correction may be preferable to the other type.

6.3.2 Spinning or Tilting Target

Throughout this thesis it has been assumed that the target does not spin or tilt in such a way as to cause the received speckle distortions to decorrelate during a pulse duration or pixel dwell time. In this section we briefly consider the implications for system performance if this is not the case. We shall assume here that the target reflectivity has the following correlation function

$$\begin{aligned}\langle \mathbf{T}(\vec{\rho}_1{}'; k_1, t_1)\mathbf{T}(\vec{\rho}_2{}'; k_2, t_2)^*\rangle &= \lambda_{av}^2 \delta(\vec{\rho}_1{}' - \vec{\rho}_2{}')\mathcal{T}(\vec{\rho}_1{}')e^{-4(\rho_1'/d_T)^2} \\ &\quad e^{-2(k_1-k_2)^2\sigma_h^2}\, e^{-(t_1-t_2)^2/t_c^2}, \end{aligned} \qquad (6.1)$$

where t_c is the coherence time of the speckle target reflectivity.

The spatial resolution is unaffected, since it depends only on the spatial characteristics of the two target-plane beam patterns. However, the CNR would be reduced because the speckle fluctuations would broaden the bandwidth of the target return so that not all of its energy would pass through the IF filter. In particular, the CNR would be multiplied by a reduction factor given by

$$(P_T/E_T)^2 \int dt_1 \int dt_2 \left|\mathbf{s}\left(t_1 - \frac{2L}{c}\right)\right|^2 \left|\mathbf{s}\left(t_2 - \frac{2L}{c}\right)\right|^2 e^{-(t_1-t_2)^2/t_c^2}, \qquad (6.2)$$

which approaches 1 as $t_c \to \infty$. The range and velocity accuracy would also be degraded, although a quantitative description of the degradation is not so simple to obtain because the results in the presence of turbulence can no longer be obtained from the no-turbulence results by making the substitution CNR → $\text{CNR}_T \cdot \boldsymbol{x}$. Qualitatively, it can be seen that the accuracy would be degraded because $\ell(\cdot)$ is broadened, so that its peak is reduced. This reduction of the peak makes the peak of $|\ell(\cdot) + \mathbf{n}(\cdot)|^2$, from which the range or velocity estimate is derived, more strongly affected by the shot noise component $\mathbf{n}(\cdot)$, as discussed in Section 3.4. Perfect correction of the turbulence phase distortions in the transmitted and/or LO beams would still improve the spatial resolution, CNR, and range and velocity accuracy, but the CNR and range and velocity accuracy would not approach their no-turbulence results at $t_c \to \infty$ due to the effects mentioned above.

If the target is spinning or tilting in such a way as to cause the received speckle distortions to decorrelate during a pulse duration or pixel dwell time, then an adaptive optical radar system whose structure is simpler than that given in Figure 5.1 may be used. In particular, the received speckle and turbulence distortions can be separated when only one wavelength is transmitted. In this case, the IF filter bandwidth in the receiver section would be increased so that it would be large enough to pass the target return in an undistorted way. The phase of the IF signal would be measured from the IF filter output, and this phase would be low-pass filtered in order to reduce its speckle component.

The system described above has some advantages compared to the system of Figure 5.1. First, its structure is much simpler, since only one wavelength is transmitted. Second, important information about the target may be obtained from measurement of its rotation rate. On the other hand, the increased IF filter bandwidth leads to a lower phase-measurement CNR, which would impair the quality of the phase measurements used for wavefront correction unless the transmitted power is sufficiently increased.

6.3.3 Glint Target

In this thesis it was assumed that the target is a speckle target, since many targets have the characteristics of a speckle target when illuminated by temporally coherent light at optical or IR wavelengths. Furthermore, the problem of compensating for the turbulence-induced distortions is more difficult in the case of a speckle target because of the necessity of distinguishing between the turbulence and speckle distortions in the target return. However, it would also be of interest to find the turbulence-induced radar performance degradation and the performance improvement that can be obtained with wavefront correction in the case of a glint target.

A glint target is a target which reflects the incident wave in a specular way, without distorting the wavefront. To give a brief and simple description of the radar performance in the case of a glint target, we shall assume here that the target has only a single region which gives a specular reflection of the incident beam pattern back toward the radar, that the area of this region is much smaller than the illuminator and BPLO spot areas on target and much smaller than the target-plane turbulence coherence area, and that the center of this region lies on the axis of propagation of the transmitted and BPLO beams from the radar to the target. Thus, the target reflectivity can be written as

$$\mathrm{T}(\vec{\rho}\,') = \sqrt{\frac{\sigma\lambda^2}{4\pi}}\,\delta(\vec{\rho}\,')e^{i\theta}, \tag{6.3}$$

where σ is the radar cross-section of the glint, and θ is a uniformly distributed random variable on $[0, 2\pi]$, which models the uncertainty in the location of the target plane on the scale of the radar wavelength [11]. Such a target is clearly spatially unresolved, so the spatial resolution need not be considered.

Assuming that the receiver front end model is that of Section 2.4, the CNR in the absence of turbulence is given by [39]

$$\mathrm{CNR}_0 = \frac{\eta P_T \epsilon_{opt}}{h\nu_0 B}\frac{G_T}{4\pi L^2}\frac{\sigma A_R}{4\pi L^2}e^{-2\alpha L} \tag{6.4}$$

in the absence of turbulence for a continuous wave, where the transmitted and LO beam patterns are given by Eq. 3.1, and P_T/B would be replaced by E_T for a pulsed wave. In Eq. 6.4, $G_T \equiv e^{\alpha L}4\pi L^2|\xi_t(\vec{0})|^2$ is the transmitter antenna gain, and $A_R \equiv e^{\alpha L}(\lambda L)^2|\xi_{lo}(\vec{0})|^2$ is the effective heterodyne-detection glint-target mixing area[3] [39]. Thus, term $P_T G_T e^{-\alpha L}/(4\pi L^2)$ represents the illuminator beam intensity

---

[3] Note that the definitions of G_T and A_R include the term $e^{\alpha L}$. This term is included in order to cancel the $e^{-\alpha L}$ term in the mean-squared target-plane beam patterns, so that the atmospheric absorption and attenuation term appears explicitly in the CNR formula.

	$\mathrm{CNR}/\mathrm{CNR}_0$
neither beam corrected	$\left(1+\frac{d^2}{8\rho_0^2}\right)^{-2}$
one beam corrected: lower bound	$e^{-\sigma_\chi^2}\left(1+\frac{d^2}{8\rho_0^2}\right)^{-1}$
upper bound	$\left(1+\frac{d^2}{8\rho_0^2}\right)^{-1}$
both beams corrected: lower bound	$e^{-2\sigma_\chi^2}$
upper bound	1

Table 6.1: CNR with Perfect Turbulence Phase Correction

over the glint region, and multiplying this term by σ gives the power reflected from the glint. The term $P_T G_T e^{-\alpha L}/(4\pi L^2) \cdot \sigma e^{-\alpha L}/(4\pi L^2)$ gives the received intensity incident on the radar aperture, and multiplying this term by A_R gives the amount of target-return power received in the heterodyne detection process. The CNR reduction factors due to turbulence for the cases of no correction, one beam phase-corrected, and both beams phase-corrected when the turbulence in the forward and return paths are independent are shown in Table 6.1. It can be seen from Eq. 6.4 and Table 6.1 that the CNR, whose no-turbulence formula is proportional to d^4, saturates for large apertures in the absence of correction, because the illuminator beam irradiance and the effective heterodyne-detection mixing area both saturate for large d. When one beam is corrected, either the illuminator beam irradiance or the effective heterodyne-detection mixing area saturates for large d, but the other quantity increases with increasing d. Therefore, the CNR for one beam corrected does not approach the no-turbulence value, but it does continue to improve as d increases. When both beams are phase-corrected, the CNR is very close to its no-turbulence value when σ_χ^2 is small, because both the illuminator beam irradiance and the effective heterodyne-detection mixing area are close to what they would be in the absence of turbulence. Thus, turbulence has a very severe effect on the glint-target CNR when neither beam is corrected. If one beam is corrected, the CNR can be considerably improved, but both beams must be corrected to approach the no-turbulence CNR.

The resolution of range and velocity measurement depends on the temporal characteristics of the target return, as discussed in Section 3.3. If the glint target is in a circular orbit around the earth at an altitude of at least 100 km, then the discussion of Section 3.3 shows that the resolution would not be affected by turbulence for pulse durations and pixel dwell times in the range of nanoseconds to tens of microseconds. The accuracy of range and velocity measurements can be obtained from the no-turbulence results as was done in Section 3.4. The no-turbulence anomaly probability and Cramer-Rao bound for a glint target can be found by using the given statistical properties of the target return and the shot noise, using the same method that was used to find the corresponding speckle-target results [18]. For a glint target, the no-turbulence probability of anomaly is

$$\Pr(A) = 1 - e^{-\mathrm{CNR}} \int_0^\infty dv\, e^{-v} I_0(2\sqrt{\mathrm{CNR} \cdot v})(1 - e^{-v})^{N_{bin}-1}, \tag{6.5}$$

where I_0 is the zeroth-order modified Bessel function of the first kind. In the absence of turbulence, the probability of anomaly for a glint target is much smaller than that for a speckle target, because the target return does not have fading in the glint-target case, while speckle causes fading in the target return in the speckle-target case. The Cramer-Rao bound for the mean-squared range or velocity estimation error in the absence of turbulence is

$$\text{CR bound} = \left\{ \begin{array}{c} z_{res}^2 \\ v_{res}^2 \end{array} \right\} \cdot 1/(16\,\mathrm{CNR}), \tag{6.6}$$

where the top row is for range measurements and the bottom row is for velocity measurements, and z_{res} and v_{res} are given by Eqs. 3.7 and 3.9, respectively. For large values of CNR, this Cramer-Rao bound is approximately equal to the Cramer-Rao bound for a speckle target. The probability distributions $p_x(X)$ for the cases of no correction, one beam corrected, and both beams corrected are the same as the formulas used in Sections 3.4 and 4.3. However, the formula for x in Eq. 3.24 is now exact—it is no longer an approximation when using the target reflectivity model of Eq. 6.3. The range and velocity accuracy can be found from Eqs. 6.5, 6.6, 3.20, and the $p_x(X)$ distributions of Sections 3.4 and 4.3, and it is plotted in Figures 6.2a and 6.2b for the case of no correction. In this case, the normalized range and velocity accuracy in slightly worse for a glint target than it is for a speckle target, for a fixed value of CNR_0 and for $d/\rho_0 = 5$ or 10. The reason is that although the no-turbulence accuracy is much better for a glint target, the CNR for a glint target is much more strongly degraded by turbulence than is the CNR for a speckle target. Also, the probability of anomaly is much more strongly degraded by turbulence for a glint target, because turbulence introduces fading into the target return. The accuracy for the case in which one beam is corrected is plotted in Figures 6.2c and 6.2d. In this case, the range and velocity accuracies improve significantly for $d/\rho_0 = 5$ or 10, to a large extent because of the significant improvement in CNR that can be obtained by correcting only one beam. The accuracy for the case in which both beams are corrected is plotted in Figures 6.2e and 6.2f. In this case, the range and velocity accuracies are very close to the no-turbulence value, as it is in the case of a speckle target. Thus, the glint-target range and velocity accuracies, as well as the CNR, are very strongly degraded by the turbulence-induced wavefront distortions, but these performance measures can be significantly improved by correcting only one beam, and the no-turbulence performance can nearly be restored by correcting both beams.

The design of a wavefront correction system is much simpler in the case of a glint target than it is in the case of a speckle target, because now the only wavefront distortions in the target return are the turbulence distortions which we want to measure, and the SCA approximation is automatically satisfied since the glint size is smaller than ρ_0'. Thus, the adaptive-optical radar system need only transmit one wavelength. It would measure the phase distortion in the target return, and apply the same distortion to the LO beam for LO correction. If the point-ahead condition of Eq. 5.1 is satisfied, then the complex conjugate of the phase distortion in the target return is applied to the transmitted wave for transmitted-wave correction. If the size of the detectors and correction elements is small compared to the coherence length of the wavefront distortions, and if the IF filter bandwidth is larger than the temporal bandwidth of the turbulence, then the main limitation on the wavefront-correction system's performance would be the effect of shot noise on the measurement of the phase distortion in the received wave. Another potential limitation on the system's performance is that if the target is moving with respect to the radar, it may not continue to behave as a glint target as it changes its position relative to the radar. At any rate, it should be quite feasible to build an adaptive-optical radar system to compensate for turbulence effects in a large-aperture radar in the case of a glint target. In fact, a tilt-tracking radar for a CO_2 laser radar with a moderate sized aperture (1.2 meters) has already been demonstrated at the Firepond facility of the MIT Lincoln Laboratory [2].

6.4 Topics for Further Investigation

The research presented in this thesis can be extended in several ways. Some of these ways concern the relaxation of certain assumptions made here in order to simplify the analysis, and other ways concern the analysis of other types of radar systems which compensate for the effects of turbulence.

One issue to consider is the effectiveness of wavefront correction using information derived from the target return when the SCA approximation ($\lambda L/\rho_0 < \rho_0'$) is not satisfied, since it is not satisfied in certain cases of interest. For example, this condition is not satisfied for sufficiently short wavelengths—for the $C_n^2(\eta)$ profiles used here it begins to be violated at about $\lambda = 1\,\mu$m. Also, for a horizontal path near the ground longer than a few kilometers it may not be satisfied. It may be that applying the complex conjugate of the turbulence phase distortion in the target return as a phase correction to the transmitted wave could still reduce the spot size of the illuminator beam pattern to some degree. In that case, the adaptive-optical radar system proposed in Chapter 5 would still give good performance in steady state if the spot size of the illuminator beam pattern decreases from one iteration to the next.

Another issue to consider is the effect of the finite size of the detectors and correction elements on the measurement and correction of the turbulence-induced phase distortions. In this thesis it was assumed for simplicity that the detectors and correction elements are small enough that the turbulence-induced phase distortions are spatially constant over their extent. This issue is of particular interest because of the tradeoff between the parameters N and CNR_{det}. The larger N is, the better is the approximation that the phase distortions are constant over each detector and correction element, and the more effective the phase correction can be. On the other hand, the larger N is, the less target-return power is incident on each detector, reducing CNR_{det}, and the more the measurement of the phase distortion in the received wave is degraded by shot noise.

It would be of interest to investigate other ways to distinguish between the speckle and turbulence distortions in the target return—other ways may give larger values of M or may be easier to implement than the transmission of multiple wavelengths. For example, consider a case in which the target is spinning fast enough that the correlation time of the speckle phase distortion in the target return is much smaller than the pixel dwell time (for a continuous wave), and the pixel dwell time is shorter than the turbulence coherence time ρ_0/v_w. In such a case, the speckle component of the received phase distortion can be suppressed by averaging the received phase distortion over different subintervals of the pixel dwell time, such that the speckle distortions during two different subintervals are statistically independent. (For a pulsed wave, a pulse would be sent for each subinterval.) The value of M would be the ratio of the pixel dwell time to the correlation time of the speckle phase distortions in the target return.

Another issue of interest is analysis of the performance of an adaptive-optical radar system which corrects only the tilt component of the turbulence phase distortions. This issue is of interest because for values of d/ρ_0 less than to slightly greater than one, the turbulence phase distortion over the aperture region is mainly tilt. Also, in a tilt correction system N may be as small as 4. Thus, it would be of interest to design and analyze the performance of a radar system with a moderate sized aperture, which measures the turbulence-induced phase tilt from the target return of a spatially resolved speckle target.

It would also be of interest to find the radar performance that can be obtained by using nonadaptive array detection, because in some cases it may not be feasible or economical to use an adaptive-optical radar system. For example, the IF signal derived from the target return may not be strong enough, for various reasons, to measure the phase distortion incident on each part of the aperture. However, when heterodyne detection is used and the received wave is not spatially coherent over the aperture region, the performance can be improved with array detection, even if no adaptation is done. Thus, the heterodyne-detected signals from each element of the array could be incoherently combined in some predetermined way (e.g. sum the squares) to get better performance than that obtained by simply using one large aperture. Various kinds of array or diversity detection could be examined, and their performance compared to that of a single large aperture.

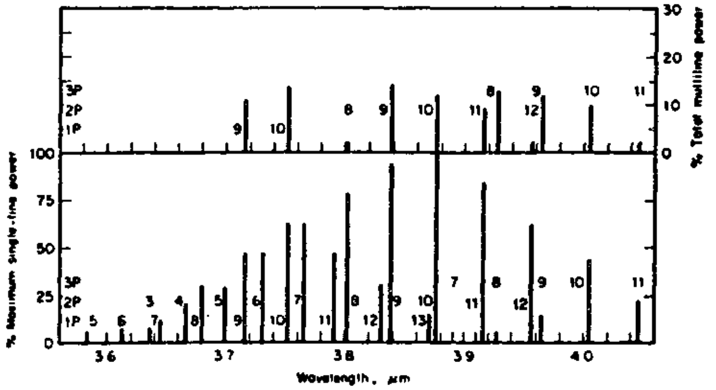

DF emission lines from a continuous-wave chemical laser.

(Courtesy of Helios Inc.)

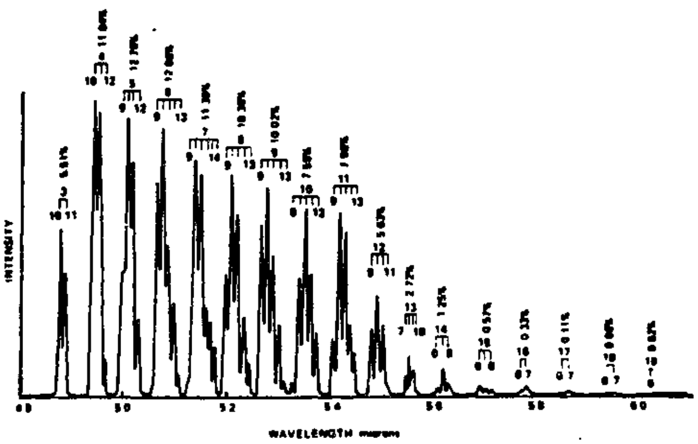

Output spectrum of the laser Gas mixture was 93.9 percent He, 5.9 percent CO, and 0.2 percent O_2 at a total discharge pressure of 390 torr. The input energy was 0.17 eV/CO and the total output power was 384 W which corresponds to an electrooptical efficiency of 9.0 percent. The percentage of the total power occurring on all lines of a band is given above the upper state vibrational quantum number of that band. The extremes of the lower state rotational quantum numbers are given below the line position markers.

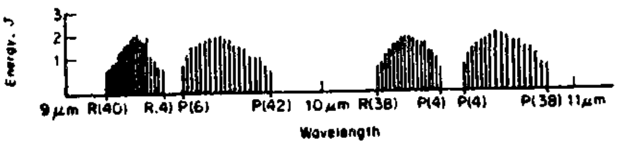

Spectrum of wavelengths produced by a transversely excited atmospheric pressure CO_2 laser, showing pulse energy emitted at each line in single-line operation by a commercial laser *R* and *P* denote rotational sublevels for each of the two main vibrational transitions of the carbon dioxide laser. *(Courtesy of Lumonics Inc.)*

Figure 6.1: Laser emission lines for three types of lasers. (a) DF, from Reference [59], (b) CO, from Reference [61], (c) CO_2, from Reference [59].

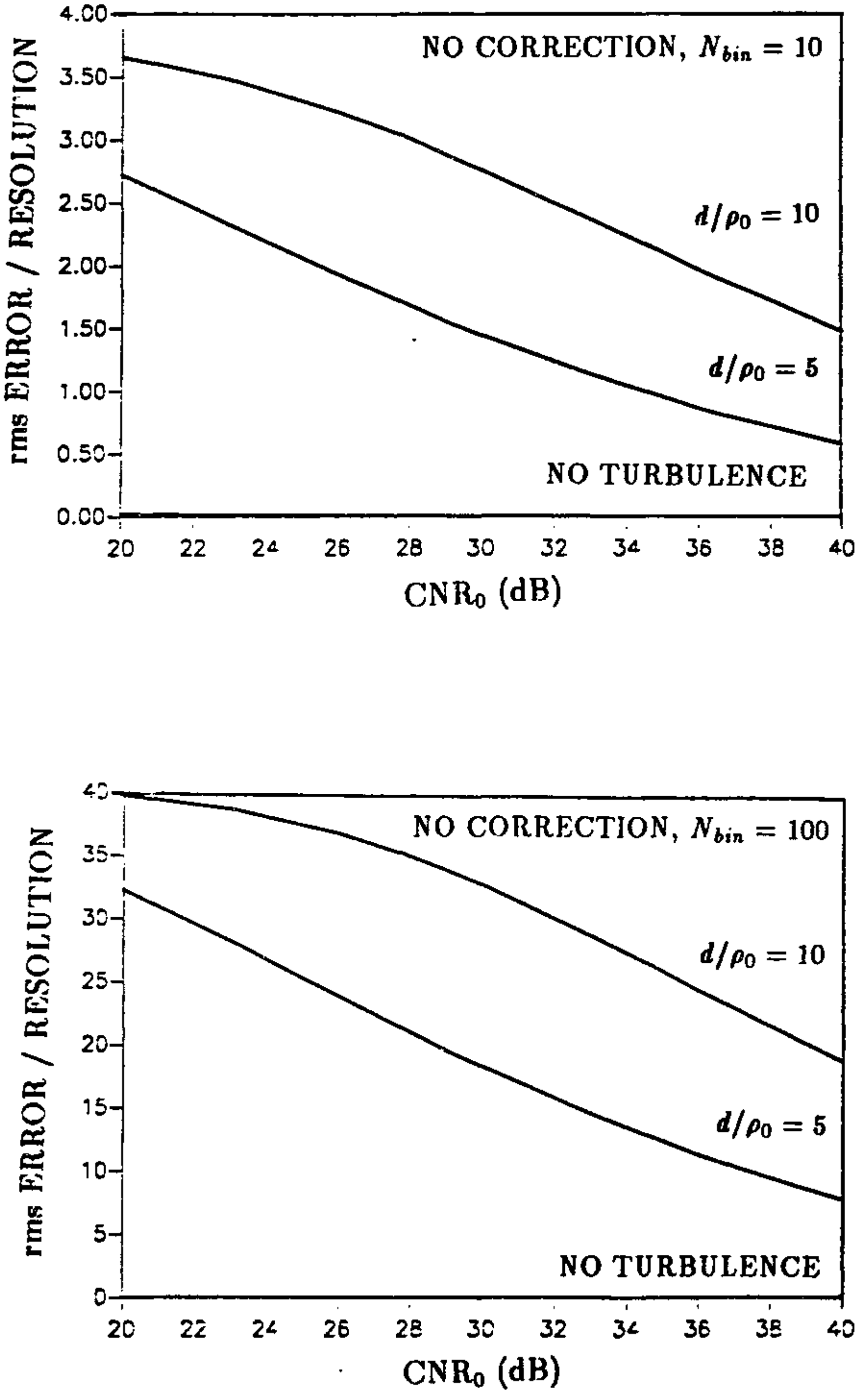

(Figures 6.2a and 6.2b)

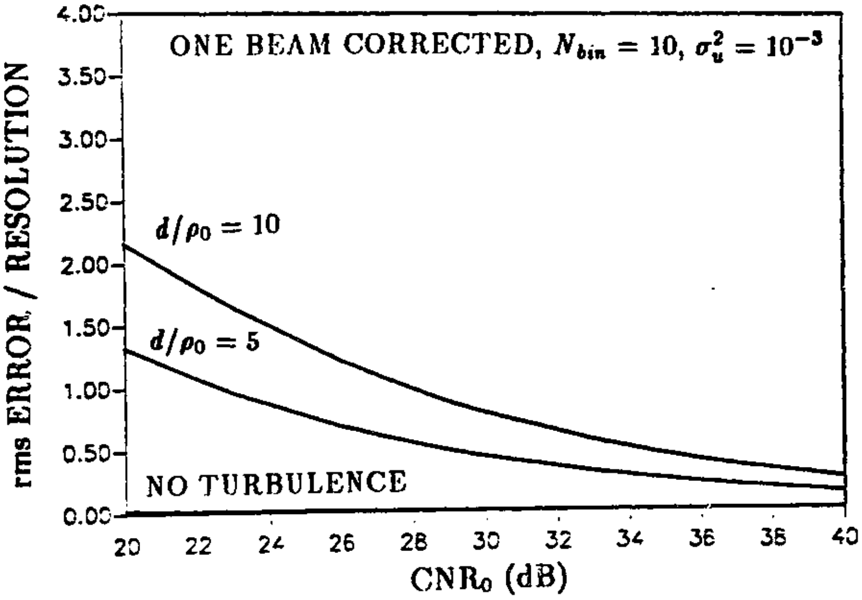

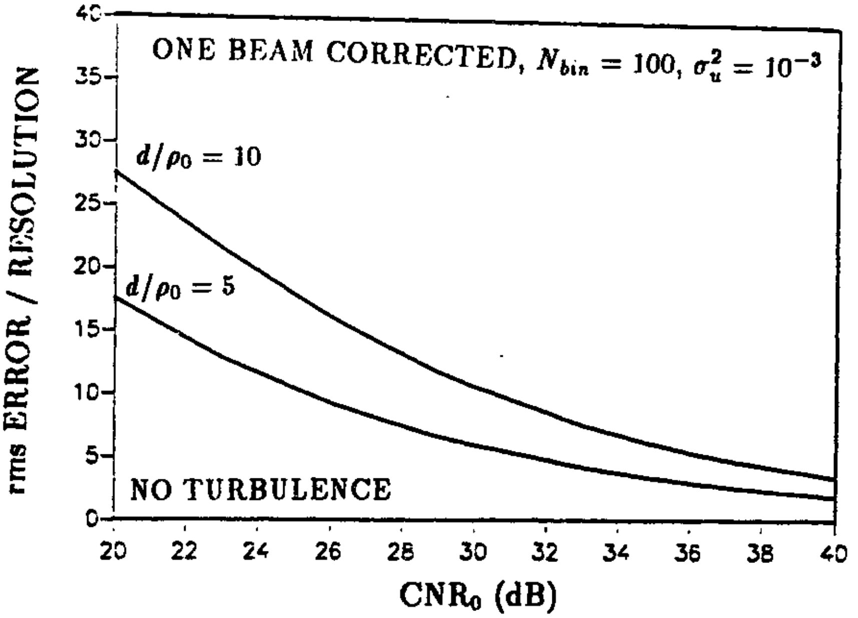

(Figures 6.2c and 6.2d)

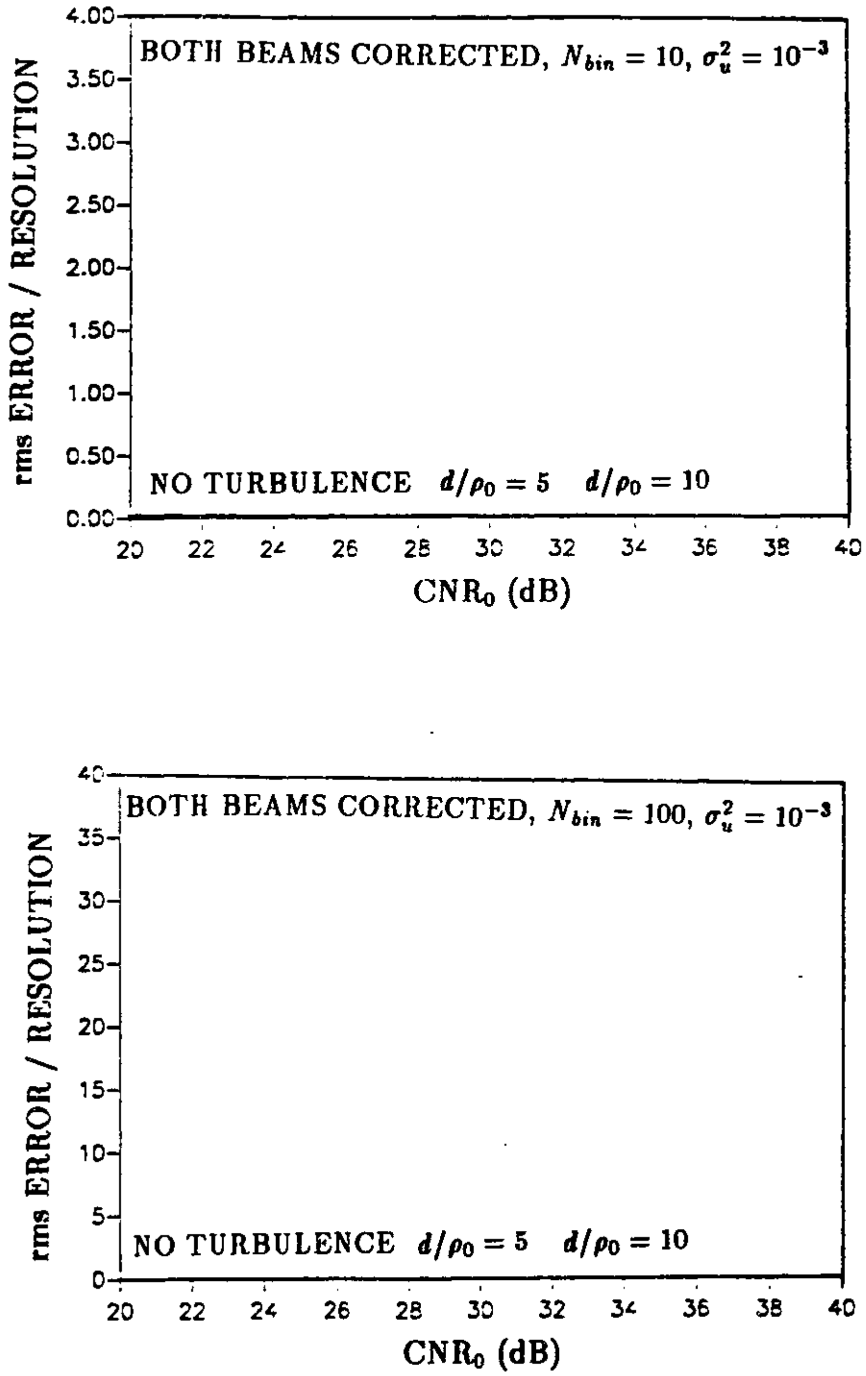

Figure 6.2: Normalized range or velocity error vs. carrier-to-noise ratio for various values of d/ρ_0; glint target. (a) no correction, $N_{bin} = 10$, (b) no correction, $N_{bin} = 100$, (c) one beam corrected, $N_{bin} = 10$, $\sigma_u^2 = 10^{-3}$, (d) one beam corrected, $N_{bin} = 100$, $\sigma_u^2 = 10^{-3}$, (e) both beams corrected, $N_{bin} = 10$, $\sigma_u^2 = 10^{-3}$, (f) both beams corrected, $N_{bin} = 100$, $\sigma_u^2 = 10^{-3}$.

Appendix

In the Appendix, the validity of the approximation of Eq. 5.15 is examined. Let

$$\mathbf{r} \equiv |\mathbf{r}|e^{i\theta} = \mathbf{y}e^{i\phi_R} + \mathbf{n}$$

be the IF signal whose phase, θ, we want to estimate. In the above equation, $\mathbf{r}$ corresponds to the IF signal's baseband complex envelope given in Eq. 5.8; $\mathbf{y}e^{i\phi_R}$ corresponds to the target-return component, where ϕ_R is the turbulence phase (see Eq. 5.11), and $\mathbf{n}$ corresponds to the shot noise component. Let $\mathbf{y} \equiv |\mathbf{y}|e^{i\phi_y}$ and $\mathbf{n} \equiv |\mathbf{n}|e^{i\phi_n}$; $\mathbf{y}$ and $\mathbf{n}$ are statistically independent zero-mean complex Gaussian random variables with $\langle|\mathbf{n}|^2\rangle = N_0$ and $\langle|\mathbf{y}|^2\rangle = N_0\text{CNR}$. The exact value of θ is

$$\theta = \tan^{-1}\left[\frac{|\mathbf{y}|\sin(\phi_y + \phi_R) + |\mathbf{n}|\sin(\phi_n)}{|\mathbf{y}|\cos(\phi_y + \phi_R) + |\mathbf{n}|\cos(\phi_n)}\right],$$

an expression equal to that of Eq. 5.14. The approximate value of θ when $|\mathbf{y}| \gg |\mathbf{n}|$ is

$$\theta_A = \phi_y + \phi_R - \frac{|\mathbf{n}|}{|\mathbf{y}|}\sin(\phi_y + \phi_R - \phi_n),$$

which can be seen to be Eq. 5.15 by noting that $\phi_y + \phi_R$ corresponds to $\angle\boldsymbol{\ell}_n$, $\mathbf{n}$ corresponds to $\mathbf{n}_n$, and $|\mathbf{y}|$ corresponds to $|\boldsymbol{\ell}_n|$.

The degree to which θ_A is a good approximation to θ can be seen by comparing the probability distributions of θ and θ_A. Conditioned on $\mathbf{y}$ and ϕ_R, $\mathbf{r}$ is a complex Gaussian random variable with mean $\mathbf{y}e^{i\phi_R}$ and variance N_0; the conditional probability distribution of θ given $\mathbf{y}$ and ϕ_R can be found in this way. This conditional distribution can then be averaged over the statistics of $|\mathbf{y}|$, a Rayleigh random variable, giving

$$\begin{aligned} p_{\theta|\phi_y,\phi_R}(\Theta|\phi_y,\phi_R) = {} & \frac{1}{2\pi}\frac{1}{1+\mathrm{CNR}\sin^2\delta}\cdot \\ & \left[1+\frac{\sqrt{\mathrm{CNR}}\cos\delta}{\sqrt{1+\mathrm{CNR}\sin^2\delta}}\left(\tan^{-1}\left(-\frac{\sqrt{1+\mathrm{CNR}\sin^2\delta}}{\sqrt{\mathrm{CNR}}\cos\delta}\right)+\varepsilon\right)\right], \\ & \text{for } -\pi \le \delta < \pi, \end{aligned}$$

where $\delta \equiv \Theta - \phi_y - \phi_R$, and $\varepsilon = \pi$ if $\cos\delta \geq 0$ and is 0 otherwise. The probability distribution for θ_A can be found in a similar way. Conditioned on **y** and ϕ_R, θ_A is a Gaussian random variable with mean $\phi_y + \phi_R$ and variance $N_0/(2|\mathbf{y}|^2)$. Averaging over the statistics of $|\mathbf{y}|$ gives

$$p_{\theta_A|\phi_y,\phi_R}(\Theta|\phi_y,\phi_R) = \frac{\sqrt{\mathrm{CNR}}}{2(1+\mathrm{CNR}\delta^2)^{\frac{3}{2}}},$$

where Θ may take on any value from $-\infty$ to ∞. However, for values of CNR large compared to 1, the probability distribution of θ_A is very small when $|\theta_A - \phi_y - \phi_R| > \pi$. The exact and approximate probability distributions given in the above two equations are plotted in Figures A.1a, A.1b, and A.1c, for CNR = 5, 10, and 20. For each of the CNR values, the approximate probability distribution is very accurate at the center and less accurate in the tails. The distributions for CNR=10 and CNR=20 seem considerably more sharply peaked than that for CNR=5; therefore we shall assume that θ_A is a good approximation to θ (i.e. that Eq. 5.15 is a good approximation) when CNR $\geq$ 10.

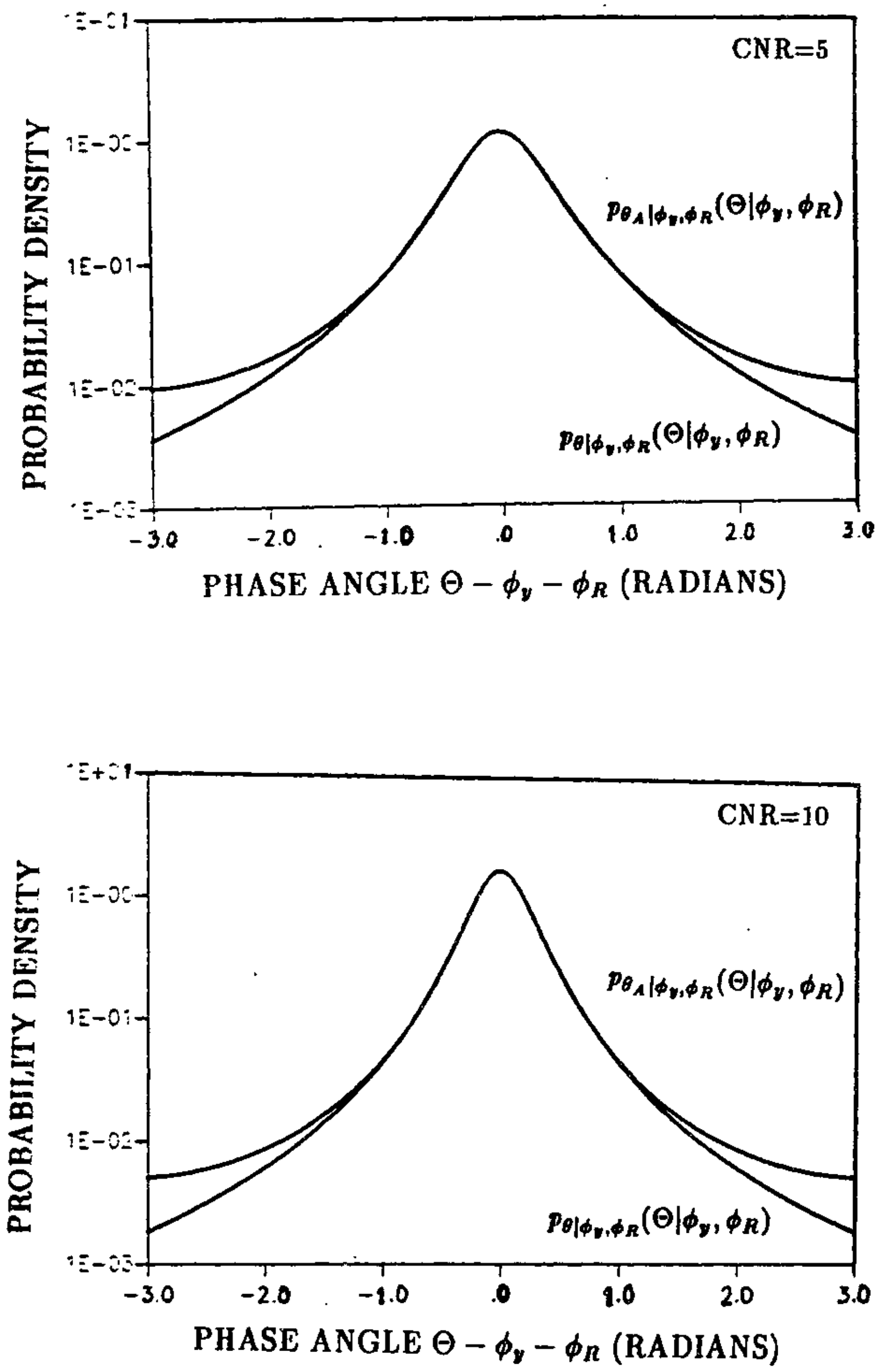

(Figures A.1a and A.1b)

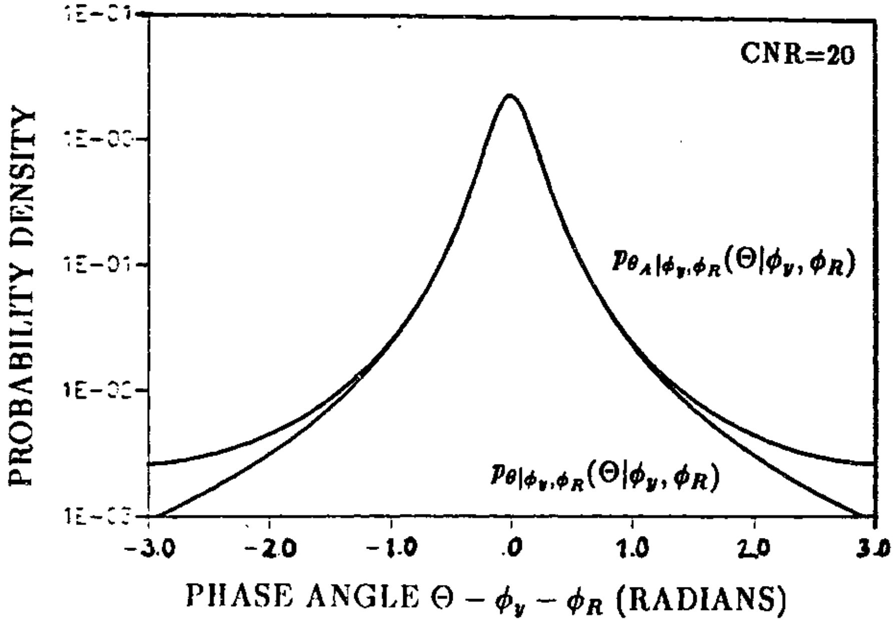

Figure A.1: Exact and approximate probability distributions for the IF signal phase. (a) CNR=5, (b) CNR=10, (c) CNR=20.

Bibliography

[1] M.I. Skolnik, *Introduction to Radar Systems, 2nd ed.*, McGraw-Hill, New York (1980).

[2] L.J. Sullivan, "Infrared coherent radar," Proc. SPIE, Vol. 227, pp. 148-161 (1980).

[3] R.C. Harney and R.J. Hull, "Compact infrared radar technology," Proc. SPIE, Vol. 227, pp. 162-170 (1980).

[4] A.B. Gschwendtner, R.C. Harney, and R.J. Hull, "Coherent IR radar technology," in *Optical and Laser Remote Sensing*, D.K. Killinger and A. Mooradian, eds., Springer-Verlag, Berlin (1983).

[5] R.L. DelBoca and R.J. Mongeon, "Multifunction CO_2 heterodyning laser radar for low level tactical operations," in *1979 National Aerospace and Electronics Conference*, pp. 1079-1088, IEEE, New York (1979).

[6] J.M. Cruickshank and P. Pace, paper ThA2 in *Digest of Topical Meeting on Coherent Laser Radar for Atmospheric Sensing*, Optical Society of America, Washington, D.C. (1980).

[7] I. Renhorn, O. Steinvall, D. Letalick, K. Gullberg, T. Claesson, and A. Widen, "Performance study of a coherent laser radar," Proc. SPIE, Vol. 415, pp. 39-50 (1983).

[8] R.M. Gagliardi and S. Karp, *Optical Communications*, Chapter 6, Wiley, New York (1976).

[9] J.W. Goodman, *Introduction to Fourier Optics*, Section 4.2, McGraw-Hill, San Francisco (1968).

[10] H.L. Van Trees, *Detection, Estimation, and Modulation Theory, Part III*, Section 10.1, John Wiley and Sons, New York (1968).

[11] J.H. Shapiro, B.A. Capron, and R.C. Harney, "Imaging and target detection with a heterodyne-reception optical radar," Appl. Opt., Vol.20, pp. 3292-3313 (1981).

[12] H.T. Yura, "Signal-to-noise ratio of heterodyne lidar systems in the presence of atmospheric turbulence," Optica Acta, Vol.26, pp. 627-644 (1979).

[13] S.F. Clifford amd S. Wandzura, "Monostatic heterodyne lidar performance: the effect of the turbulent atmosphere," Appl. Opt., Vol.20, pp. 514-516 (1981).

[14] D.M. Papurt, J.H. Shapiro, R.C. Harney, "Atmospheric propagation effects on coherent laser radars," Proc. SPIE, Vol. 300, pp. 86-99 (1981).

[15] J.W. Goodman, "Statistical properties of laser speckle patterns," in *Laser Speckle and Related Phenomena*, J.C. Dainty, ed., Springer-Verlag, Berlin (1975).

[16] A.V. Jelalian, W.H. Keene, and E.F. Pearson, "Tactical and atmospheric coherent laser radar technology," in *Optical and Laser Remote Sensing*, D.K. Killinger and A. Mooradian, eds., Springer-Verlag, Berlin (1983).

[17] J.H. Shapiro and P.L. Mesite, "Performance analyses for Doppler and chirped laser radars," Appendix C in R.J. Hull, D.G. Biron, S. Marcus, and J.H.

Shapiro, "Coherent laser radar remote sensing," Final Report, MIT Lincoln Laboratory, 30 Sept.1983.

[18] J.H. Shapiro, R.W. Reinhold, D. Park, "Performance analyses for peak-detecting laser radars," Proc. SPIE, Vol. 663, pp. 38-56 (1986).

[19] J.W.Hardy, "Active optics: a new technology for the control of light," Proc. IEEE, Vol.66, pp. 651-697 (1978).

[20] R.J. Becherer and B.A. Horwitz, eds., *Adaptive Optics Systems and Technology*, Proc. SPIE, Vol. 365 (1982).

[21] J.H. Shapiro, "Correlation scales of laser speckle in heterodyne detection," Appl. Opt., Vol. 24, pp. 1883-1888 (1985).

[22] J.H. Shapiro, "Imaging and optical communication through atmospheric turbulence," in *Laser Beam Propagation in the Atmosphere*, J.W. Strohbehn, ed., Springer-Verlag, Berlin (1978).

[23] R.S. Lawrence and J.W. Strohbehn, "A survey of clear-air propagation effects relevant to optical communications," Proc. IEEE, Vol. 58, pp. 1523-1545 (1970).

[24] E. Brookner, "Atmosphere propagation and communication channel model for laser wavelengths," IEEE Trans. Comm. Tech., Vol. COM-18, pp. 396-416 (1970).

[25] R.L. Fante "Electromagnetic beam propagation in turbulent media," Proc. IEEE, Vol. 63, pp. 1669-1692 (1975).

[26] J.Y. Wang, "Optical resolution through a turbulent medium with adaptive phase compensations," J. Opt. Soc. Am., Vol. 67, pp. 383-390, 1977.

[27] J.H. Shapiro, *Class Notes for Optical Detection and Communication, 6.453*, Department of Electrical Engineering and Computer Science, MIT (1980).

[28] M.M. Colavita, M. Shao, and D.H. Staelin, "Atmospheric phase measurements with the Mark III stellar interferometer," Appl. Opt., Vol. 26, pp. 4106-4112, 1987.

[29] V.I. Tatarskii, *Wave Propagation in a Turbulent Medium*, Chapter 3, McGraw-Hill, New York (1961).

[30] D.L. Fried, "Propagation of a spherical wave in a turbulent medium," J. Opt. Soc. Am., Vol. 57, pp. 175-180 (1967).

[31] D.L. Walters and K.E. Kunkel, "Atmospheric modulation transfer function for desert and mountain locations: the atmospheric effects on r_0," J. Opt. Soc. Am., Vol. 71, pp. 397-405 (1981).

[32] D.L. Fried, "Anisoplanatism in adaptive optics," J. Opt. Soc. Am., Vol. 72, pp. 52-61, (1982).

[33] A. Ishimaru, "Temporal frequency spectra of multifrequency waves in turbulent atmosphere," IEEE Trans. Antennas and Propagation, Vol. AP-20, pp. 10-19 (1972).

[34] S.F. Clifford, "The classical theory of wave propagation in a turbulent medium," in *Laser Beam Propagation in the Atmosphere*, J.W. Strohbehn, ed., Springer-Verlag, Berlin (1978).

[35] J.H. Shapiro, "Reciprocity of the turbulent atmosphere," J. Opt. Soc. Am., Vol. 61, pp. 492-495 (1971).

[36] J.Y. Wang and P.A. Pruitt, "Laboratory target reflectance measurements for coherent laser radar applications," Applied Optics, Vol. 23, pp. 2559-2564 (1984).

[37] T.S. McKechnie, "Speckle Reduction," in *Laser Speckle and Related Phenomena*, J.C. Dainty, ed., Springer-Verlag, Berlin (1975).

[38] A.E. Siegman, "The antenna properties of optical heterodyne receivers," Proc. IEEE, Vol. 54, pp. 1350-1356 (1966).

[39] J.H. Shapiro, V.I. Dardzinski, and E.W. Tung, "Coherent Laser Radar Antenna Patterns and Mixing Efficiencies," Appendix A in R.J. Hull, D.G. Biron, S. Marcus, and J.H. Shapiro, "Coherent laser radar remote sensing," Final Report, MIT Lincoln Laboratory, 30 Sept. 1983.

[40] S.M. Wandzura, "Meaning of quadratic structure functions," J. Opt. Soc. Am., Vol. 70, pp. 745-747 (1980).

[41] J.H. Shapiro, "Resolution and accuracy, ambiguity and anomaly for range-spread speckle targets," Proc. SPIE, Vol. 415, pp. 142-146 (1983).

[42] H.L. van Trees, *Detection, Estimation, and Modulation Theory, Part III*, Section 10.2.1, Wiley and Sons, New York (1971).

[43] J.G. Himes, "The Performance af an Active Optical Imaging Radar in the Turbulent Atmosphere," Appendix 3A, Ph.D. Thesis, Dept. of Elect. Engr. and Comp. Sci., MIT, February 1975.

[44] A. Papoulis, *Probability, Random Variables, and Stochastic Processes*, Section 8-6, McGraw-Hill, New York (1965).

[45] J.W. Hardy, J.E. Lefebvre, and C.L. Koliopoulis, "Real-time atmospheric compensation," J. Opt. Soc. Am., Vol. 67, pp. 360-369 (1977).

[46] R.A. Fisher, ed., *Optical Phase Conjugation*, Academic Press, New York (1983).

[47] D.P. Greenwood, "Adaptive compensation for atmospheric turbulence effects on optical propagation," presented at NATO/AGARD Advisory Group for Aerospace Research and Development, Norway, 4-7 Oct. 1983.

[48] D.L. Fried, "Optical resolution through a randomly inhomogeneous medium for very long and very short exposures," J. Opt. Soc. Am., Vol. 56, pp. 1372-1379 (1966).

[49] R.L. Mitchell, "Permanence of the log-normal distribution," J. Opt. Soc. Am., Vol. 58, pp. 1267-1272 (1968).

[50] J.H. Shapiro, "Point-ahead limitation on reciprocity tracking," J. Opt. Soc. Am., Vol. 65, pp. 65-68 (1975).

[51] D.Halliday and R.Resnick, *Fundamentals of Physics*, Section 14-7, Wiley and Sons, New York (1974).

[52] J.H.Shapiro, "Diffraction-limited atmospheric imaging of extended objects," J. Opt. Soc. Am., Vol. 66, pp. 469-477 (1976).

[53] K.S. Miller, *Complex Stocahstic Processes, An Introduction to Theory and Application*, Section III.3, Addison-Wesley, Reading MA (1974).

[54] I.S. Gradshteyn and I.M. Ryzhik, *Tables of Integrals, Series, and Products*, Section 3.47, Orlando, Academic Press (1980).

[55] R.H. Hudgin, "Wavefront compensation error due to finite corrector element size," J. Opt. Soc. Am., Vol. 67, pp. 393-395 (1977).

[56] D.L. Fried, "Optical heterodyne detection of an atmospherically distorted signal wave front," Proc. IEEE, Vol. 55, pp. 57-67 (1967).

[57] R.C. Smithson and M.L. Peri, "Partial correction of astronomical images with active mirrors," J. Opt. Soc. Am. A, Vol. 6, pp. 92-97 (1989).

[58] I.C. Winkler, M.A. Norton, and C. Higgs, "Adaptive phase compensation in a Raman look-through configuration," Opt. Lett., Vol. 14, pp. 69-71 (1989).

[59] J. Hecht, *The Laser Guidebook*, McGraw-Hill, New York (1986).

[60] Charles Freed, MIT Lincoln Laboratory, private conversation, January 1989.

[61] J.W. Daiber and H.M. Thompson, "Performance of a large, cw, preexcited CO supersonic laser," IEEE J. Quantum Electron., Vol. QE-13, pp. 10-17 (1977).

[62] W.L. Wolfe and G.J. Zissis, eds., *The Infrared Handbook*, Section 5.5.2, Office of Naval Research, Department of the Navy, Washington DC (1978).

[63] L.C. Bradley, K.L. SooHoo, and C. Freed, "Absolute frequencies of lasing transitions in nine CO_2 isotopic species," IEEE J. Quantum Electron., Vol. QE-22, pp.234-267 (1986).

[64] F.G. Gebhardt, "High power laser propagation," Appl. Opt., Vol. 15, pp. 1479-1493 (1976).

[65] L.C. Bradley and J. Herrmann, "Phase compensation for thermal blooming," Appl. Opt., Vol. 13, pp. 331-334 (1974).

[66] C.A. Primmerman and D.G. Fouche, "Thermal-blooming compensation: experimental observations using a deformable-mirror system," Appl. Opt., Vol. 15, pp. 990-995 (1976).

[67] C.A. Primmerman, F.B. Johnson, and I. Wigdor, "Thermal-blooming compensation using the CLASP system," Appl. Opt., Vol. 17, pp. 2909-2912 (1978).